UNIVERSITA' DEGLI STUDI DI NAPOLI FEDERICO II

Dottorato di Ricerca in Ingegneria Chimica
(XXI Ciclo)

Ph.D THESIS

Characterization of carbonaceous nanoparticle size distributions (1-10 nm) emitted from laboratory flames, diesel engines and gas appliances

Scientific Committee

SUPERVISOR

Prof. Antonio D'Alessio
DIC Università di Napoli "Federico II"

CO-SUPERVISOR

Prof. Andrea D'Anna
DIC Università di Napoli "Federico II"
Eng. LeeAnne Sgro
DIC Università di Napoli "Federico II"

Ph.D Student

Andrea De Filippo

Nada sabìamos de verdad.
A excepciòn del aire,
la tierra y el fuego,
todo es locura;
Dios incluido.

Héctor Tizòn

Acknowledgements

I want to thank my thesis advisor, Prof. Antonio "Ninni" D'Alessio, who was a tremendous mentor. Our talks on combustion, current results, future investigations, Dante and the Divina Commedia are well rubbed in my mind. Without his presence, the laboratory in Piazzale Tecchio will never be the same. I'd like also to thank Andrea D'Anna for his suggestions and advices and also because he was the first to orientate my interest towards the scientific research of combustion-formed compounds during his passionate undergraduate lectures, by now almost six years ago. I want to thank Lee Anne Sgro who taught me to develop critical skills necessary for the scientific research and to complete this thesis.

I must also acknowledge:

At the Ford Research and Innovation Center in Dearborn (Michigan), Matti Maricq, Joe Szente and all the researchers and technicians at the VERL labs. In particular, I'd like to thank Dr. Maricq for his useful advices and questions about combustion-generated nanoparticles. In few weeks there, I learned a lot about vehicles emissions and that experience was an important step for my future working decisions. I want also to acknowledge the "Programma di scambi internazionali per Mobilità di breve durata" by Università di Napoli "Federico II" for the financial support related to that experience.

Everyone I worked with in Napoli, or simply shared opinions and results at the Dipartimento di Ingegneria Chimica and Istituto Motori in these years.

All the intelligent and interesting people I have met at the Lawrence Berkeley National Laboratory and at U.C. Berkeley, especially Musahid Amhed, Kevin R. Wilson, Donald Lucas and Catherine Koshland. I want to thank the "Commissione Fulbright per gli Scambi Culturali tra l'Italia e gli Stati Uniti" and the Institute of International Education in San Francisco which supported my stay in California.

I want to thank Giacomo (dad) and Anna (mom), who both supported my studies and my choices, Stefania and Antonio who always demonstrate their proud for their little brother, Tonia and Fernando who always consider me as a son in their family.

I want to thank all my friends I had the fortune to meet in Napoli, Detroit and Berkeley, especially Errico, Alfredo, Roberto, Filippo, Eugenio, Pina and Tony, and their families, Alan and his friends, Erin, Marco, Irene, and my American "cousin" Ronny.

A special thank to my partner, friend and lover, Azzurra. My life with her began just few months before I started my doctorate and so she lived with me all the positive and negative moments of this experience. The sincerity of her feelings gave me the required self-confidence to make difficult, but unavoidable, choices. She made these years specials for me.

Finally I want also to thank the two little hamsters that have been living in my brain for 29 years, continuously moving the lonely neuron in order to follow the Dante's teaching:

"*Non vogliate negar l'esperienza di retro al sol, del mondo sanza gente. Considerate la vostra semenza, fatti non foste a viver come bruti ma per seguir virtute e canoscenza"*

(Dante Alighieri, Divina Commedia, Inferno canto XXVI, 116-120)

Abstract

Commercially available SMPS and a differential mobility analyser (DMA) designed to enable detection of particles as small as 1 nm were used to provide further information about nanoparticles emitted from premixed flames, engines and common burners, with particular attention to the 1-10 nm range. Premixed laboratory flames were studied to examine carbonaceous nanoparticle formation in fuel rich burning conditions near the onset of soot formation. Nanoparticles were measured at different carbon/oxygen (C/O) ratio and at different heights above the burner surface in order to evaluate their behaviour in high temperature conditions. The measured size distributions showed that the first particles observed in flames have a size of ~2nm (Mode I), consistent with previous *in situ* measurements by light scattering and extinction (LSE), size distributions determined by Atomic Force Microscopy (AFM) of particles deposited by thermophoresis on mica substrates and off-line size measurements of material captured in water samples from the same flames. A larger 3-7 nm particle mode (Mode II) was measured in richer flames and later in the flame, which was not previously distinguished by optical measurements, which can only give the d_{6-3} diameter (ratio of the 6^{th} and 3^{rd} moments of the size distribution) or in the size distributions determined by AFM, which had lower resolution. This larger mode is also not observed in water samples collected from flames even when their concentration is as large as or larger than the 2nm mode, presumably because the larger particles are hydrophobic. The evolution of these two nanoparticles modes was studied in a flame with C/O = 0.65 at different height above the burner surface. The results were consistent with the conceptual framework for particle inception, advanced in earlier works based on UV-visible optical measurements, and for particle coagulation which seemed to increase because of the appearance of mode II, in agreement with the size-dependent coagulation rate addressed in previous studies based on optical measurement and atomic force microscopy (AFM).

To begin addressing the question of whether or not such small particles are also found in the exhausts/emissions of applied combustion systems were they may be inhaled by humans or interact with the atmosphere, size distributions of nanoparticles generated by a burner, a test engine and diesel vehicles were measured. The emissions from a test bench single-cylinder engine and from two modern light-duty diesel vehicles run with commercial ultralow sulphur fuel indicated the presence of a “solid” particle nucleation mode (~ 10nm or lower) which accompanied normal soot emissions (~ 60 nm). In diesel vehicle tests, this mode, most prominent at idle, was highly sensitive to the level of exhaust gas recirculation (EGR), non-volatile to temperature higher than 400 C and electrically charged. All of these characteristics suggest that these solid particles were formed during combustion and not by lower temperature condensation processes as the exhaust cools. An important conclusion of these tests was also that the specific diesel particulate filters employed removed the “solid” nucleation mode and the soot with efficiency comparable to soot. Tests on bench single-cylinder engines again indicated that the smallest nanoparticles were highly influenced by the EGR levels but also the type of injections and the type of fuel employed have an effect on the emitted particulate. Preliminary measurements on domestic gas appliances burning methane also showed the presence of nanoparticles in the size range 1-3 nm in the plume near the burner, in agreement with optical absorption measurements

and time resolved fluorescence polarization anisotropy (TRFPA) analysis on water samples from the same flames.

INDEX

Acknowledgements 1

Abstract 2

Introduction 6

Chapter 1: 8
ULTRAFINE PARTICLES
- **1.1 Atmospheric aerosol** 8
- **1.2 Classification and sources** 8
- **1.3 Environmental and health effects** 11
- **1.4 Formation and growth of ultrafine particles** 12
- **1.5 Carbonaceous ultrafine particles: Elemental Carbon (EC) and Organic Carbon (OC)** 13
  - **1.5.1 Emissions by internal combustion engines and regulations** 13
  - **1.5.2 Emissions by flames and soot formation pathway** 15
  - **1.5.3 Incipient nanoparticles** 17
- **1.6 Specific discussion: definitions of particle diameters** 18
- **1.7 Specific discussion: particle size distribution functions** 19

Chapter 2: 21
EXPERIMENTAL APPARATUS: ANALYSIS SYSTEMS
- **2.1 Introduction** 21
- **2.2 Analysis systems: Electrical Mobility Spectrometer and Scanning Mobility Particle Sizer** 22
  - **2.2.1 Classification by electric mobility: general features and theory** 22
  - **2.2.2 tapcon EMS DMA 3/150 & TSI SMPS 3936: analogies and differences** 24
  - **2.2.3 tapcon EMS DMA 3/150 & TSI SMPS 3936: experimental comparison** 25
  - **2.2.4 tapcon EMS: sub-nanometer peak** 31

Chapter 3: 35
EXPERIMENTAL APPARATUS: SAMPLING DEVICES
3.1 Sampling devices: probes and ejectors 35
3.2 Horizontal probe 36
3.2.1 Brief overview 36
3.2.2 Effect on the flame temperature 37
3.2.3 Effect of dilution on the measured size distributions 39
3.2.4 Pinhole clogging: effect of particle deposition in time 43
3.3 Home-made ejectors and the Dekati diluter 45
3.4 Diffusion losses along the sampling line 46

Chapter 4: 49
EXPERIMENTAL RESULTS: PREMIXED LABORATORY FLAMES
4.1 Introduction 49
4.2 Premixed ethylene-air flames from a McKenna burner 50
4.3 Flame-generated nanoparticles at different C/O ratios 51
4.3.1 Size distributions 51
4.3.2 Particle charge 53
4.4 Size distributions at different heights above the burner surface 56
4.4.1 C/O=0.65: experimental results 57
4.4.2 C/O=0.65: experimental versus numerical results 59
4.4.3 C/O=0.63 & C/O=0.60: experimental results 61
4.5 Effect of flame gas velocities 64
4.6 Effect of fuel employed: comparison with methane flames 66

Chapter 5: 68
EXPERIMENTAL RESULTS: BEHAVIOR OF FLAME-GENERATED PARTICLES IN A RESIDENCE TUBE
5.1 Introduction 68
5.2 Effect of residence time on the measured size distributions 70
5.3 Effect of humidity on the measured size distributions 74
5.4 Interaction of flame-generated nanoparticles with ~50 nm NaCl particles 76

Chapter 6: 78
EXPERIMENTAL RESULTS: DIESEL VEHICLES AND TEST BENCH ENGINE
6.1 Introduction 78

6.2 Light-duty diesel vehicles: nucleation mode particles 79
6.2.1 Test vehicles and operating conditions 79
6.2.2 Effect of vehicle speed and exhaust gas recirculation (EGR) 80
6.2.3 Nanoparticle volatility & charge measurement 82
6.2.4 Effect of exhaust after treatment 84
6.3 Test bench single-cylinder engine: nucleation mode particles 85
6.3.1 Operating conditions 85
6.3.2 Particle size, mass, gases and cycle-pressure measurements 86
6.4 General comments 94

Chapter 7: 96
EXPERIMENTAL RESULTS: DOMESTIC GAS BURNERS
7.1 Introduction 96
7.2 Domestic gas burners 96
7.2.1 Experimental procedure 96
7.2.2 Nanoparticles naturally convoyed to the analyzer (no dilution employed) 97
7.2.3 Nanoparticles sampled through a home-made ejector (dilution employed) 99
7.3 Final comments 101

Conclusions 102

Bibliography 105

Introduction

At the present time, combustion based on carbon containing species still represents the most important source of energy (IEA, 2006). The worldwide growing demand of energy supply points out the concerns regarding its massive use while repositories last and, at the same, more specifically, emphasizes the present and overall effects related to the emissions of carbon dioxide and combustion-generated particles. While the first has a well-known impact on the climate forcing representing one of the most important greenhouse gas in Earth's atmosphere (Kyoto, 1997), the carbon-based particulate matter is a category whose impact on human health and atmospheric particles is not completely well understood but whose potential importance has been clearly addressed (AQMD, 2006). Understanding their physical and chemical properties, as well as their toxicity, their size and growth processes, as well as their interaction with other atmospheric aerosols, represents the goal of many current investigations on vehicle exhausts and on laboratory flames.

The majority of the concern is related to the high emissivity in number concentration as the size decreases and to the combustion conditions which favour their emission. If studies on laboratory flames give important basilar information on these combustion-generated high molecular mass structures, studies on engines (and common burners) give a realistic prospective with the possibility, for example, to evaluate the new efficient injection system and the introduction of after treatment devices with respect to these nanoparticles. Despite the recent technological advances that have caused a strong reduction of particulate mass concentration at the exhaust of diesel engines, the actual filter media still enable a high number of ultrafine particles to pass in the engine exhaust and be released into the atmosphere. In next years, their removal will be one of the goals of the automotive industry, since as reported in the draft proposal Euro5/6 emissions standards, the upcoming normative will introduce number based Particulate Matter (PM) limits (Euro 5/6 Standards, 2007) in addition to the traditional mass based limits. Therefore, it becomes crucial to completely characterize the nature and the properties of these nanoparticles as well as to identify their origin and the formation and growth mechanisms.

Under fuel rich burning conditions, including those typical of modern engines/burners that emit low to undetectable levels of soot, investigations on laboratory hydrocarbon-air flames revealed some important properties of the first incipient carbon-based particles: mean diameter about ~2-3nm, an organic carbon structure, and transparency to the visible radiation (D'Alessio *et al.*, 2007). In addition these Nanoparticles of Organic Carbon (NOC) experience a size-dependent coagulation rate at high temperature which implies that flame-generated nanoparticles, particularly those smaller than 3-5 nm, may escape the exhaust devices of modern combustion systems without ultimately growing to larger sizes, especially when no adequate filter media are employed (D'Alessio *et al*., 2005; Lanzuolo *et al.*, 2008). Similar properties are observed for nanoparticles collected in water samples from gasoline and diesel powered vehicles (Sgro *et al*., 2008a).

Currently the choice of a single method able to detect these macromolecules/nanoparticles and to give information about their chemical and physical properties as well as the growth processes and interactivity with other species as function of their size, appear very difficult. Among the experimental techniques that can be applied, the literature distinguishes two broad categories: the non-intrusive optical measurement techniques (e.g. UV absorption) and intrusive probe sampling diagnostics. The optical techniques are real

time and “in situ” and give information about the size and the chemical nature of the particle but present limitations related to the accuracy for the refractive index of the investigated species. The probe sampling diagnostic category generally includes the combined use of a sampling dilution device and a subsequent analysis system to measure size distribution (e.g. Scanning Mobility Particle Sizer (SMPS)) and mass spectra (e.g. Photoionisation Mass Spectrometry (PIMS)). The accuracy of the latter techniques is generally dependent on the capability to minimize losses and particle-particle interactions in the path from the sampling points to the analysis system but they have an important advantage over optical diagnostics: they can selectively and sensitively measure most of the combustion-generated species that are not amenable to spectroscopic techniques.

In this thesis, commercially available Scanning Mobility Particle Sizer (SMPS) and Electrical Mobility Spectrometer (EMS), both based on the differential mobility analysis (DMA), are used to provide further, and new, information about nanoparticles emitted from premixed flames, engines and common burners, with particular attention to the 1-10 nm range. More specifically, the *First Chapter* is a review of current terminology and classification of ultrafine particles with a specific focus on the carbon-based compounds. The *Second Chapter* is focused on a direct comparison between the two different systems used in this work. In addition to a detailed description of the main components of each system, a simultaneous experimental investigation on the nanoparticles generated from a premixed ethylene-air flame is made to have direct information on the efficacy of the two instruments to detect the full range of molecular clusters/nanoparticles down to 1nm. The *Third Chapter* reviews the different sampling devices used in this thesis with particular attention to some common problems in order to avoid sampling artefacts. In the *Fourth Chapter* flame-generated nanoparticles, emitted from fuel rich burning condition below the on-set of soot formation, are studied at different carbon/oxygen (C/O) ratio and at different heights above the burner surface in order to evaluate their behaviour at high temperature conditions and have a comparison with previous results achieved on similar flames with optical techniques and atomic force microscopy. To this aim, the sampling devices are operated to obtain high and immediate dilution at the sampling point in order to preserve the nanoparticle size distribution as in the flame. The *Fifth Chapter* describes preliminary measurements on the behaviour of flame-generated nanoparticles in a residence tube, in different humidity conditions and in the presence of NaCl nanoparticles. The *Sixth Chapter* reports the emissions from a test bench single-cylinder engine and from two modern light-duty diesel vehicles which were run with commercial ultralow sulphur fuel and investigated at different vehicle speeds and exhaust gas recirculation (EGR) conditions. In the diesel vehicle tests, particle size, volatility, the electrical charge and effect of the after treatment devices are measured to examine the physical nature and the origin of the measured nanoparticles with special attention to the 1-10 nm range. In the case of the single-cylinder engine, emissions from a different fuel, N-Heptane, are also studied at different EGR levels and injection conditions and the measurements are completed by PM mass and gases concentrations measured by conventional instrumentations. The *Seventh Chapter* reports preliminary measurements to investigate the emissions from a commercial domestic gas appliances fuelled with methane.

First Chapter

Ultrafine particles

1.1 Atmospheric aerosol

A commonly accepted definition of aerosols is "a suspension of solid or liquid particles in a gas" (Hinds, 1999). Both the particles and the gas phase constitute the unique system which is usually referred with the term *aerosol*. Liquid particles are also referred as *droplets* while the term *particulate matter* is a collective term used for any substance (except pure water), either solid particles or liquid droplets, that exists in the atmosphere under normal conditions; from freshly nucleated clusters containing a few molecules to cloud droplets and crustal dust particles up to tens of microns in size (Seinfeld, 1996; McMurry, 2000b). Particulate matter may be generated by natural processes (e.g., bacteria, fungi, mold, salt spray, soil from erosion, volcanoes, dust, forest fires, etc.) or through human activities, including diesel trucks, power plants, wood stoves and industrial processes. The morphology (in terms of diameter) and the composition often reflect the various origins of the air emissions and atmospheric processing. Particles are either emitted directly into the atmosphere (*primary aerosol*) or formed in the atmosphere from the physical and chemical transformation of other vaporous or gaseous components (*secondary aerosol*) (Hinds, 1999).

1.2 Classification and sources

Particle size is the most important parameter for characterizing the behavior of aerosols. There are different approaches and conventions in the classification of particles by sizes. U.S. EPA (Environmental Protection Agency) (US EPA, 2004) furnishes three different approaches defined by:

- Modes, based on the observed size distributions and formation mechanisms
- Dosimetry or occupational health sizes, based on the entrance into various compartments of the respiratory system
- Cut-point, usually based on the 50% cut-point of the specific sampling device

US EPA also reports an idealized classification based on particle modes, as first proposed by Whitby in 1978. Four particle modes are identified (see Figure 1.1):

- Nucleation Mode: Freshly formed particles with diameters below about 10 nm, observed during active nucleation events. The lower limit is currently at about 3nm, equal to the lower size detection limit of the most widely used SMPS (TSI Model)
- Aitken Mode: Larger particles with diameters between about 10 and 100nm
- Accumulation Mode: Particles with diameters from about 0.1 μm to just above the minimum in the mass or volume distributions which usually occurs between 1 and 3 μm
- Coarse Mode or Coarse Particles: Particles with diameters mostly greater than the minimum in the particle mass or volume distributions, which generally occurs between 1 and 3 μm.

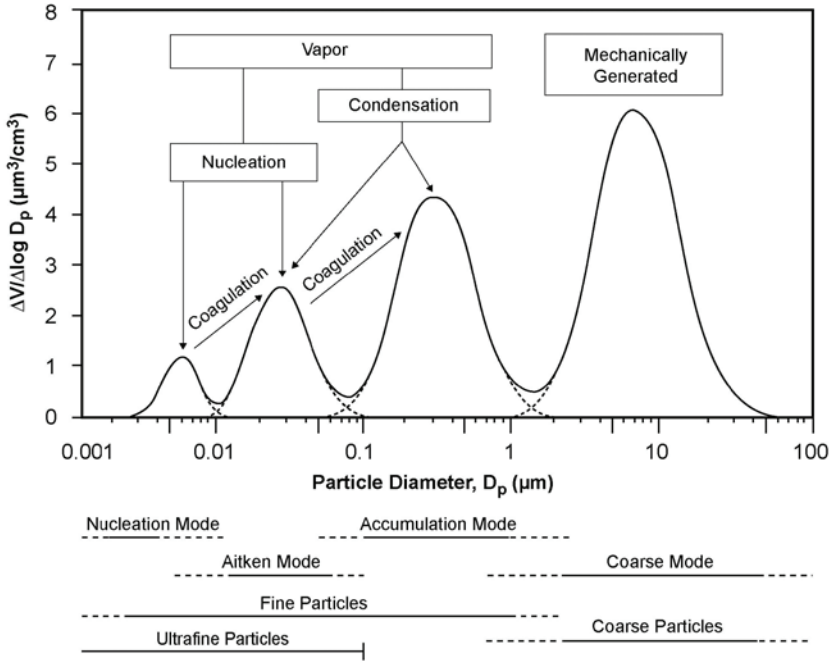

Figure 1.1 Idealized size distribution of atmospheric particle modes, adapted from US Environmental Protection Agency (US EPA, 2004).

In the classification by EPA, it is also possible to observe two further categories:

- *Fine Particles*: They include nucleation, Aitken, and accumulation modes, i.e., particles from the lowest measurable size, currently about 3 nm, to just above the minimum in the mass or volume distribution which generally occurs between 1 and 3 μm.
- *Ultrafine particles(UFPs)*: They are not a mode. In the air pollution literature, they are generally defined by size alone, i.e., particles with diameters of 0.1 μm (100 nm) or less. They include the nucleation mode and much of the

Aitken mode. They may also be defined as particles whose properties differ from those of the bulk material because of their small size.

In particular, Preining (1998) divides the spectrum of ultrafine particles as follow:

- *Nano-Size aerosol*: Particles smaller than about 20 nm
- *Very, very small aerosol*: Particles smaller than about 5 nm, particle behavior dominated by surface effects, total number of molecules less than about 500
- *Molecular size aerosol*: Particles smaller than about 1 nm, less than 10 molecules in the particle

The convention adopted by the occupational health community led to classify atmospheric particles in terms of their entrance into various compartments of the respiratory system. Thus, three great categories are identified: *inhalable, thoracic* and *respirable* particles (US EPA, 2004). *Inhalable* particles enter the respiratory tract, beginning with the head airways. *Thoracic* particles travel past the larynx and reach the lung airways and the gas-exchange regions of the lung. *Respirable* particles are a subset of thoracic particles that are more likely to reach the gas-exchange region of the lung.

The classification based on the 50% cut-point of the specific sampling device led to another commonly accepted terminology:

- *Total Suspend Particulate Matter (TSP)*: archaic definition for all particles in the atmosphere with the upper cut-off size dependent on the wind speed and direction and ranging from 25 to 40 μm
- PM_{10}: Particulate Matter with an aerodynamic diameter smaller than or equal to 10 micrometers
- $PM_{2.5}$: Particulate Matter with an aerodynamic diameter smaller than or equal to 2.5 micrometers
- *Nanoparticles:* Particles with diameters smaller than 50 nanometers

Beyond the size, these different particle modes have distinctly different chemical composition, sources, and lifetime in the atmosphere. As labeled in Figure 1.1, coarse particles are mechanically generated (grinding, erosion, and resuspension by the wind) and they are usually removed from the atmosphere within hours, due to their higher gravitational settling velocities. Thus, they may settle out from the air rapidly than smaller particles and usually will be found relatively close to their emission source. It is worth reminding that the origin of atmospheric particles is both natural and anthropogenic. Globally, there are many natural sources such as dust, volcanoes, sea sprays, forest fires and secondary aerosols from the atmospheric oxidation of biogenic material. In urban areas, fine particles are mostly generated by human activities through gas-to-particle conversion mechanisms, including homogeneous and heterogeneous nucleation, and by condensation onto preexisting particles in the accumulation-size mode, and they have lifetimes in the atmosphere on the order of days (Hinds, 1999). They can be transported long distances by wind and weather and can be found in the air thousands of miles from where they are formed. The major chemical constituents are nitrates, sulfates, organic carbon (OC) and elemental carbon (EC), as well as a variety of trace metals formed in combustion processes (US EPA, 2003).

As displayed in Figure 1.1, unlike coarse and fine particles, which are naturally divided by a cut-point of 2.5 μm, there is no clear cut-point that separates ultrafine particles from accumulation-mode PM. This is because, unlike coarse and fine particles, which have distinctly different origins, a major fraction of accumulation-mode particles originates from the ultrafine mode (Sioutas *et al.*, 2005). Recent studies in urban and rural areas, worldwide located (Woo *et al.*, 2001; Shi *et al.*, 2001; US EPA, 2003; Morawska *et al.,* 1998; Trier, 1997; Rodriguez *et al.*, 2005), demonstrates that a large fraction of urban ultrafine particles consists of primary combustion products from mobile source emissions (mostly diesel and automobile exhaust) and includes organic compounds, EC, and metals.

If most ambient PM mass is distributed in the larger particle size range (or modes), that is, the coarse and the accumulation modes, on the other hand, the ultrafine mode contains the majority (in numbers) of the ambient particles and an appreciable portion of total surface area (Hinds, 1999). Figure 1.2 displays idealized diesel exhaust particle number and mass weighted size distributions (Kittelson, 1998). In this case, the ultrafine particles account for 1-20% of the total particle mass but for more than 90% of the total particle number.

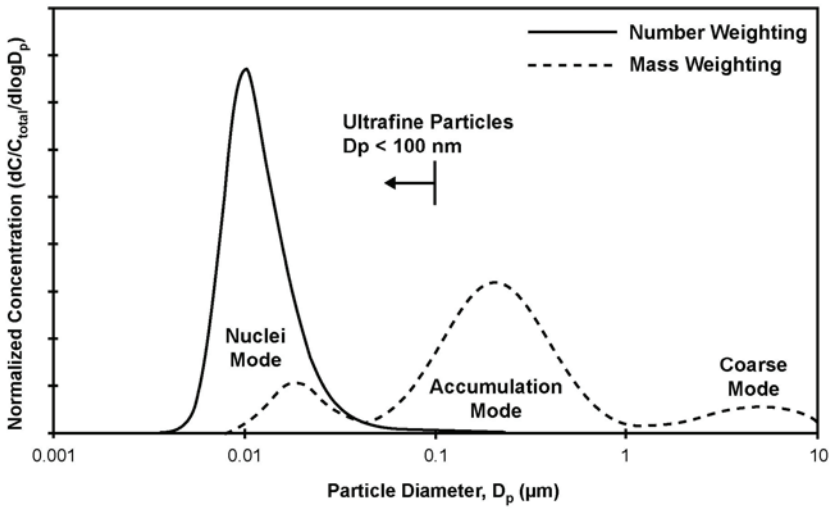

Figure 1.2- Number and mass engine exhaust size distribution, adapted from Kittelson (1998)

1.3 Environmental and health effects

Fine and ultrafine particles are the major sources of haze that reduces visibility both in urban and rural areas. Visibility impairment occurs when particles scatter and absorb light, creating a haze that limits the distance we can see and that degrades the color, clarity, and contrast of the view (US EPA, 2003; Jung & Kim, 2006). Humidity can also significantly increase visibility impairment by causing some particles to become more efficient at scattering light. Poor summertime visibility is primarily the result of high sulfate concentra-

tions, combined with high humidity. Organic carbon and nitrates also contribute to reduce visibility.

Atmospheric fine and ultrafine particles are particularly important in environmental health. The growing body of epidemiological studies indicates a clear relationship between the exposure to particulate air pollution in urban areas and acute increase in morbidity and mortality rates, especially for persons with obstructive lung and cardiovascular diseases (Pope, 2000). More generally, they both cause adverse health effects in humans, but in different ways (Wichmann *et al*., 2000). Although it is not clear from epidemiology studies, whether it is the mass, number or the surface area of particles which is the most determinant of health impact, some information from epidemiological studies suggests that ultrafine particles (with a diameter < 100 nm) exert a much stronger physiological effect than the same mass of larger particles (Oberdorster *et al*., 1992; Donaldson *et al*., 1998).

Nevertheless, due to their larger number (and also the surface area) than the number of coarse and fine particles, ultrafine particles can carry large amounts of adsorbed or condensed toxic air pollutants (oxidant gases, organic compounds, and transition metals) (Oberdorster, 2001) which may also cause inflammatory effects. In addition, the smaller particles are capable of penetrating deeper into the respiratory tract, thus, producing pulmonary inflammation at both epithelial and interstitial sites, as well as entering the circulation to reach other target sites, including the cardiovascular system (Nemmar *et al*., 2002,2004; Oberdorster, 2001; Oberdorster *et al.*, 2002). Over the last decade, toxicology has also made important progress regarding biological plausibility for the epidemiological findings associate with the exposure to ultrafine ambient particles (Oberdorster *et al*., 2002).

These observations show that not only is total particle concentration important but also the size distribution (and the surface area) of ultrafine particles (Kreyling *et al*., 2004). Therefore, over recent years there has been increased interest in the size distribution of atmospheric ultrafine particles and their mechanisms of formation and growth.

1.4 Formation and growth of ultrafine particles

Ultrafine particles can be formed in the atmosphere by at least three processes (Sioutas, 2005):

a) Incomplete combustion processes, mostly associated with motor vehicles and industrial sources (Kittelson, 1998)
b) Nucleation and condensation of hot supersaturated vapors, emitted from combustion sources, while being cooled at ambient temperature (Holmes, 2007)
c) Chemical reactions in the atmosphere

In addition to the formation by direct emissions from combustion processes, new particles are formed by a variety of nucleation processes of non-or low-volatile gas–phase compounds (Holmes, 2007; Kulmala *et al.*, 2004; Stainer *et al.*, 2004). Most new particle formation within the atmosphere is assumed to occur by several possible mechanisms: binary nucleation of sulphuric acid and water; ternary nucleation involving a third molecule, likely ammonia which is abundant in the troposphere and has been shown to enhance nu-

cleation rates of sulphuric acid (Weber *et al.*, 1998); ion-induced nucleation (Yu & Turco, 2000). Anther possible mechanism for new particle formation includes organic compounds that either participate in the nucleation process or react in the atmosphere to form compounds that nucleate. Due to their low concentrations, the identity and concentrations of these compounds are not yet known (Kulmala *et al.*, 2004).

The growth rate of ultrafine particles depends on season and location and more specifically on factors including particle size, chemical composition, concentration and temperature. Particles may grow by condensation as gas phase material condenses on existing particles (preferentially on smaller particles) or by coagulation as two particles combine to form one at a rate decreasing as the particle size increases.

1.5 Carbonaceous ultrafine particles: Elemental Carbon (EC) and Organic Carbon (OC)

Carbon-based compounds make up a large fraction of ultrafine and fine PM in urban areas (US EPA, 2003). These carbonaceous aerosols are released from incomplete combustion processes, the latter including motor vehicles on the streets of urban areas and also domestic heating by fossil fuel burners situated in individual apartments and houses. New technologies applied to motors and burners have reduced the emissions of large particles, but particles below 100nm in diameter down to few nanometers are still emitted into the atmosphere. Carbonaceous compounds may be inorganic, in the form of elemental or black carbon, referred as *Elemental Carbon (EC)* or *soot*, and organic, in the form of numerous species whose characteristics depend on the thermodynamic conditions while the particles remain suspended in air and also during sampling. The latter category is called *Organic Carbon (OC).* EC is solely primary in nature, whereas OC can be directly released into the atmosphere or produced via secondary gas-to-particle conversion processes. The identification of the physical and chemical characteristics of carbonaceous aerosols is not trivial, and detailed characterization of OC is used to determine the specific source, or origin, of emissions, namely the nature of the fuel and how the combustion process is carried out.

1.5.1 Emissions by internal combustion engines and regulations

Vehicle engine exhaust may include both the categories described above (and also sulfates and metallic particles). Ultrafine particles are observed in the emissions from spark, diesel and jet engines (Kittelson, 1998). The typical size distribution of engine exhaust PM is bimodal with the larger size particles ($d>50$ nm) mainly composed of carbonaceous soot aggregates formed directly in combustion (Harris & Maricq, 2001) and the smaller mode ($d<50$nm) traditionally associated with hydrocarbon and sulfate nucleation as exhaust cools. However the nature of the smaller size mode is still debated and recent intriguing observations suggest that the smaller mode can sometimes contain nonvolatile cores (Kittelson *et al*., 2006; Ronkko *et al.*, 2007) which can be possibly originated either in the engine from pyrolyzed hydrocarbons, and lube oil derived ash, or in the engine at high-temperature combustion processes and reactions (Sgro *et al*., 2008a). In the latter case, the

particles are referred as nanoparticles of organic carbon (NOC) due to their similarities to those emitted by premixed flames (D'Alessio *et al*., 2007).

The continuous research to understanding how soot is formed, soot properties and its association with smaller size particles, is driven by the necessity, on one side, to refine the classical engine combustion coupled to the development of complex after-treatment systems, taking into account a possible increase of fuel consumption, and on the other side, to develop new combustion systems in order to cut directly the raw emissions itself. Traditionally there has been a more focus on the properties and the effects of diesel exhaust emission than the gasoline ones. This was primarily the consequence of a higher emission (10-100 times) in terms of mass of diesel particulate with respect to those from spark ignition engines. Over the last years, the introduction of very strict regulations for vehicles' exhaust emissions improved the quality of combustion processes, fuels and after-treatment devices, leading to a significant reduction of the particle mass concentration but also to a significant shifting towards lower particle size with a higher number concentrations (Burtscher, 2005). Therefore the next steps of the European Union regulations for emission standards from motor vehicle passenger cars (Euro 5 and Euro 6) have the aim to match the goal of near zero emission engines, including number-based PM limits, beside the traditional mass-based PM limits. Thus, spark ignition cars, equipped with direct injection engines, will be subjected to the same regulations as for diesel cars (Euro 5/6 Standards, 2007). This is a consequence of several experimental investigations that demonstrated that also spark ignition engines emit high number concentration of nanoparticles under high load in rich mixture conditions, including cold starts and acceleration (Gaskow *et al.*, 1998; Cadle *et al*., 1998).

Table 1.1 – **Euro 5 emission limits[1], adapted from Euro 5/6 Standards (2007)**

		RM (Kg)	Limit Values													
			Mass of (CO)		Mass of THC		Mass of NMHC		Mass of NO_x		Mass of THC+NO_x		Mass of PM_x		Number of P	
			L_1 (mg/km)		L_2 (mg/km)		L_3 (mg/km)		L_4 (mg/km)		$L_2 + L_4$ (mg/km)		L_5 (mg/km)		L_6 (#/km)	
Cat	Class		PI	CI	PI	CI	PI	CI	PI	CI	PI	CI	PI	CI	PI	CI
M		All	1000	500	100	–	68	–	60	180	–	230	5/4.5	5/4.5		$6x10^{11}$
N_1	I	RM≤1305	1000	500	100	–	68	–	60	180	–	230	5/4.5	5/4.5		$6x10^{11}$
	II	1305<RM ≤1760	1810	630	130	–	90	–	75	235	–	295	5/4.5	5/4.5		$6x10^{11}$
	III	1760<RM	2270	740	160	–	108	–	82	280	–	350	5/4.5	5/4.5		$6x10^{11}$
N_2			2270	740	160	–	108	–	82	280	–	350	5/4.5	5/4.5		$6x10^{11}$

[1] Nomenclature: RM=Reference Mass; CO=Carbon Monoxide; THC=Total Hydrocarbon; NMHC=Non-Methane Hydrocarbons; NO_x=Oxides of Nitrogen; PM=Particulate Matter; P=Particles; PI=Positive ignition; CI=Compression ignition; Category M=vehicles designed to fulfill specific social needs;

Table 1.2 – **Euro 6 emission limits[2], adapted from Euro 5/6 Standards (2007)**

		RM (Kg)	Limit Values													
			Mass of (CO)		Mass of THC		Mass of NMHC		Mass of NO_x		Mass of THC+NO_x		Mass of PM_x		Number of P	
			L_1 (mg/km)		L_2 (mg/km)		L_3 (mg/km)		L_4 (mg/km)		$L_2 + L_4$ (mg/km)		L_5 (mg/km)		L_6 (#/km)	
Cat	Class		PI	CI	PI	CI	PI	CI	PI	CI	PI	CI	PI	CI	PI	CI
M		All	1000	500	100	–	68	–	60	80	–	170	5/4.5	5/4.5		$6x10^{11}$
N_1	I	RM≤1305	1000	500	100	–	68	–	60	80	–	170	5/4.5	5/4.5		$6x10^{11}$
	II	1305<RM ≤1760	1810	630	130	–	90	–	75	105	–	195	5/4.5	5/4.5		$6x10^{11}$
	III	1760<RM	2270	740	160	–	108	–	82	125	–	215	5/4.5	5/4.5		$6x10^{11}$
N_2			2270	740	160	–	108	–	82	125	–	215	5/4.5	5/4.5		$6x10^{11}$

Table 1.1 and Table 1.2 report the emission limits established by the European Union in 2007 (Euro 5/6 Standards, 2007), in relationship to the reference mass (RM), defined as the mass of the vehicles in running order less the uniform mass of the driver of 75 Kg and increased by a uniform mass of 100 Kg.

It is possible to note that Euro 6 differs from Euro 5 for more stringent limits on the emissions of oxides of nitrogen. For the number of particles emitted, a standard limit was defined in the final draft version (18.09.2007) of the regulation (EC) No 715/2007 of the European Parliament and of the Council of 20 June 2007 (Euro 5/6 Standards, 2007).

1.5.2 Emissions by flames and soot formation pathway

Emissions by internal combustion engines are complex mixtures which depend on engine operation, fuel composition, lube oil, after-treatment technology and exhaust sampling procedure. Laboratory flames, which are relatively simple to study both experimentally and computationally, offer an environment to investigate carbonaceous PM formation in high T combustion processes.

Carbonaceous PM formation by combustion is a complex process which involves the decomposition of the fuel and the subsequent formation of aromatic hydrocarbons with one to three benzenoid rings. Specifically five important steps can be identified (McEnally *et al*., 2006), which involves first gas-phase and then solid-phase chemistry:

- Fuel decomposition;
- Small aromatic hydrocarbons formation;
- Growth of the small aromatics to compounds containing large numbers of rings;
- Inception of small soot particles from the large aromatic hydrocarbons;
- Growth of the small particles to particles with larger masses

[2] Nomenclature: RM=Reference Mass; CO=Carbon Monoxide; THC=Total Hydrocarbon; NMHC=Non-Methane Hydrocarbons; NO_x=Oxides of Nitrogen; PM=Particulate Matter; P=Particles; PI=Positive ignition; CI=Compression ignition; Category M=vehicles designed to fulfill specific social needs;

All of the steps are important research topics with a wide literature on each topic. PM formation can not be described as a global reaction. Reaction pathways that describe the entire process from fuel decomposition to the first incipient particles must be modeled with detailed chemical kinetic mechanisms (Frenklach & Wang, 1991; D'Anna *et al*., 2001).

The carbonaceous particles formation starts with the oxidation and pyrolysis of the hydrocarbon fuel, thus producing small fragments which can either form oxidation and pyrolysis products or cycle to form the first aromatic ring, namely benzene or phenyl radical.

The formation of naphthalene, the first compound in the PAH series, mainly follows two routes. The first route is the popular HACA (H-abstraction-C_2H_2-addition) mechanism (Frenklach & Wang, 1991), characterized by the sequential addition of acetylene (C_2H_2) to phenyl radical. The second route is the combination of resonantly-stabilized radicals, specifically two cyclopentadienyl radicals (Marinov *et al*., 1996; Castaldi *et al*., 1996) or the combination of benzyl and propargyl radicals (Colket *et al.*, 1994).

The dividing line between the small and large aromatics is usually ~3 benzenoid rings. At this point of the process, these small aromatics, and also acetylene, constitute the building blocks for the subsequent growth process which lead to the formation of intermediate compounds, such as peri-condensed aromatic hydrocarbons (PCAH) and aromatic-aliphatic-linked hydrocarbons (AALH) (D'Anna, 2007). These compounds containing large numbers of aromatic rings continue to grow to form agglomerates of a few nanometers in diameter held together by weak van der Walls forces. The formation of macromolecular species whose size is on the order of a few nm marks the onset of *particle inception*.

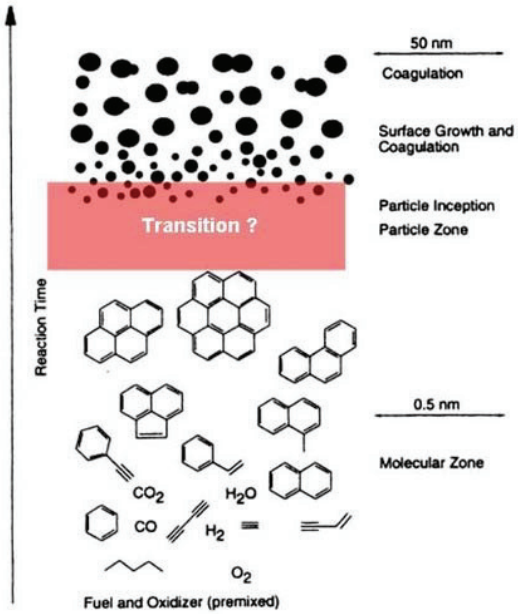

Figure 1.3 Theoretical soot formation mechanism, adapted from Bockhorn (1994)

According to different investigations, particle inception takes places at different molecular masses between 300 and 2000 amu. (Miller, 1990; Pfefferle *et al*., 1994; D'Anna *et al.*, 1994).

The subsequent steps in the soot particle formation are coagulation and surface growth. Coagulation is the result of colliding macromolecules/nanoparticles to produce new spherical structures. The rate of coagulation depends on the size of the colliding particles: small particles, characterized by a large Knudsen number[3] (Kn>>1), evolve in the free molecular regime; larger particles, characterized by a small Knudsen number (Kn<<1), evolve in the continuum regime (Friedlander, 1977). Surface growth is the result of chemical reactions, involving molecules in the gas phase and molecules on the surface of the particle, such as adsorption and desorption processes. Acetylene and aromatics are well accepted to be the main species responsible for mass addition on the surface of a particle. Also oxidation is in principle a surface reaction. In this case, however, hydroxyl radical and oxygen remove mass from the particles and form CO and HCO. The last step of soot formation is the agglomeration which produces cluster or chain-like agglomerates.

1.5.3 Incipient nanoparticles

As displayed in Figure 1.3, particle inception at high temperature still remains the not-well understood step in the process of soot formation. Therefore, the question of soot precursor particles has received considerable interest in the last decades. The availability of high-performance instruments, with increased sensitivity to species in the 10^3-10^5 amu (or 1-5 nm size range), has produced significant progress in understanding particle inception. In the early 90s, Dobbins *et al.* (1987, 1994) and D'Alessio *et al*. (1992) provided preliminary reports on the existence of nanoparticles in the sub-nanometer size range with liquid-like properties and size and properties different from the larger soot particles. More recently, the existence of high molecular mass flame generated particulate material with equivalent spherical sizes down of 2-3nm is well documented by independent measurements with different diagnostic techniques: in situ optical measurements (D'Alessio *et al*., 1992, 1998; Minutolo *et al*., 1994, 1999; D'Anna *et al*., 2005*,* 2007, 2008), off-line Atomic Force Microscopy (AFM) (D'Alessio *et al*., 2005; Barone *et al*., 2003), Transmission Electron Microscopy (TEM) (Dobbins & Subramaniasivam, 1994; Dobbins & Megaridis, 1987; Dobbins, 2007), probe sampling and off-line chemical characterization (Ciajolo *et al.*, 1994, 1996, 1998), probe sampling on line Differential Mobility Analyzer (Thierley *et al*., 2007; Sgro *et al*., 2007a; Zhao *et al*., 2003) and molecular beam mass spectroscopy (Thierley *et al*., 2007; Weilmunster *et al*., 1999; Bachmann *et al*., 1996), and ex-situ and in-situ Time Resolved Fluorescence Polarization Anisotropy (Bruno *et al*., 2007, 2008). These incipient nanoparticles were named precursor nanoparticles (PNP) by Dobbins and Nano Organic Carbon (NOC) by the Naples research group lead by D'Alessio.

Very recently, Dobbins (2007) and D'Alessio *et al.* (2007) have also reported detailed reviews on the properties, behaviors and structures of this combustion-generated particu-

[3] Knudsen number is defined as a dimensionless number equal to the ratio of the mean free path to the particles radius, Kn= $2\lambda/d$. λ=0.066 μm for air molecules at standard conditions (Hinds, 1998).

late matter. Table 1.3 reports the main differences between NOC and soot formed in atmospheric hydrocarbon flames.

Table 1.3 – **Main differences between NOC and soot, adapted from D'Alessio *et al.* (2007)**

NOC	**Soot**
Extinction in the far UV	Extinction in the entire UV-visible wavelength range
UV fluorescence	UV-visible fluorescence
$D_{6\text{-}3}$ =3 nm	$D_{6\text{-}3}$ >3 nm
Soluble in dichloromethane	Not soluble in dichloromethane
Affinity with water	Not soluble in water
Coagulation rate < collision rate	Coagulation rate = collision rate
Low sphericity	Higher sphericity approaching 1
Semi transparent to the electron beam	Clear Electron Microscope images
H/C=0.5-1	H/C=0.1-0.05
Density=1.2 g/cm^3	Density=1.77-1.8 g/cm^3
Measured in fuel rich blue flames	Not measured in fuel rich blue flames
Emissivity=0.5	Emissivity=1
High mutagenic potency	Non-mutagenic in Ames and other mutagenicity assays

1.6 Specific discussion: definition of particle diameters

For a spherical particle of unit density, the size can be simply characterized by the geometric diameter (d_p). However, atmospheric particles can have arbitrary shape and density. Therefore their diameters are described by an equivalent diameter, defined as the diameter of a sphere that would have the same physical behavior as the particle in question (US EPA, 2004). The appropriate particle size definition depends primarily on the type of measurement made (John, 2001):

- *Aerodynamic diameter* (d_a) = The aerodynamic diameter is defined as that of a spherical particle of unit density having the same settling velocity as the particle in question. It is usually used to analyze the data from a cyclone, a cascade impactor, an Electrical Low Pressure Impactor (ELPI) and an Aerodynamics Particle Sizer (APS)
- *Diffusive diameter* (d_d) = The diffusive diameter is the diameter of a particle of unit density having the same rate of diffusion as the particle in question. This diameter would be used for a diffusion battery measurement
- *Stokes diameter* (d_{St}) = The Stokes diameter describes particle size based on the aerodynamic drag force imparted when its velocity differs from that of the surrounding fluid. The Stokes diameter is the appropriate parameter for

particle behavior governed by diffusion because the particle diffusion coefficient and Brownian diffusion velocity can be related through the Stokes-Einstein equation. The Stokes diameter would be used in size distributions based on light scattering and mobility analysis. In the latter, a Differential Mobility Analyzer (DMA) classifies particles according to their electrical mobility; thus particles of equal Stokes diameters that carry the same electrical charge will have the same electrical mobility. For spherical particles, the electrical mobility diameter would equal the Stokes diameter. The *mobility diameter* (d_m) can be considered the diameter of a spherical particle that would have the same electrical mobility. To correlate the mobility diameter with the actual diameter (geometric diameter of known spherical particles), it is necessary to consider an effective diameter (d_o) of the gas in which the aerosol is immersed for the measurement:

$$d_m = d_p + d_o \qquad (1.1)$$

For air at standard conditions, Fernandez de la Mora et al. (2003) experiment ally measured a value of do~0.53 nm, not far from Tammet's estimated 0.6 nm (Tammet, 1995) and in good agreement with a more general relationship derived by Li & Wang (2003) who considered the potential energy of inter actions between particles and gas molecules in terms of the reduced collision integral.

- *Optical diameter* (d_{OP}) = The optical diameter is defined as the diameter of a calibration particle having the same response in an instrument detecting particles by their interaction with light, namely that scatters the same amount of light into the solid angle measured. The optical diameter would be used with an Optical Particle Counter (OPC).
- *Equivalent spherical diameter(ESD)* = The equivalent spherical diameter of an irregularly-shaped object is the diameter of a sphere of equivalent volume (Jennings & Parslow, 1988). This would be used with an Atomic Force Microscopy (AFM).
- $d_{6\text{-}3}$ =This mean particle diameter is given by the ratio between the sixth and third moments of the particles number distribution function.

1.7 Specific discussion: particle size distribution functions

Monodisperse aerosols have a single mode of particles that are all contained within a narrow size range, and are usually generated in laboratory. Aerosols containing a wide range of particle sizes are said to be *polydisperse* (Hinds, 1999). The mathematical description of particle size distributions is characterized by very fine successive size intervals, each of them containing a counted number of particles. Because the dependent variable, or the ordinate of the plot, is the number of particles, such a distribution is called a *number distribution* (John, 2001). If N(dp) is the number of particles in the size interval centered between d_p and d_p+dd_p, where d_p is the particle number, the number distribution is

$$dN = N(d_p)\, dd_p \qquad (1.2)$$

Because the particle diameter typically ranges over several orders of magnitude, it is common to use $\mathrm{dln}d_p$ (or $\mathrm{dlg}d_p$) for the size interval, and the number distribution becomes

$$\mathrm{dN} = \mathrm{N}(d_p)\,\mathrm{dln}d_p \qquad (1.3)$$

Similarly, frequently used size distributions are the *surface distribution*, the *volume distribution* and the *mass distribution*:

$$\mathrm{dS} = \mathrm{S}(d_p)\,\mathrm{dln}d_p \qquad (1.4)$$
$$\mathrm{dV} = \mathrm{V}(d_p)\,\mathrm{dln}d_p \qquad (1.5)$$
$$\mathrm{dM} = \mathrm{M}(d_p)\,\mathrm{dln}d_p \qquad (1.6)$$

The data for one of the above distributions might be obtained directly by an appropriate analyzer or indirectly by the measured number distribution. The total particle number concentration is expressed as:

$$N_{TOT} = \sum_i N\left(d_{p,i}\right) \qquad (1.7)$$

Assuming the particle as spherical, the total volume fraction is expresses as:

$$FV_{TOT} = \sum_i \left[\sum_i N\left(d_{p,i}\right) \cdot \left(\frac{\pi}{6}\right) \cdot \left(d_{p,i}\right)^3 \right] \qquad (1.8)$$

It is necessary to know the density, ρ, of the particle to obtain the total mass from the total volume fraction.

Other useful parameters that are calculated from the size distributions are:

- the *mean arithmetic diameter*, $\bar{d} = \dfrac{\sum_i N\left(d_{p,i}\right) \cdot d_{p,i}}{\sum_i N\left(d_{p,i}\right)}$.
- the *median diameter* defined as the diameter for which one-half the total number of particles are smaller and one-half larger
- the *mode diameter* defined as the diameter associated to the peak of the log-normal distribution
- the *mean geometric diameter* (d_g), $\log d_g = \dfrac{\sum_i N\left(d_{p,i}\right) \cdot d_{p,i}}{\sum_i N\left(d_{p,i}\right)}$.
- the *geometric standard deviation* (σ_g),

$$\log \sigma_g = \left[\frac{\sum_i N\left(d_{p,i}\right) \cdot \left(\log d_g - \log d_i\right)^2}{\sum_i N\left(d_{p,i}\right) - 1} \right]^{1/2}$$

Second Chapter

Experimental apparatus: analysis systems

2.1 Introduction

In this thesis, commercially available instruments were used to measure the size distribution of nanoparticles emitted from premixed laboratory flames, two light-duty diesel vehicles, a test bench single-cylinder engine and common burners. Figure 2.1 gives a schematic view of the experimental apparatus. An Electrical Mobility Spectrometer (EMS) and a Scanning Mobility Particle Sizer (SMPS) were employed to determine particle size distributions with particular attention to the 1-10 nm range. These diagnostic techniques are based on the Differential Mobility Analysis (DMA) which furnishes the possibility of determining the size distribution of nanoparticles resolved in space and time at the exhaust of a generic combustion source. The combustion-generated aerosol was diluted and transported to the analysis system via sampling devices which were designed to minimize effects on the sampled aerosol to avoid sampling artefacts.

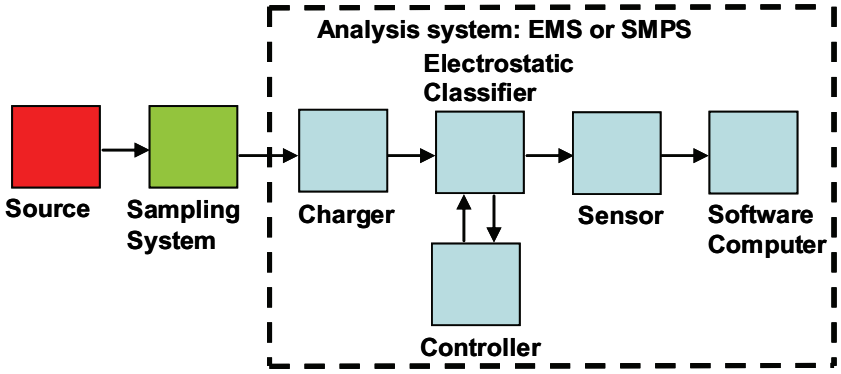

Figure 2.1 – General sketch of the experimental setup

Different types of sampling and analysis systems were used. Table 2.1 reports a summary of the instruments employed. Tests of premixed laboratory flames were mainly conduced with the combined use of a sampling probe, horizontally positioned above the burner surface, and a tapcon EMS (3/150 DMA) of particular design (Sgro *et al.*, 2007a; tapcon & analysesysteme GmbH, Winklmayr *et al.*, 1991, Reischl, 1991). In some cases home-made ejector probes, vertically positioned above the burner surface, and a TSI SMPS (equipped

with TSI 3085 nano DMA) were also employed (Tsi Incorporated). The latter, in combination with a series of one or two ejector pump diluters (Dekati, Ltd.), was also used to test the emissions of light-duty diesel vehicles. The tapcon EMS was again employed to investigate nanoparticles emitted from test bench single-cylinder engine and common gas burners.

This chapter gives a detailed description of each of the aforesaid analysers, comparing their main characteristics and evaluating experimentally their analogies and differences. On the other hand, Chapter 3 focuses on the different sampling devices employed.

Table 2.1 – **Summary of the analysis and sampling systems**

Source	Analysis System	Sampling/dilution device	Laboratory[1]
Premixed Laboratory Flames	-tapcon EMS -TSI SMPS	-Horizontal probe -Ejector probe	-DIC Napoli -CDB Berkeley
LD Diesel Vehicles	-TSI SMPS	-Dekati Diluter	- FORD's VERL Dearborn
Test bench engine	-tapcon EMS	-Dekati diluter	-IM CNR Napoli
Common burner	-tapcon EMS	-Ejector probe	-DIC Napoli

2.2 Analysis systems: Electrical Mobility Spectrometer and Scanning Mobility Particle Sizer

2.2.1 Classification by electric mobility: general features and theory

Electrical Mobility Spectrometers and Scanning Mobility Particle Sizers are useful experimental tools for the study of the emissions of carbonaceous ultrafine and fine particles since, in principle, they furnish the measure of the size distribution of aerosols in size ranges from 1 to 1000 nm. As schematically displayed in Figure 2.1, both the sampling systems are generally made of five main components: a charger which brings the polydisperse aerosol sample to a well defined "steady-state" (size dependent) charge distribution (Adachi *et al.*, 1983; Wiedensohler *et al.*, 1986; Wiedensohler, 1988), a controller to control flows and high-voltage, an electrostatic classifier which separates the particles on the basis of their electrical mobility, a sensor which measure the particle concentration and a customized software to control individual instruments, collect and store sample data.

Specifically, polydisperse aerosol, entering the charger, receive either a unipolar charge in the case of unipolar charger (ionizer) or positive, negative or zero charge in the case of a radioactive bipolar charger (neutralizer). The latter establishes a steady-state bipolar equilibrium charge level on the particles which is well-predicted by Fuchs theory for

[1] DIC = Dipartimento di Ingegneria Chimica dell'Università "Federico II" di Napoli; CDB = Chemical Dynamics Beamline at Lawrence Berkeley National Laboratory in Berkeley (California); VERL= Vehicle Emission Research Laboratory at Ford Research and Innovation Center in Dearborn (Michigan); IM CNR= Istituto Motori del Consiglio Nazionale delle Ricerche in Napoli.

particles larger than 2nm (Reischl *et al*., 1996) or 2.5 nm (Alonso *et al*., 1997b). The particles then enter the electrostatic classifier (EC) where they are classified by their ability to transverse an electric field, namely by their electrical mobility. Thus, in this case, the classifier is referred as the differential mobility analyzer (DMA).

The DMA employs a cylindrically symmetric electric field applied to the electrostatic classifier to separate the charged aerosol particles. A stainless steel cylinder constitutes the outer electrode with a metal rod, lined along its axis, working as the inner electrode of the EC. The sample charged aerosol enters the outer periphery of the classifier and mixes with a larger laminar sheath of particle free air, Q_{sh}, which flows through the annular cavity between the two electrodes, with inner radius, R_1, and outer radius, R_2. The electric field applied across the central rod and outer cylinder attracts the opposite polarity of particles toward the rod. Particles with a narrow range, ΔZ, of electrical mobility have the proper trajectory to travel from the aerosol inlet to the exit aperture (distance of the travel, L) and enter the sensor for the subsequent detection. Thus, the size distribution is calculated from the distribution of Z (V), while varying the applied voltage or the electric field in the classifier, in terms of mobility diameter, d_m[2], by the Millikan-Fuchs' equation, which is valid for spherical particles:

$$Z = \frac{Q_{Sh}}{2\pi \cdot V \cdot L} \ln(\frac{R_2}{R_1}) = \frac{q \cdot e \cdot C_c}{3 \cdot \pi \cdot \mu \cdot d_m} \qquad (2.1)$$

where q is the number of charges on the particles, e is the unit charge, and μ is the viscosity of the carrier gas. The Cunningham correction factor, C_c, is a function of the Knudsen number (Hinds, 1999), $C_c=1+Kn[\alpha+\beta \cdot exp(-\gamma/Kn)]$[3]. The classified particles are then counted and their concentration is measured by a Condensation Particle Counter (CPC), in the case of an SMPS, or by an Electrometer, in the case of the EMS.

With the CPC, condensation of supersaturated vapors (e.g. n-butyl alcohol) is used to grow particles to sizes that can be detected and counted by a simple optical detector (McMurry, 2000a). Commercially available instruments can detect particles as small as 3 nm in diameter (e.g. TSI CPC 3025A) (Kesten *et al.*, 1991). The advantage of CPCs is that they count single particles and hence very low concentrations like those found in clean rooms of atmospheric concentrations. By contrast, the electrometer requires enough particles to provide a significant current above electrical noise. With the CPC, particles are counted individually and therefore the minimum concentration that can be detected is limited only by instrument noise and by counting time. The disadvantage is that its counting efficiency is a strong function of particle size such as that most CPCs have near 100% efficiency for sizes larger than 5 nm and near 0% efficiency below 2-3 nm [Stolzenburg *et al.*, 1991; Wiedensohler *et al*., 1997; Mavliev & Wang, 2000). Further problems are introduced by a dependency on the composition of the particles and their physical and chemical surface properties (Petzold *et al*., 2005).

With the Electrometer, the current delivered by charged particles is measured by a Faraday Cup (Flagan, 1998). The particle concentration, N_{ae}, is obtained from the aerosol electrometer current, I, using the following relationship:

[2] $d_m = d_p + 0.5$ (see Equation 1.1 and relative discussion)
[3] $\alpha = 1.142$, $\beta = 0.558$, $\gamma = 0.999$ (Allen & Raabe, 1985)

$$N_{ae} = \frac{I}{Q \cdot e} \qquad (2.2)$$

where Q is the volumetric flow rate through the electrometer, e is the charge per electron, and number of charges per particles is equal to 1. The advantage of the Electrometer is to provide an independent measurement that does not rely on condensation and on the particle size. Furthermore, to minimize losses in tubing, the electrometer housing is mounted at the aerosol outlet of the DMA. The complication is that multiply charged particles having the same mobility as the desired singly charged particles may be included with the aerosol leaving the DMA and inversion schemes to calculate size distributions from mobility distributions must consider also the charge distribution on the measured aerosol. Multiple charging becomes important only at larger sizes, 20 nm in diameter (Flagan, 1998), with respect to the size range examined in this thesis.

To operate the spectrometer it is necessary to control several gas flows through the DMA and the particle sensor. The performance of the DMA is critical to the stability of these flows which are generally supplied from a flow control unit. The control of the electrode voltages and the reading of the particle sensor is done by dedicated electronics and a micro computer, which is also used for data reduction, display and storage.

2.2.2 tapcon EMS DMA 3/150 & TSI SMPS 3936: analogies and differences

The two types of analysis systems, which were used in this thesis, were manufactured respectively by tapcon & analysesysteme GmbH and by TSI Incorporated. Both consisted of a cylindrical DMA and the main differences are the particle sensors employed and the flow rates through the instruments, both of which determined the lower size detection limit.

More specifically, the tapcon EMS was the last development of the previous version distributed by the Aerosol Measurement Division of Hauke, also known as Wien Type DMA or “Vienna” DMA in the literature. The EMS was equipped with a bipolar radioactive (Am-241) diffusion charger (Winklmayr *et al.,* 1991) and a DMA 3/150, characterized by a superior flow profile to furnish a clean size separation, low diffusional losses and, in principle, a wide range of applicable aerosol (1-10 L/min) and sheath gas flows (10-50 L/min) depending on the critical orifices in the flow control unit. With the aerosol flow at 5L/min and the sheath flow at 50 L/min, the particle size regions achieved by the instrument were 0.6-28 nm and 2-100 nm with high voltage respectively at 1250 V and at 12500 V. The highly stable gas flows were assured by critical orifices rather than electronic mass flow controlling devices. The classified particles were measured by a Faraday Cup Electrometer (FCE-08) and the EMSSYS operating software converted the measurement data to the size distributions and displayed on-line, besides controlling the different hardware components of the EMS system. The size distributions were calculated as dN/dln*D*, including the size dependent charging probability in air for single charge and a correction function reflecting the slip correction and the instrument resolution (transfer function). Correction for instrument losses was not included and no impactor was used.

On the other hand, in the TSI SMPS systems used for this thesis, the aerosol sample first passed through a single stage inertial impactor which served to remove larger particles and to control the aerosol inlet flow (nozzle sizes of 0.0508 cm and of 0.071 cm were al-

ternatively used). Then the aerosol was charged by a bipolar radioactive neutralizer (TSI Kr-85 and also NRD Po-210[4]), required to establish a known charge on the particles entering into the classifier. The latter (TSI Model 3080) accommodated the Model 3085 Nano DMA, able to cover a broad range of particle diameters from 2 to 150 nm. The design of the Nano DMA reduced the effects of diffusion (by reducing the residence time of particles in the classification zone) and promoted axisymmetric aerosol flow, thus reducing distortions of the flow field. The classified particles were counted by the TSI CPC 3025A which measured the particle concentration. Because of the very low detection efficiency of CPC for small particles, the lower cut off limit for the size distribution function reported by the TSI Aerosol Instrument Manager (AIM) is 3 nm as mobility diameter. The size distribution was calculated as dN/dlg*D* and the main advantage in using the TSI SMPS is that the software also enabled a mathematical correction for particles with multiple charges and for particle diffusion losses. However, since the flow rates are substantially lower, particle losses may be higher and of course if no particles arrive to the detector because they are all lost within the instrument, the raw counts is 0 and the correction is useless. Extension of the lower detection limit down to 2 nm was possible by determining the size distributions from raw counts (Minutolo *et al.*, 2008).

Table 2.2 summarizes the main characteristics for two specific analyzers employed.

Table 2.2 – **Comparison of two analysis systems: main components**

	tapcon EMS	**TSI SMPS**
Model	VIE-09	3936
Bipolar Ionizer	^{241}Am, $t_{1/2}$ = 458.6 years, 3.24 mCi, α-radiation	^{85}Kr, $t_{1/2}$ = 10.8 years, 2 mCi, β-radiation
Classifier	L=109mm, R_1=25mm, R_2=33mm (DMA 3/150)	L=49.87mm, R_1=9.37mm, R_2=19.05mm (TSI Nano DMA 3085)
Flow rates	Qa= 5 lpm, Qsheath= 50 lpm	Qa= 1.5 lpm, Qsheath= 10 lpm *dual blower mode*
Sensor	Faraday Cup Electrometer	Condensation Particle Counter (TSI CPC 3025 A)
Nominal size range	0.6-28 nm	2-63 nm
Scan time	170s	75 s = 60+15 s (retrace time)

2.2.3 tapcon EMS DMA 3/150 & TSI SMPS 3936: experimental comparison

An experimental investigation on the efficiencies of the two systems to detect the full range of molecular clusters/nanoparticles in the gas-to-particle conversion processes (as small as about 1nm) in a flame environment was also made. Table 2.2 reports their main characteristics. The two analysis systems were simultaneously used to measure the size distributions of nanoparticles emitted from premixed ethylene air flames (cold gas velocity=

[4] NRD, Inc., 2937 Alt Boulevard, PO Box 310, Grand Island, NY 14072 USA (www.nrdinc.com).

10 cm/s) with carbon to oxygen ratio (C/O) in the range from 0.6 to 0.67, just before the on set of soot formation. The flat premixed flames were stabilized on a water cooled sintered bronze McKenna burner (d=60mm).

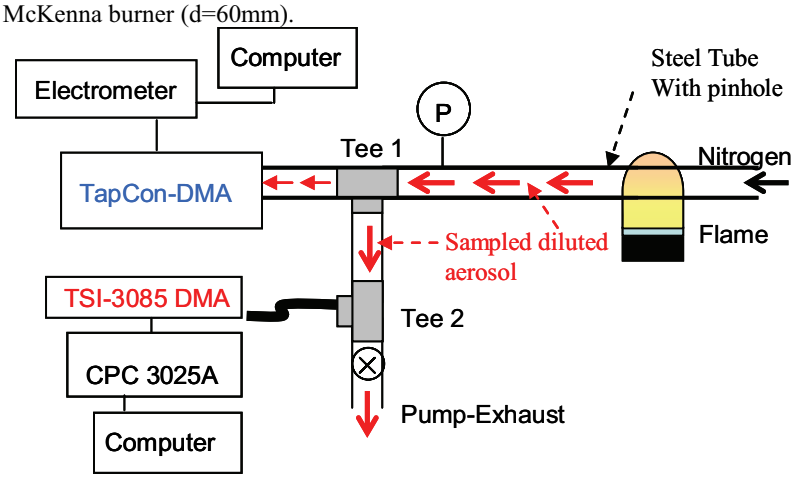

Figure 2.2 – Experimental set up for on-line DMA measurements in premixed flames.

The tapcon EMS and the TSI SMPS sampled the diluted aerosol in parallel downstream of the sampling/dilution system, as schematically described in Figure 2.2. The sampling system was the same as described by Sgro *et al.* (2007a) and its characteristics will be discussed in the following chapter. The distances from Swagelok Tee 1 and inlet of the two analysis systems were slightly different, with the TSI SMPS positioned on the exhaust line in correspondence of a second Swagelok Tee. Thus to exclude effects due to the different configurations, tests were also made inverting the position of the two analysis units. In both cases, the diluted and cooled sample was transported from the Swagelok tee to the TSI Nano DMA at 1.5 L/min through a 63 cm-long, 0.5 cm inner diameter electrically conductive tube. Since diffusion losses become significant for particle size below 20 nm, they were evaluated in this tube using the equation for penetration in a circular tube for laminar flow (Hinds, 1999; Alonso *et al.*, 1997a; Gormeley *et al.*, 1949). No bypass flow was used with the TSI SMPS.

With the TSI SMPS, size distributions were stored as dN/dlgD, including the mathematical correction (provided by AIM software) for particle diffusion losses within the SMPS (Panel A in Figure 2.3), and also as raw counts, in order to estimate the particle concentration down to 2nm (Panel B in Figure 2.3). Analysis of raw counts effectively demonstrated that a signal below the instrument limit (3 nm) is measured, and is above the value attributable to noise which is randomly measured in the 3-63 nm size range. Therefore it was possible to extend the particle size distribution in the 2-3 nm size range following the approach described in details by Minutolo *et al.* (2008). On the other hand, with the tapcon EMS, only measured particles larger than 1.4 nm were considered (see discussion in the next section).

As the dilution ratio was kept constant (~10^4) and equal for the times required for both the measurements, the compared data between tapcon EMS and TSI SMPS refer to the par-

ticle concentration measured by the sensors (and not at the sampling points/flame), both expressed in terms of dN/dlnD (see Figure 2.4).

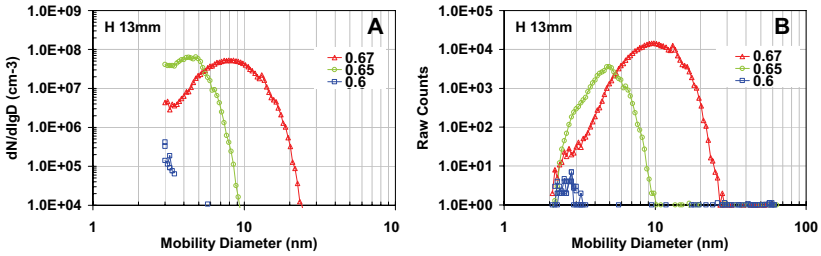

Figure 2.3 – Signals stored by TSI SMPS when sampling from three premixed ethylene-air flames (C/O=0.6, 0.65, 0.67) with the horizontal probe positioned at H=13mm above the burner. Particle size distributions corrected for diffusion losses within the SMPS (Panel A) and raw counts (Panel B) without any correction.

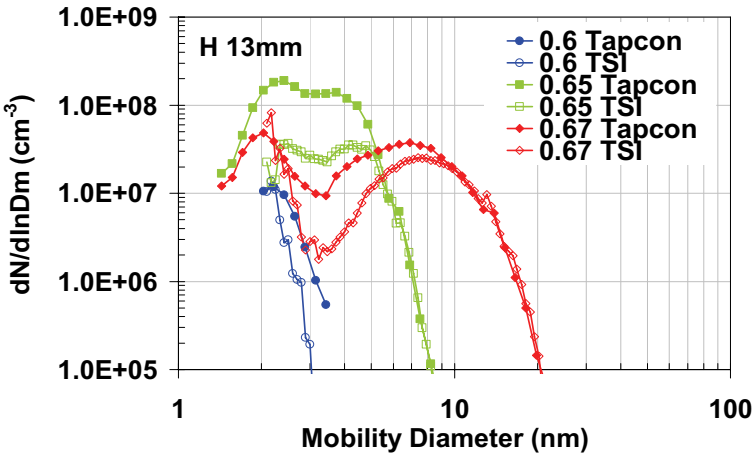

Figure 2.4 – Particle size distributions simultaneously measured from three premixed ethylene-air flames (C/O00.6, 0.65, 0.67), with the horizontal probe positioned at H=13mm above the burner, employing the tapcon EMS (full symbols) and the TSI SMPS (empty symbols). Data are not corrected for dilution and losses in the probe but those of TSI are corrected for losses in the additional path (conductive tube).

At higher C/O ratios, both the systems measured a bimodal size distribution. In the case of the C/O=0.65 flame (green symbols), the first mode was at about 2.4 nm and the larger mode at about 4 nm while, for the C/O=0.67 flame (red symbols), the first mode was at about 2nm and the second mode at about 7nm. It is also worth noting that a slight shift (less than 0.5nm) in the modal diameters was also observed, with the TSI SMPS measuring the larger size. In addition, there was quantitative agreement for particles larger than 5 nm. This result matches similar comparison presented by Sgro *et al.* (2007a) on two independent measurements of the particulate emitted from the same slightly sooting flame. For the

C/O=0.65 flame, the particle size distributions show that, below 5 nm, the tapcon EMS was able to detect a particle number concentration five times higher than that measured by the TSI nano SMPS. As already addressed, the overall shape of the size distribution was instead similar in the two cases. For the richer C/O=0.67 flame, the results again indicate that the tapcon EMS measured a higher signal for particles smaller than 9nm but, in this case, in correspondence of the two modes there was a good quantitative match between the two analyzers. The discrepancy for the C/O=0.67 case mainly involved the size range of the dip between the two modes.

At lower C/O ratio, namely C/O =0.6, where all the measured signals are below 3 nm, the correction included in the TSI data to extend the lower detection limit down to 2nm seems to be reasonable and there is a good qualitative agreement between the two sets of data: the tapcon data were two times higher than those from TSI except for the signal at 2 nm where they both matched.

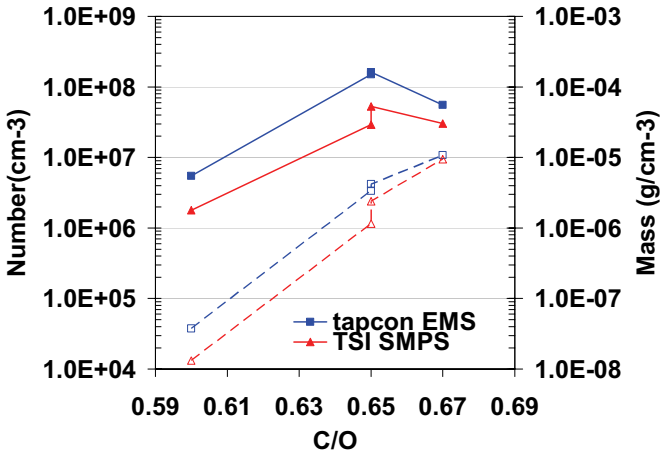

Figure 2.5 – Particle number concentration (primary axis, solid lines) and mass concentration (secondary axis, dotted lines)for the tapcon EMS (blue colors) and TSI SMPS (red colors).

Figure 2.5 shows the number and the mass concentration (assuming ρ=1.2 g/cm^3) calculated from the integral of the size distributions of Figure 2.4. Number and mass are respectively displayed as full line-full symbols and dotted line-empty symbols while blue and red colors refer to tapcon and TSI. While the mass concentration increases with almost a constant slope in the C/O range investigated, the number concentration increases from C/O=0.6 to C/O=0.65 and then decreases from C/O =0.65 to 0.67, which is in proximity of the C/O where optical spectra indicate the presence of first soot particle.

Moreover the extra (and higher) points at C/O=0.65 are those calculated from the size distributions in the tests with two analyzers inverted with respect to the position displayed in Figure 2.2. As expected, inverting the position of the two analyzers produced a slightly higher (but less than two times) signal for the TSI but it did not affect at all the signals from the tapcon EMS. As consequence, switching the position of the two analyzers did not produce significant changes.

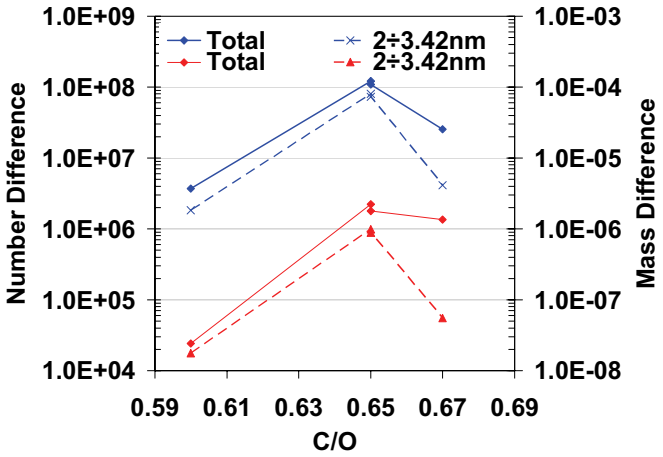

Figure 2.6 – Difference in the total (full lines) and partial (dotted lines) number concentration (primary axis, blue colors) and mass concentration (secondary axis, red colors) of the tapcon EMS data versus the TSI SMPS data.

Figure 2.6 & Figure 2.7 add further information to this comparison. In Figure 2.6, primary axis shows the difference of number concentration (blue symbols), integrated both along the entire size range (full line) and in the 2-3.42nm size range (dotted line). Instead secondary axis refers to the difference of mass concentration (red symbols). It is interesting to note that the difference (signal from tapcon minus signal from TSI) increases in the step from C/O=0.6 to C/O=0.65 and then decreases in the step from C/O=0.65 to C/O=0.67. In addition, the largest difference coincides where the particle number concentration of both modes is the highest.

In order to include further measurements at C/O=0.63 and C/O=0.65, both at H=10mm, and measurements at different heights above the burner in the C/O =0.65 flame, the number difference is also plotted versus the number concentration as measured by the tapcon EMS (Figure 2.7). In Figure 2.7, the four data at H=13mm discussed in Figure 2.4, 2.5 & 2.6 are displayed in blue symbols; the two data at H=10mm are displayed with green symbols and the eight data at C/O=0.65 for different heights are displayed with red symbols. Most of the data correspond to a number concentration of ~ $2*10^8$ and this produces an overlapping of some of them. The main information achieved by the plot in Figure 2.7 is that the difference, in terms of particle number concentration, between tapcon EMS and TSI SMPS linearly increases with the total particle number concentration of the aerosol.

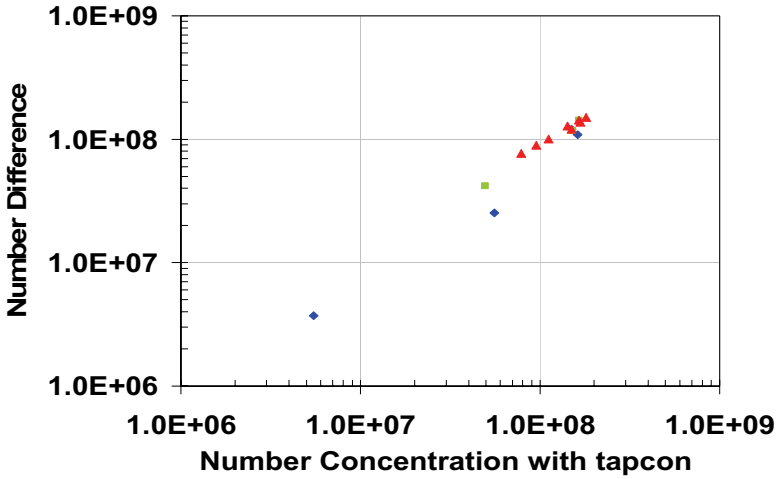

Figure 2.7 - Difference in the total number concentration measured with the tapcon EMS data versus the TSI SMPS data for different particle concentration measured with the tapcon EMS.

At a first sight, this result seems to indicate that the main factor that explains the discrepancy between the two analyzers is the different bipolar neutralizers used (since is the only among the possible factor that have a strong dependence on number concentration) but it is necessary a further investigation covering a wider range of particle number concentration, a wider range of flames and different levels of radiation. In fact, for this specific analysis, the bipolar analyzer used (TSI Kr-85) had a level of radiation of 2.0 mCi which is a lower strength Kr source with respect to the latest version provided by TSI (10 mCi) which was not available at the time of this investigation. Therefore, whether the reasons for this discrepancy were the different chargers used (with ion density generated by alpha decay, in the case of the tapcon EMS, and by beta-radiation, in the case of the TSI SMPS, and also characterized by different geometries and intensity of radiation) or the efficiency of the sensors or the design and operating conditions of the two classifiers or the transport losses to the DMAs (e.g., a bypass flow used with the TSI SMPS would help to reduce significantly the residence time in the bipolar charger (Maricq, 2004)) remain still unknown and a definitive explanation require a more focused investigation which was not the main objective of this thesis.

In any case, it is clear that the tapcon EMS configuration was able to detect smaller nanoparticles (below 5 nm) more than the TSI SMPS instrumentation, in better qualitative and quantitative agreement (once corrected for the dilution factor of ~ 10^4) with earlier observations made using atomic force microscopy (D'Alessio *et al.*, 2005) and in situ light scattering and extinction in the ultraviolet and visible wavelengths in similar slightly sooting flames (Minutolo *et al.*, 1999; D'Alessio *et al.*, 1998).

2.2.4 tapcon EMS DMA 3/150: sub-nanometer peak

With the tapcon EMS configuration, a sub-nanometer peak, slightly smaller than 1nm, was always present in the measured size distributions. This peak was voluntarily not displayed in Figure 2.4 and was not accounted for the calculations reported in Figure 2.5 and Figures 2.6. The nature of the first peak is ambiguous since it may be due both to carbon compounds with molecular mass of about 300-700 amu[5] produced in combustion, or ion-induced molecular clusters produced in the bipolar particle charger have a similar size in mobility diameter, contributing greatly to the number of particles measured smaller than 1.4 nm (Winklmayr *et al*., 1991; Parts, 1996).

In Figure 2.8, Panel A displays the signal measured by the electrometer corresponding to the size distribution measured when testing the C/O=0.67 flame, already displayed in Figure 2.4 (red symbols). With respect to Figure 2.4, Figure 2.8 (both Panel A and B) reports the data with the x-axis extended to the lower limit of the tapcon EMS, namely below 1nm in terms of mobility diameter (d_m). The x-axis is arbitrarily modified to have a direct comparison between the mobility diameters (d_m), the actual particle diameters (d_p), the electrical mobility (Z) and the molecular mass (M) in the hypothesis of particle density equal to 1.2 g/cm^3.

The current signal is characterized by three modes: the sub-nanometer at 0.85 nm and the two modes at ~2 nm and at ~7nm previously commented. At a first sight, one would attribute the origin of the sub-nanometer peak to carbon compounds produced in combustion, since the size distributions was obtained when analyzing the aerosol sampled from a rich premixed flame. However it is important to remind that the largest fraction of the aerosol entering the DMA was made by high purity particle-free nitrogen, working as cooling and diluting flow. Thus to test the nature of the sub-nanometer peak, the current signals of high purity particle-free gases were also recorded by the tapcon EMS. The specifications for the gases tested are reported in Table 2.3 and refer to a specific period of year 2006. Information was provided by Società Ossigeno Napoli (S.O.N.).

Figure 2.9 displays the current signals measured by the electrometer when testing the high purity particle-free gases (specified in Table 2.3) and the laboratory air in the early morning at an ambient temperature of 25°C. These signals refer to a single day of measurements with the corresponding available tank of that day. Small differences in terms of peak maximum value and presence of a small shoulder at about 1.2nm were observed analyzing different tanks or the same tank in different days. In any case no signal at 2nm or larger size was recorded.

[5] amu = atomic mass unit

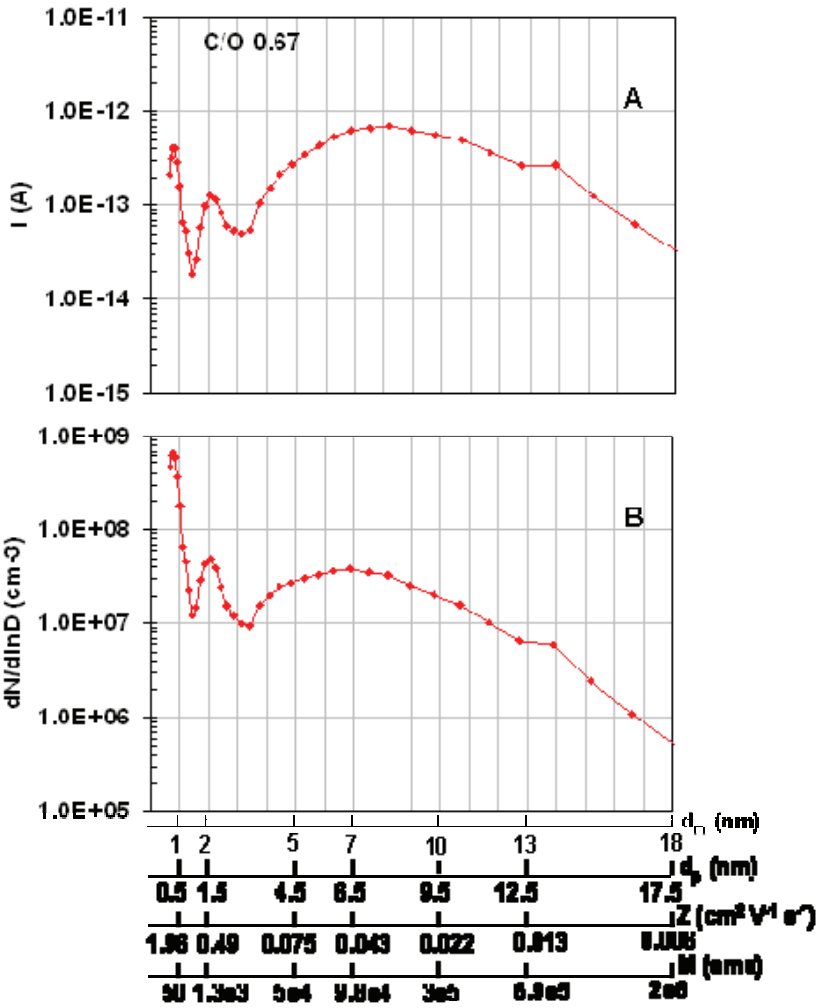

Figure 2.8 – Current signal measured by the electrometer (Panel A) and particle size distribution (Panel B) from a C/O = 0.67 premixed ethylene-air flame at H = 13 above the burner surface. The x-axis is extended to the lowest detectable signal (~0.65 for d_m) and is arbitrarily modified to include actual particle diameter (d_p), the electrical mobility (Z), and the molecular mass (M) besides the mobility diameter (d_m).

The sub-nanometer peak at ~ 0.85 nm was instead clearly visible in all the cases investigated. Its nature was mainly related to the charging mechanism of the bipolar charger (Sgro *et al.*, 2007a). The latter emits alpha particles that ionize gas molecules, producing an amount of ion pairs that brings all nanoparticles within a certain concentration to a steady-

state charge distribution, which is well predicted by Boltzmann statistics for particles larger than 20 nm, but better modeled with Fuchs' charging theory for smaller nanoparticles. The total amount and the shape of the mode (in some cases a shoulder at 1.2 nm was also measured) in the size range below 1.4 nm depended on the particle concentration in the measured aerosol and on the impurities present in the particle-free gas flow. As a consequence, the concentration of these 'charger ions' was highest in particle-free gasses and usually reduced as the concentration of particles in the measured aerosol increases (e.g. flames at the onset of soot formation) (Sgro *et al*., 2007b].

Table 2.3 – **Specifications of the tested gases**

Gas	Title	Impurity	Concentration
Nitrogen IP 4.8	≥ 99.998 % v/v	-Water -Oxygen -Total HC	3 ppm v/v 3 ppm v/v ≤ 0.1 ppm v/v
Carbon Dioxide P	≥ 99.999 % v/v	-Water -Carbon Monoxide -Sulfur	15 ppm v/v ≤ 5 ppm v/v ≤ 1 ppm v/v
Air Lab P	Oxygen 20.4÷21.4%	-Carbon Dioxide -Hydrocarbons -Water	1 ppm v/v 1 ppm v/v 3 ppm v/v
Oxygen 2.7	≥ 99.7 v/v	-Water -Carbon Dioxide -Methane	≤ 10 ppm v/v ≤ 2 ppm v/v ≤ 20 ppm v/v

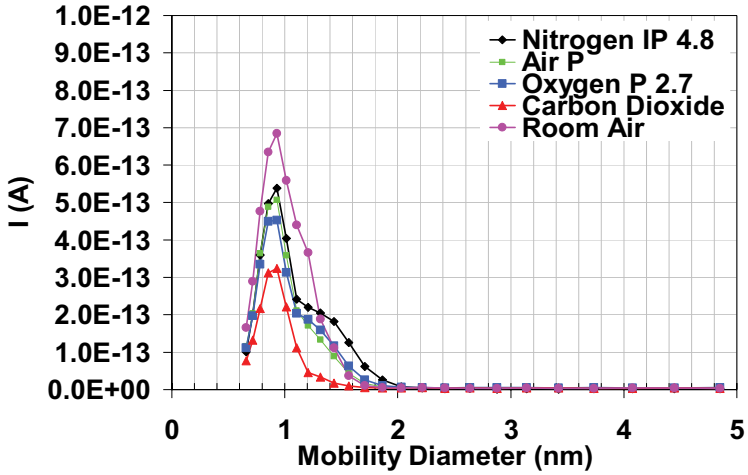

Figure 2.9 - Current signals measured by the electrometer from high purity particle free gases from tanks: nitrogen (black symbols), air lab (green symbols), oxygen (blue symbols), carbon dioxide (red symbols).

To add more information on the nature of this sub-nanometer peak, an investigation on the particle-free nitrogen was made. The measured signals were representative of a par-

ticular condition of the nitrogen tested were a shoulder at 1.2 nm also appeared (Figure 2.10). Without the bipolar diffusion charger, the current signal drastically decreased close to the current detection limit of the electrometer. This was a clear indication that this sub-nanometer peak consisted primarily of 'charger ions' produced by ion-induced molecular clustering. As displayed in Figure 2.8, these charged molecular clusters span the mass molecular range of 10-1000 amu. The majority of these clusters are not primary ions formed as the α-particles ionize the aerosol (free electron and positive ions with masses depending on the specific gas).

Obviously, in combustion processes, where carbon compounds are also present in this size range (Homann & Wagner, 1967; Apicella *et al.*, 2007), it becomes difficult to separate the species that contribute to this sub-nanometer peak. To discern the size distribution of flame products smaller than 1.4 nm, this sub-nanometer charger peak is a sort of 'instrument background' that needs to be removed. However, it cannot simply be subtracted since the ion-pairs created by radioactivity in the particle charger are either consumed by particles or participate in ion-induced clustering to form these 'charger ions' (or are lost to the walls).

Therefore this sub-nanometer peak, different from the other measured larger peaks in on-line tapcon EMS DMA measurements, is not discussed further in this thesis (except where explicitly said) and the measured size distribution are displayed starting from the lower measured mobility diameter of 1.4 nm.

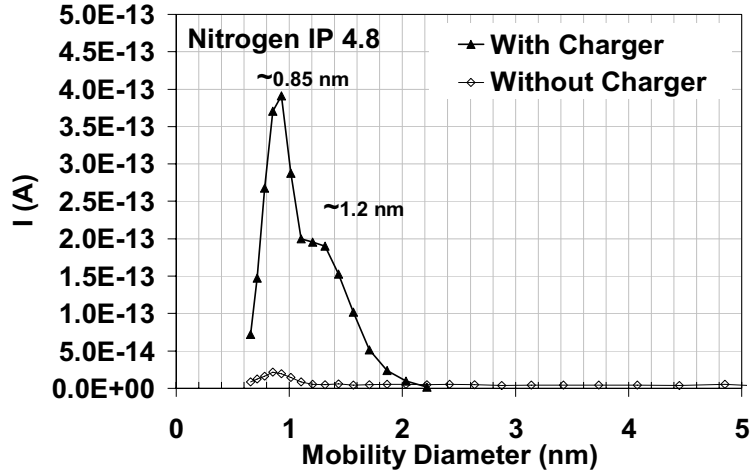

Figure 2.10 - Current signals measured by the electrometer from high purity particle free nitrogen with the charger (black full symbols) and without the charger (black empty symbols).

Third Chapter

Experimental apparatus: sampling devices

3.1 Sampling devices: probes and ejectors

The possibility of determining the size distribution of nanoparticles resolved in space and time at the exhaust of a generic combustion source via a differential mobility analyzer deeply depends on the appropriate sampling devices employed and on the line to transport the sampled aerosol from the source to the analyzer. Potential problems range from particle losses in the sample probe through particle-particle coagulation to diffusive wall losses along the sampling line. Furthermore, in flame's studies, the presence of a solid tube changes the flame temperature profile, the flow field and the concentration profiles, with a disturbance drastically dependent on the distance between the burner surface and the probe (Hartlieb *et al*., 2000; Zhao *et al*., 2003). Materials, dilution, geometry, position with respect to the aerosol source are some of the parameters that have been modified over the years to optimize the probe sampling technique (Burtsher *et al*., 1993; Hepp *et al*., 1995; Kasper *et al.*, 1997; Zhao *et al.*, 2003, Maricq *et al*., 2003)

Table 3.1 – **Summary of the sampling devices**

Probe	Material	Main Characteristic	Combostion source	Position	Laboratory/[1]
HP NA1	Stainless Steel	ID=8mm Wall thickness=0.5mm Orifice diameter=0.3mm	Premixed Flames	Horizontally positioned	DIC Napoli
HP NA2	Stainless Steel	ID=8mm Wall thickness=0.5mm Orifice diameter=0.7mm	Premixed Flames	Horizontally positioned	DIC Napoli
HP BE1	Stainless Steel	ID=7.5mm Wall thickness=1mm Orifice diame-ter=0.37mm	Premixed Flames	Horizontally positioned	CDB Berkeley
EP NA1	Stainless Steel	ID=3mm Length=20 cm	Premixed Flames/Domestic gas burner	Horizontally & vertically positioned	DIC Napoli
Dekati	AISI 316	Total Length=360mm Orifice diameter=8mm	LD diesel vehi-cles/Engine	Exhaust line	VERL & IM CNR

[1] DIC = Dipartimento di Ingegneria Chimica dell'Università "Federico II" di Napoli; CDB = Chemical Dynamics Beamline at Lawrence Berkeley National Laboratory in Berkeley (California); VERL= Vehicle Emission Research Laboratory at Ford Research and Innovation Center in Dearborn (Michigan); IM CNR= Istituto Motori del Consiglio Nazionale delle Ricerche in Napoli.

Table 3.1 summarizes the main specifications of the different sampling probes employed in this thesis. The home-made probes, labeled as HP (Horizontal Probe), were primarily used to explore the flame-generated nanoparticles whereas the ejector type diluter EP (Ejector Probe) was alternatively used to sample particles from flames and domestic burners at lower dilution and, finally, a commercial Dekati diluter was employed in the motor vehicles/engines tests. The following of this chapter furnishes a more detailed analysis of the probe employed and its influence on the measured particle size distributions.

3.2 Horizontal probe

3.2.1 Brief overview

Ideally, to study the flame-generated particles as they exist and evolve unperturbed in the flame, it is necessary to use a sample device able to immediate dilute, quench and transport the sampled aerosol to the analyzer in a way that preserve the salient features of the nanoparticles, thus effectively and systematically eliminating particle-particle coagulation processes, diffusive wall losses, thermophoresis and condensation.. Such a system does not yet exist but, over the years, very efficient sampling devices have been designed and experimentally tested to reduce and minimize sampling artifacts.

In 1997, Kasper *et al*. developed an *in situ* sampling probe for flames, made of a straight stainless tube with a small orifice for sample intake. The probe was placed horizontally above the burner and the flame gas sample was rapidly diluted by nitrogen gas in the probe, with the main purposes to quench chemical reaction, prevent the particles from coagulating or growing through condensation, and therefore avoid alteration of particle size distribution during the sampling process (Figure 3.1). Compared to the quartz microprobes used in the past, the advantage of this probe was the possibility to sample for enough time without suffering too much from the soot clogging of the orifice. In 2003 two independent studies by Maricq e*t al*. and Zhao *et al.* furnished further experimental information to characterize a sample probe similar to that of Kasper *et al.* (1997).

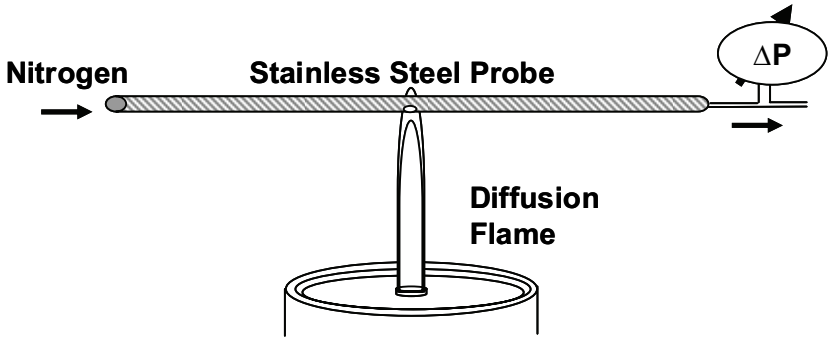

Figure 3.1 – Sampling device for a diffusion flame, adapted from Kasper et al. (1997)

In this thesis, the horizontal probes, HP NA1, HP NA2, HP BE1, were designed following the above said scientific works. Modification of probe thickness and orifice diameter allowed the possibility to use these probes for different purposes. The wall thickness of the HP NA1 probe near the pinhole, where flame samples enter and mix with a large N2 dilution flow, was reduced to 0.5 mm. The pinhole (diameter=0.3mm) was positioned along the centreline of the flame, facing downward toward the burner surface. The pinhole size yielded large dilution ratios (DR > 10^4), immediately after the flame sample enters the probe, high enough to prevent particle-particle coagulation and study flame-generated particles as they exist in the flame (De Filippo *et al.*, 2006; Sgro *et al*., 2007a). They were carefully adjusted by monitoring the under pressure in the probe with water manometer. Immediate and high dilution was crucial to minimize particle-particle coagulation in the sampling line. The sample gasses were cooled upon mixing with the cold gas nitrogen, controlled with a critical orifice and set at ~ 29.6 L/min. A downstream water cooled heat exchanger furnished further cooling and prevent the ionizer by excess heating. The distance from the probe orifice to the DMA inlet was 85 cm (sample residence time in the probe = ~88 ms). The distance from the burner surface to the fixed sampling probe (height above the burner surface, H) was varied with an accuracy of 0.01 mm using a vertical translation stage equipped with a micrometer.

The HP NA2 probe was inserted in the same sampling line of the previous described HP NA1. The difference is the orifice (diameter=0.7mm) drilled into the probe surface, which consented to obtain slightly lower dilution ratios (~10^3) in order to deliberately examine particle-particle coagulation (Lanzuolo *et al*., 2008).

The geometry of HP BE1 probe was slightly different from the other two probes in order to study the emissions from slightly richer (and sooting) flames.

3.2.2 Effect on the flame temperature

Probe sampling is indeed invasive and perturbs the flame temperature profile (McEnally *et al.*, 2006) and affects the experiment by cooling the post-flame products as they approach the probe. The probe's influence on the temperature of laminar premixed ethylene-air flame was studied employing the probe HP NA1, cooled by a constant flow of nitrogen set at 29.6 L/min. Flame temperature was measured with a thermocouple (type R, joint diameter = 330 μm, wires covered with Al_2O_3 insulators to minimize surface effects). Radiation corrections were applied to the measured temperature following the procedure described by Shaddix (1999).

Figure 3.2 shows the effect of the probe on the centreline temperature of a C/O=0.65 flame (unburned gas velocity = 10 cm/sec), comparing the measured temperature in the pre-flame, flame and post-flame zones without and with the probe positioned at different heights above the burner surface, H 8, 10, 12, 15 mm, indicated with dotted lines in the figure. Without the probe (empty symbols), the temperature first rises to flame temperature (around 1750 K at H=2mm) and then slightly decreases in the post-flame region (to 1650 K at H 15 mm) as a function of increasing H. The presence of the probe (black filled symbols) does not influence the flame temperature (maximum temperature measured along the centreline) but it does significantly lower the local flame temperature within about 0.4 cm ahead of the probe (~ 500 K). The shape of these temperature profiles are similar to

those reported by Zhao et al. (2003) for a slightly different premixed flame. In addition, extrapolating the measured data, the temperature of the sampled flame products in proximity of the orifice may be considered ~1000 K. As a consequence of these results, even though experimentally possible, flame-generated species were not collected with the probe horizontally positioned below H=7mm in order to avoid probe disturbance on the pre-flame and flame zone. To note that problems related to probe perturbation are commonly solved by shifting measurements made by the probe a few mm closer to the burner surface when comparing numerical and measured profiles even though there is no theoretical basis for this shifting (McNeally *et al*., 2006).

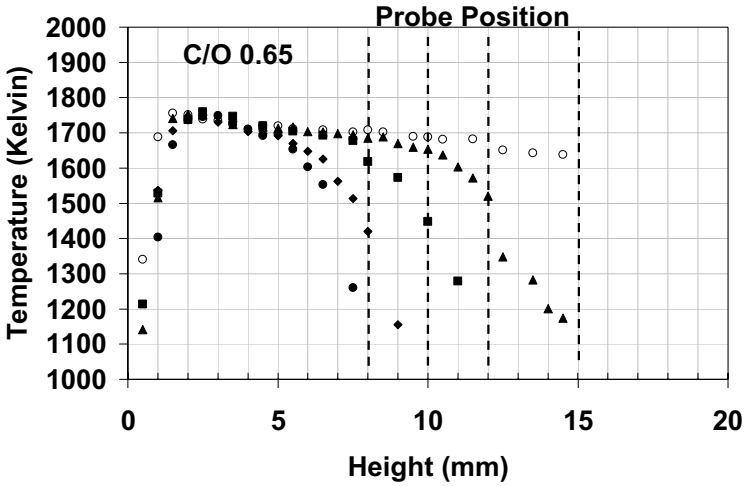

Figure 3.2 – Flame temperature profiles measured along the centerline of the burner with (filled symbols) and without the probe (empty circles), horizontally positioned at different height above the burner surface. Filled symbols: flame temperature profiles when the probe is fixed at H=8mm (black filled symbols), H=10mm (black filled diamonds), H=12mm (black filled squares) and H=15mm (black filled triangles).

Figure 3.3 shows the gas temperature profile measured with a thermocouple type K along the centreline of the dilution and sample flow when the probe was positioned at H 12mm above the burner surface and the dilution ratio at ~ 10^4. The temperature was measured at different distances from the sampling orifice (indicated with point 0 on the x-axis) to the inlet of the analyzer.

The average temperature of the diluted sample flow is ~320 K from the probe orifice to 85cm downstream (inlet of the analyzer), with a maximum of ~ 350 K at 16 cm downstream from the orifice. The high dilution employed and the relative low temperatures seem to be sufficient to quench chemical reactions.

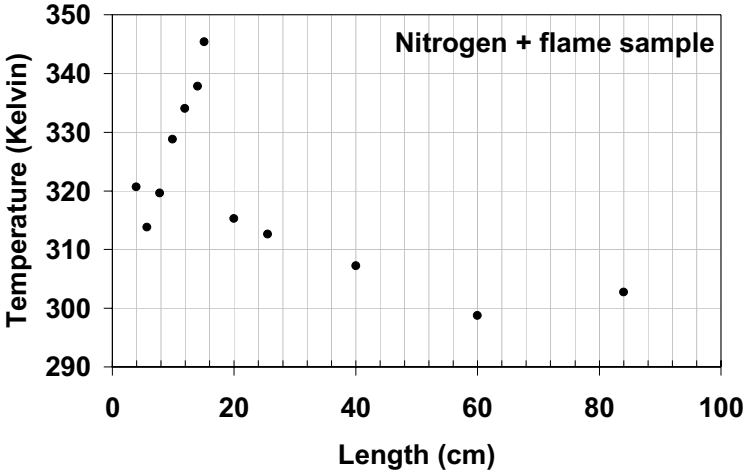

Figure 3.3 - Centerline temperature profiles inside the sampling line.

3.2.3 Effect of dilution on the measured size distributions

Dilution is a crucial point in probe sampling techniques. As the particles travel through the orifice before mixing with the diluting flow and during dilution as they travel through the probe, they may experience changes in their size distribution caused by particle-particle coagulation. The latter distorts the measured particle size distribution by reducing the concentration of small particles and increasing the concentration of large particles with respect to the actual distribution in the flame. On the basis of previous works, it is necessary to have high and immediate dilution and to measure the particle size distributions at a critical dilution ratio, defined as the level above which the shape of the size distribution becomes independent of the dilution ratio (Zhao *et al*., 2003). The dilution ratio is defined as the ratio of the diluting flow and the sampled flow. CO_2 measurements from a stoichiometric flame (C/O=0.33) with a non-dispersive infrared analyzer (Hartmann & Braun URAS 10E for HP NA1/2 probes; EGM-4 Environmental Gas Monitor PP Systems for HP BE1 probe) give information on the dilution ratio achieved at a fixed diluting flow and different under pressures at the probe pinhole.

At a constant diluting flow, the dilution ratio can be changed modifying the amount of sampled gas from the flame. Tests to determine the optimal operative dilution range to transport flame aerosol from the sampling point to the DMA, preserving the size distribution as in the flame, were made on premixed ethylene-air flames in the 0.6-0.7 C/O range. Both the tapcon EMS and TSI SMPS were used to measure the particle size distribution. As an example, just one set of measurements with the tapcon EMS is displayed (Figure 3.4). Particle size distributions were measured from a laminar premixed ethylene-air flame (C/O=0.67, unburned gas velocity=10 cm/s) at different dilution ratios with the probe HP NA1 fixed at H=10mm above the burner. The data were corrected for the dilution em-

ployed and for particle diffusive losses. The overall overlapping of the size distribution at a DR≈ $3*10^4$ (red symbols in Figure 3.4) indicates that this is the optimal range to measure the actual in-flame particle size distribution. In fact, when no correction for the dilution is applied, the shapes of the size distributions are not affected by the dilution and only the number concentration is changing. On the other hand, the process of coagulation appears more distinctly when sampling at lower dilution ratios (green squares) which causes a reduction of smaller particles and a broadening of the size distribution. At the same time it is possible to observe that at higher dilution ratios the corrected size distribution (purple symbols) does not overlap with the other at DR≈ $3*10^4$. Assuming that all the corrections are true, this result suggest that at these conditions the sampling flow is too low to establish complete mixing with the much higher turbulent flow.

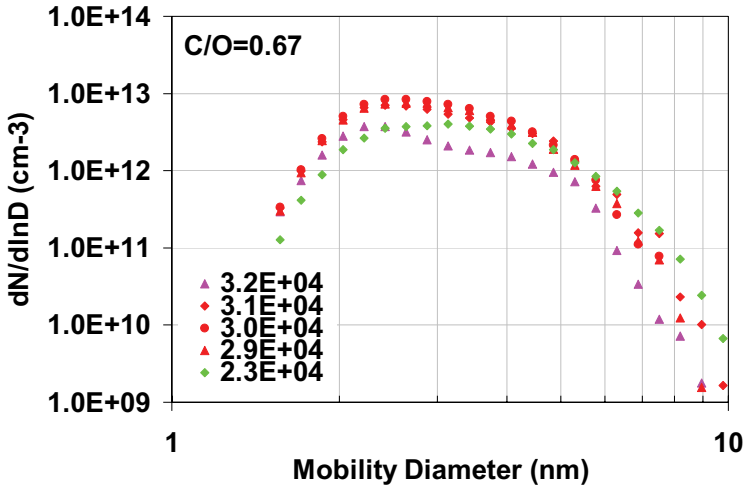

Figure 3.4 – Particle size distributions at different dilution ratios.

In Figure 3.5 (linear scale) the particle volume fraction is plotted versus the employed dilution ratios. The volume fraction is calculated from the size distributions presented in Figure 3.4 under the assumption of a constant density and a spherical geometry for the classified particle whose real diameter is calculated from the measured mobility diameter considering an effective diameter (do=0.5nm for air) for the particle–free sheath or carrier gas in the electrostatic classifier (Fernandez de La Mora et al., 2003).

The vertical dotted lines emphasize the presence of the three different dilution regimes already pointed out describing the measured size distributions. Regime I at lower dilution ratios is characterized by particle-particle coagulation. Thus the total volume fraction does not change within the experimental error, but the shape of the size distribution changes as previously described (Figure 3.4). Regime II represents the optimal operative dilution range to transport flame aerosol from the flame to the DMA without changing the size distribution. Regime III at larger dilution ratios is characterized by a non perfect mixing among flame aerosols and diluting gas. The optimal operative dilution range might change

depending on some features of the flame sampled particles, e.g. concentration and size, and therefore it is necessary to repeat this investigation when studying new flames.

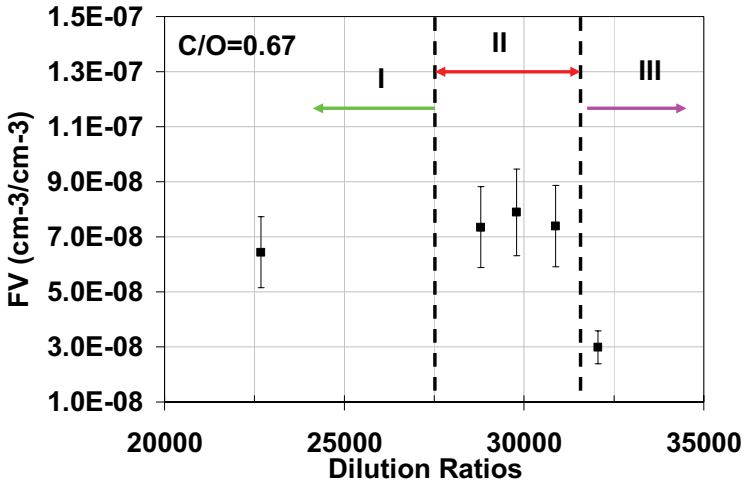

Figure 3.5 – Integrated volume fraction at different dilution ratios for C/O=0.67 at H=10mm. Error bars (20%) indicate the repeatability on the measured values.

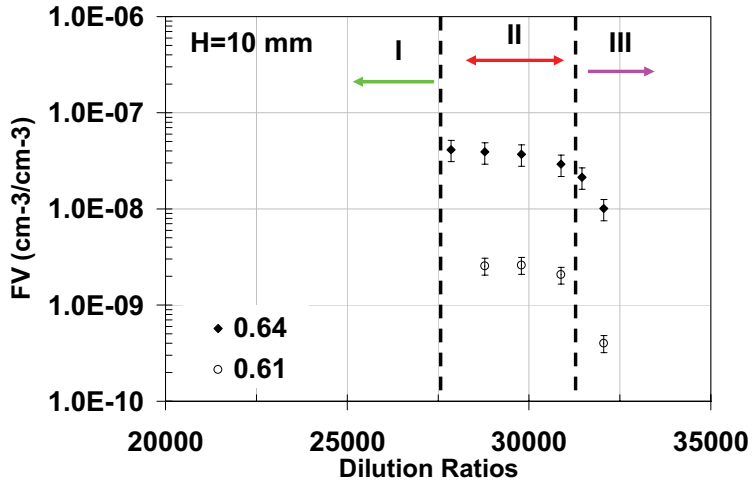

Figure 3.6 - Integrated volume fraction at different dilution ratios for C/O=0.64 (black diamonds) and C/O=0.61 (empty circles) with the sampling point at H=10 mm.

As previously addressed, an analogous investigation has been made for flames at different C/O ratios. Figure 3.6 reports the integrated volume fraction relative to two other ethylene-air flames (C/O=0.64, filled diamonds, and C/O=0.61, empty symbols) and again

the three different regimes of dilution. In this case the y-axis is logarithmic in order to include both sets of data.

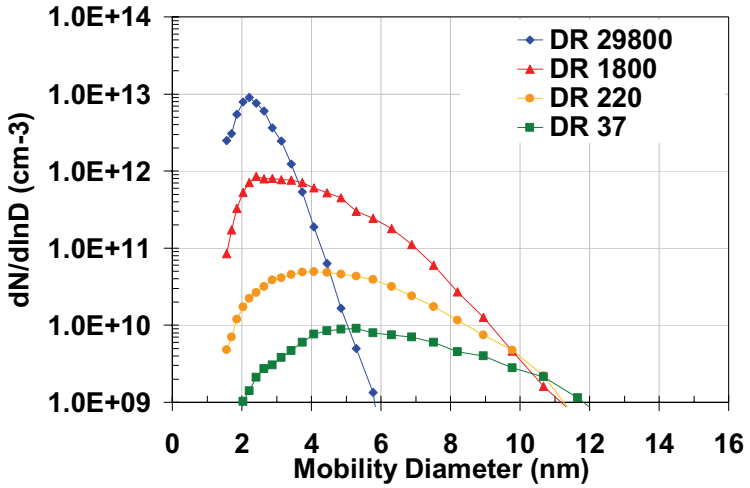

Figure 3.7 - Size distributions at different dilution ratios achieved employing probe HP NA1 (blue diamonds), HP NA2 (red triangles), a series of two ejectors EP NA1 (gold circles) and one ejector EP NA1 (green squares).

The range of dilution reported in the previous figures is quite small. This is a consequence of the specific probe employed (HP NA1) and the small vacuum at the pinhole (few mmH_2O), and the necessity to operate in conditions necessary to preserve the particle size distributions as in the flame. However, in order to achieve smaller dilution ratios, different sampling devices were also employed. Figure 3.7 reports the size distributions of nanoparticles emitted from the same ethylene-air flame at a fixed height above the burner in correspondence of four different dilution ratios. The highest dilution ratio (~$3*10^4$, blue symbols) was obtained employing HP NA1, in the sampling conditions already described for Figure 3.4. The red symbols in Figure 3.7 (DR~$2*10^3$) refer to the nanoparticles measured with HP NA2, which was operated exactly in the same conditions of HP NA1. Reminding the table 3.1, the difference between the two probes (both used with a slightly turbulent diluting flow) was simply due to the larger diameter of the orifice (and also the thickness) for the HP NA2 which, for the same underpressure, produces a higher amount of flame products to enter the probe. Therefore, with HP NA2, it was not possible to quench completely the interactions between flame-generated products and, in particular, coagulation was not suppressed. The lowest dilution ratios were instead achieved utilizing a different sampling dilution system. A single ejector probe placed horizontally above the burner surface sucked in flame-generated products by the underpressure created in the accelerated low pressure section of a Venturi tube operating at atmospheric pressure using particle-free N2 as the diluting flow through the Venturi. A wide range of dilution ratios could be achieved by adding additional ejector pumps (or Venturi tubes). In this investigation, a two stage (DR=37, green symbols) and a three stage ejectors system (DR=220, gold symbols) were employed.

Plotting the total volume fraction measured as a function of DR for these two dilution systems, it is possible to observe that the ejector pump dilution system measures less overall particles than the turbulent flow straight tube dilution probe (Figure 3.8). This may be due to thermophoretic losses (not taken into account) in the inlet prior to dilution, which is the thickness of the tube (0.5 mm) for the turbulent flow straight tube dilution probe, and several centimeters (~20 cm) for the ejector pump dilution system. Also, several ejector pumps in series cause complex flow patterns, which may increase particle losses beyond the simple corrections for diffusional losses in a straight tube.

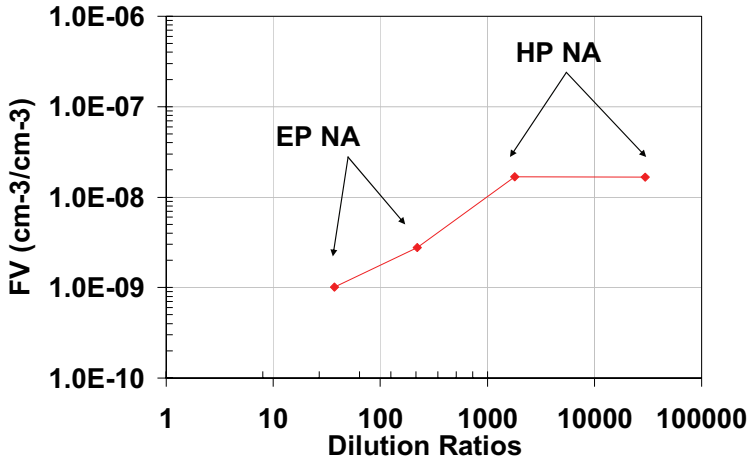

Figure 3.8 - Integrated volume fraction at different dilution ratios, employing two different sampling systems.

3.2.4 Pinhole clogging: effect of particle deposition in time

Another problem related to probe sampling in flame is the deposition of soot particles on the walls of the sampling orifice which, for the time required by the analyzer to complete the data collection, can distort the particle size distributions as in the flame. In fact the carbon deposition on the wall produces a change of probe orifice diameter, thus the dilution ratio, and a good procedure is to routinely clean the orifice with a thinner wire.

Figure 3.9 displays the measured size distributions from three different rich premixed ethylene-.air flames, with unburned gas velocity set at 10 cm/s, and the probe horizontally positioned at H=9mm above the burner. The size distributions were collected in continuum without cleaning the orifice, in high dilution conditions (~10^4). Time zero refers to the beginning of the first measurement (red symbols). Panel A and Panel B show that a continuum sampling did not produced significant change in the measured size distributions, which is likely indicative of low deposition rates on the walls and high reliability in time.

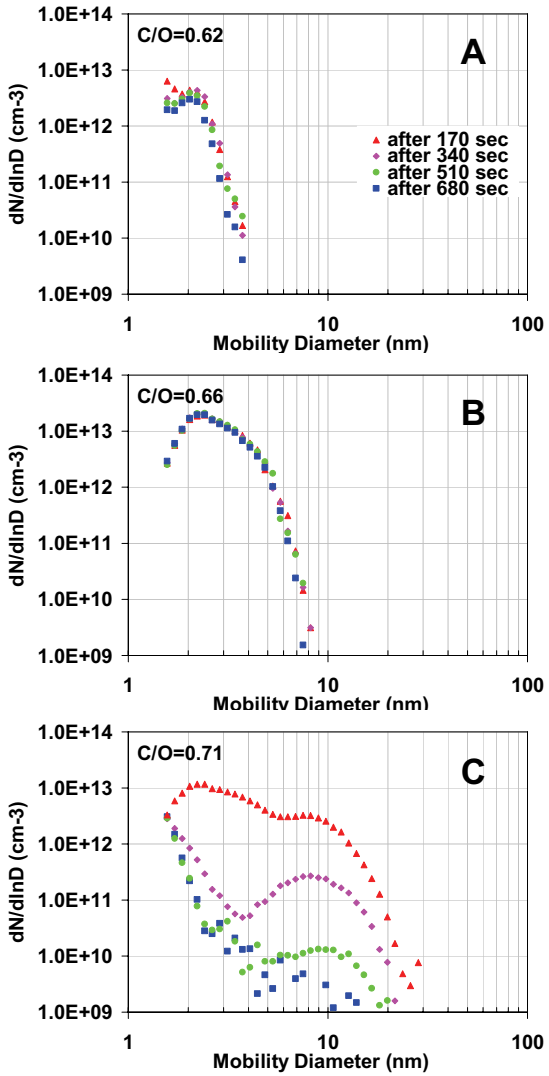

Figure 3-9 – Size distributions collected in continuum (without cleaning the orifice) from three different flames: a blue flame (C/O=0.62, Panel A), a blue flame with slightly yellow luminosity (C/O=0.66, Panel B), and a yellow flame (C/O=0.71, Panel C).

Instead Panel C, which refers to a yellow luminosity flame, clearly shows that there was an immediate effect on the size distribution between the first (after 170 sec) and the second (after 340 sec) measurements, indicating that with these flames it is necessary to clean the orifice before each scans. In the latter, to note that the smaller mode (~ 2-3nm) was particularly affected by the presence of the larger soot mode, thus probably working as

a filter for the smaller particles. After about 10 minutes the overall signal is close to the noise level indicating a complete obstruction of the orifice, clearly visible under the microscope. Measurements setting shorter scan times (not displayed) also indicate that with these sooting flames the carbon deposition starts in less than a minute and can even affect the first measurements (170 s for the tapcon EMS and 75 s for the TSI SMPS).

3.3 Home-made ejectors and the Dekati diluter

As already anticipated in the previous section, the other sampling device usually adopted for flame studies consists of a multi-stage ejector pump diluter, which has been demonstrated to sample with a similar efficiency to the horizontal probe if the dilution is sufficiently high and immediate (Maricq, 2004). However, employing sequential or multi stage dilution of the aerosol sample might make difficult to quantify particle losses (see Figure 3.8). The home-ejectors employed in this thesis were used to study the flame-generated material to keep the dilution at very low values.

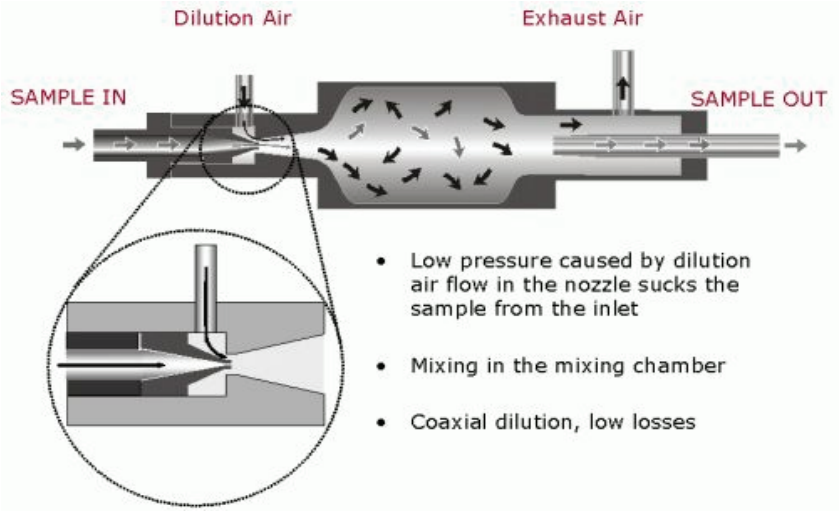

Figure 3.10 – Operating principle of Dekati Diluter, adapted from Dekati Ltd.

The operation principle of the ejector probes is the same of the commercial Dekati Diluter (Figure 3.10) which is commonly used in a two stage apparatus (the first heated) at the exhaust of test motor vehicles or engines. Referring to the Dekati Diluter, clean and dry pressurized dilution air (or nitrogen) is conducted to the diluter through an ejector cavity. The sample line is connected to the ejector cavity via an ejector nozzle. The high flow rate of the dilution air in the ejector cavity induces a pressure drop in the ejector nozzle causing sample flow into the diluter (Bernoulli principle). The dilution air mixes with the sample air in the ejector cavity and further in the diffusion cavity resulting in a homogeneous dilu-

tion of gases and particles (Figure 3.10). The ratio of dilution air flow to the sample flow determines the dilution ratio of the diluter. The latter is a function of the inlet pressure of the diluter and therefore a good procedure is to calibrate the actual dilution ratio measuring CO_2 concentration and pressure and temperature at the inlet of the diluter.

3.4 Diffusion losses along the sampling line

Particles smaller than 20 nm are lost to the surfaces mainly by diffusion. Well-accepted equations exist to calculate these losses in laminar and turbulent flows in tubes (Hinds, 1999). These calculations assume that every collision of a particle with a surface results in a particle loss, which agrees with experimental observation for NaCl particles as small as 2nm at room temperature (Alonso *et al*., 1997a).

For laminar flows, the particle penetration, P, defined as the number concentration of particles exiting the tube length, L, can be calculated using the classical formulas given by Gormeley and Kennedy (1949), expressed as the sum of the first terms of a series:

$$P = 0.819\exp(-3.657\zeta) + 0.0975\exp(-22.3\zeta) + 0.0325\exp(-57\zeta) \quad \text{for } \zeta \geq 0.0312 \quad (3.1)$$

$$P = 1 - 2.56\zeta^{2/3} + 1.2\zeta + 0.177\zeta^{4/3} \quad \text{for } \zeta < 0.0312 \quad (3.2)$$

where $\zeta=\pi DL/Q$, D is the particle diffusion coefficient and Q the aerosol volumetric flow rate through the tube (Gormeley and Kennedy, 1949; Alonso *et al*., 1997a).

For turbulent flows, the particle penetration can be estimated by the following equation (Hinds, 1999):

$$P = \exp\left(\frac{-4V_{dep} \cdot L}{D_{in} \cdot U}\right) \quad (3.3)$$

where V_{dep} is the deposition velocity, Din the inner diameter of the tube and U is the average velocity of the aerosol.

Estimated particle losses with Equation (3.3) in the turbulent flow of the sample line after dilution can be considered negligible (Zhao *et al*., 2003) or insignificant compared to those in the orifice (Sgro *et al*., 2008b), where the flow is laminar and calculated with Equation (3.1) and (3.2).

However, the analysis of particle losses in the orifice requires further comments. The temperature of flame products entering the probe orifice was estimated as $T_{orifice} = 1000 \pm 250$K, where the large uncertainty depends on the fact that the temperature profile is steeper within 2mm ahead of the probe (see Figure 3.2). Then, the observation that flame generated particles smaller than 5 nm, at least at high temperature, adhere to surfaces less than larger particles even when they are in higher concentration at flame temperatures (Figure 3.6 A and B), suggests that while their mobility is higher, they may escape collisions with surfaces by thermal rebound (D'Alessio *et al*., 2005). Therefore, the effect of particle rebound has been taken into account considering that the number of collisions with the walls producing losses of particles is equal to the number of collision multiplied by the particle sticking efficiency, γ_{SD}, evaluated by the interaction potential of particle with orifice walls, similarly to the interaction with mica disk as discussed in D'Alessio *et al*. (2005) which depends on particle size, temperature and chemical composition. Figure 3.11

shows the estimated particle penetration in the orifice used to correct the size distributions measured by the DMA for particle losses. Assuming 1000 K as the temperature of the orifice, penetration was calculated in two ways: P1, assuming no thermal rebound (γ=1), and P2, accounting for a size-dependent sticking efficiency during particle-wall collisions (γ_{SD}). The minimum in the penetration curve calculated with γ_{SD} occurs because particle mobility (and so the number of collisions with the walls) increases while the sticking efficiency (or number of collisions that result in a loss of particles) decreases with decreasing particle size.

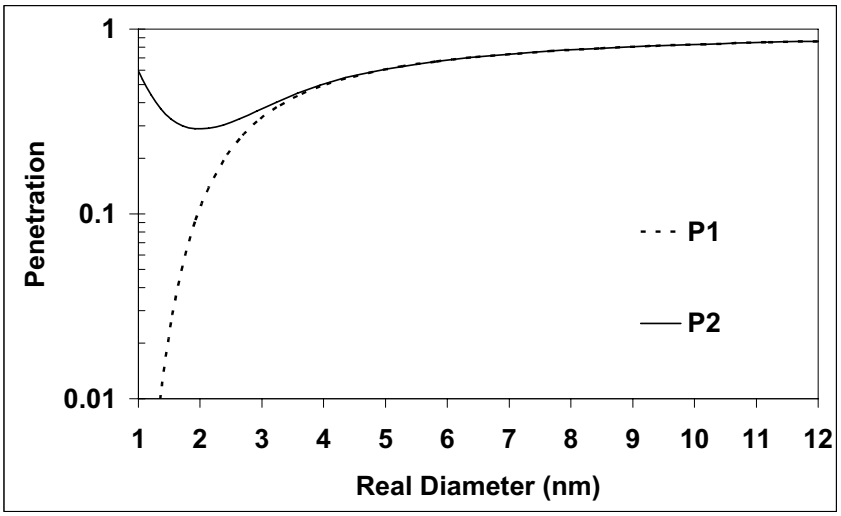

Figure 3.11 – Particle penetration inside the orifice calculated assuming no thermal rebound P1 (γ=1) and assuming a size dependent sticking efficiency P2 (γ_{SD}).

Particle losses were estimated ≈67% for 2nm particles and ≈41% for 5nm particles. X-axis refers to the real or actual particle diameter.

Indeed, the presence of particles rebound during penetration of nano-sized particles in laminar flow through tubes is still under debate (Alonso *et al*., 1997a; Wang and Kasper, 1991). In any case, in the size range below 3 nm, the size distributions corrected for losses assuming γ_{SD} will be only marginally different in shape from the uncorrected size distributions. In contrast, corrections assuming no thermal rebound (γ=1) would produce a dramatic change of the size distribution which would become a tail of a distribution that is below the lower size detection limit of the classifier.

Finally electrostatic losses were minimized by keeping all of the sampling lines in contact with particles conductive and at the same potential. Instead, due to the lack of knowledge about the thermal gradients across the probe orifice, it was difficult to quantify thermophoresis losses and they were not considered. However, since the thermal gradient between the probe wall and the sampled gas, at least at the orifice inlet, seems to be minimal, and, assuming that this remains constant as the nanoparticles travel

across the 0.5mm of the wall thickness, thermophoretic losses can be considered negligible.

Fourth Chapter

Experimental results: premixed laboratory flames

4.1 Introduction

Traditionally laboratory premixed one-dimensional flames involving small hydrocarbons such as methane, ethylene, and acetylene as the fuel represent simpler systems to study the chemical mechanisms of fuel decomposition and aromatics formation in flames. Despite their only apparent simplicity, studies on these flames still require continuous improvements and efforts to characterize the essential steps to soot formation such as the dynamics of very small incipient nanoparticles. In recent years, different flames studies have revealed some important properties of these nanoparticles formed in fuel rich flame burning but non-sooting conditions, typical of modern engines/burners that emit low to undetectable levels of soot. The mean particle diameter has been estimated about 2-3 nm (Minutolo *et al.*, 1999; Barone *et al*., 2003; Sgro *et al*., 2003; Sgro *et al.*, 2007a), they present an organic carbon structure, and therefore are referred as Nanoparticles of Organic Carbon (NOC), and they are transparent to the visible radiation (Minutolo *et al.*, 1999, 1994). In addition, they seem to experience a size-dependent coagulation rate at high temperature (D'Alessio *et al*., 2005) which implies that combustion-generated nanoparticles, particularly those smaller than 3-5 nm, may escape the exhaust systems without ultimately growing to larger sizes, especially when no adequate filter media and after-treatment devices are employed.

Currently among the experimental techniques that are used to study flames, the combined use of a sampling/diluting probe and a differential mobility analyzer (DMA) have received increased attention to characterize flame-generated particle size distributions in different burning conditions (Sgro *et al.*, 2007a; Thierley *et al.*, 2007; Zhao *et al*., 2003; Maricq *et al*., 2003). This chapter relies on the on-line measurements by DMA of flame-generated nanoparticle in different burning and sampling conditions. The size distributions were measured in a C/O interval extending from non-sooting to slightly sooting flames (C/O greater than about 0.70 for premixed ethylene air flames with cold gas velocity=10 cm/s) to evaluate their behavior at high temperature environment, and also to compare these results with those on analogous flames from previous studies employing UV-visible (D'Alessio *et al*., 1998; Minutolo *et al.*, 1994) and atomic force microscopy (AFM) (Barone *et al.*, 2003), transmission electron microscopy (TEM) (Dobbins & Subramaniasivam, 1994; Vander Wal, 1998), mass spectrometry (Homann & Wagner, 1967) and size exclusion chromatography (SEC) (Apicella *et al*., 2003).

4.2 Premixed ethylene-air flames from a McKenna burner

Premixed laboratory flames are usually generated through McKenna burners (Figure 4.1) which, in principle, are able to produce "flat" and highly stable flames. These characteristics are necessary in order to consider the flame to be one-dimensional. This type of burner is worldwide employed both for the development and calibration of optical diagnostic techniques (Clauss *et al*., 2000; Barlow & Carter, 1994; Cheskis, 1999), and as a calibration device for flame temperature diagnostics techniques (Prucker *et al*., 1994), and also for the study of gas species and nanoparticles responsible for soot formation by using several optical and sampling techniques (Gonzales Baquet *et al*., 2007; Thierley *et al*., 2007; Maricq *et al*., 2003; Apicella *et al*., 2007; Sgro *et al*., 2007a). Different models of this burner are commercially available, with either a stainless steel or bronze porous disk. Recently, Migliorini *et al.* (2008) have pointed out some differences in the measured soot distribution using the stainless steel versus the bronze porous disk in rich sooting flames with the same input stoichiometries, flow rates, and geometry. On the basis of line-scattering measurements at 647nm, the authors concluded that the bronze configuration seems to work properly and that the observed differences could be related to the different thermal conductibility of the burner material and the c
this thesis, water cooled sintered bronze McKe
lize rich premixed laminar flames (Panel B in Fi

A further device used to improve the stabil
plate, positioned at a certain height above the b
presence of the plate in the flame may also dist
approaches the plate surface, and this influenc
(2007) employing different configurations of t
was used as well (see Panel B in Figure 4.1),
horizontal probe (which already perturbs the fla
along the centreline above the burner surface a
perimentally verified that the presence of the p
bution.

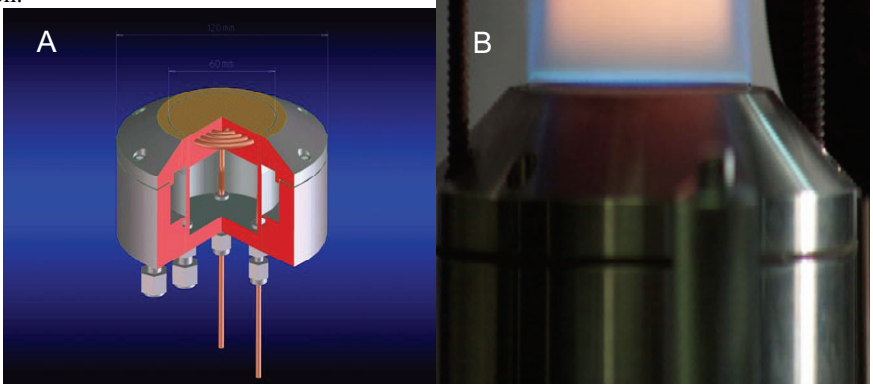

Figure 4.1 - Sectional view of a McKenna burner (A), adapted from Holthuis and example of a rich premixed flames generated from a water cooled sintered bronze McKenna burner(B).

4.3 Flame-generated nanoparticles at different C/O ratios

The majority of the work presented in this section is concentrated on flames that are below the onset of soot formation with ethylene and air supplied to the burner via Brooks mass flow controllers with an accuracy of ± 0.7% of each rate to obtain unburned gas velocity = 10 cm/s and C/O ranging between 0.61 and 0.69. The flame products were sampled at the centre of the burner with the horizontal probe HP-NA1, immediately diluted (~ $3*10^4$) to quench particle-particle coagulation and preserve the size distributions as in the flame, and transported, once mixed with a turbulent flow of room temperature nitrogen (Q_{N2}=29.6 L/min; Reynolds number, Re≈5000), to the tapcon EMS for the subsequent analysis. The distance from the sampling point to the inlet of the analyzer was 85 cm and the correspondent residence time was ~ 87 ms. The concentration of particles at the inlet of the sample orifice was calculated from the number concentration, dN/dln*D,* provided by the EMSSYS software, divided for the particle penetration along the entire sampling line (orifice + probe) and multiplied both for the applied dilution ratio and for the ratio of the temperature of the DMA, T_{DMA}=300K, and the temperature of the orifice, $T_{orifice}$=1000K, to account for the change in gas volume with temperature.

4.3.1 Size distributions

Figure 4.2 shows the size distribution of incipient nanoparticles produced in ethylene-air flames with a C/O ratio ranging from 0.61 to 0.69, just at the on-set of soot formation, i.e., which is here defined as the C/O value where light absorption in the visible and Laser Induced Incandescence (LII) are detected (D'Alessio *et al*., 2007). The particle size distributions were collected at a fixed height above the burner, H=10mm, and the majority of these investigated flames (C/O< 0.67) did not show noticeable signs of particle deposition into the orifice, even though high concentrations of particles were measured.

At different C/O ratios, a peak around 2nm was always present. This peak rapidly increased with increasing the fuel to oxidant content and its width broadened towards larger sizes for richer flames. When the yellow luminosity of the flame increased (C/O=0.69), a shoulder at about 3-5 nm started to grow out from the smaller mode while the number concentration of the 2nm peak remained unchanged.

Figure 4.3 displays the particle number concentration (blue solid line-solid-full symbols) and the volume fraction (red dotted line-empty symbols), respectively on the primary and secondary axis, calculated from the integration in the size range between the minimum (d_m=1.4 nm) and the maximum diameter measured for each case. The number concentration increased with the C/O ratio from C/O=0.6 to C/O=0.67 while it remained practically unchanged in the step from C/O=0.67 to C/O=0.69. Conversely, the volume fraction increased with a constant slope over the entire C/O range. The increase of volume fraction with C/O was consistent with previous measurements obtained with optical techniques on the same flames and the increase of gas phase particle precursors (D'Alessio *et al*., 2000; Violi *et al*., 1999).

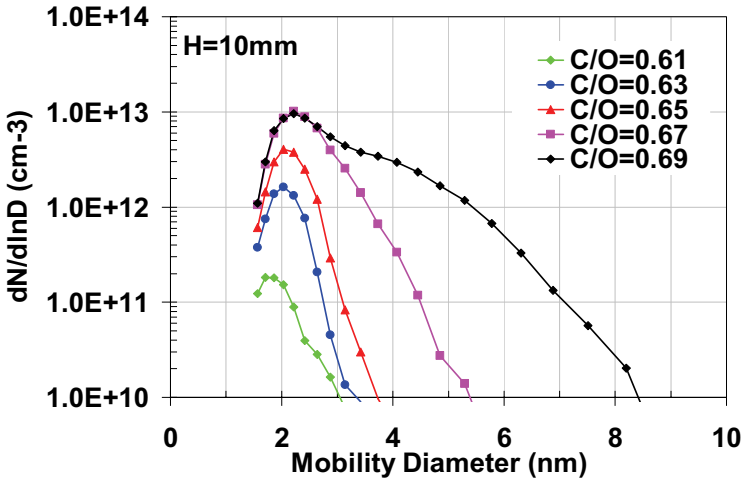

Figure 4.2 - Particle size distribution measured at H=10mm in ethylene-air flames with C/O=0.61 (green symbols), 0.63 (blue symbols), 0.65 (red symbols), 0.67 (purple symbols) and 0.69 (black symbols), adapted from Sgro et al. (2007a).

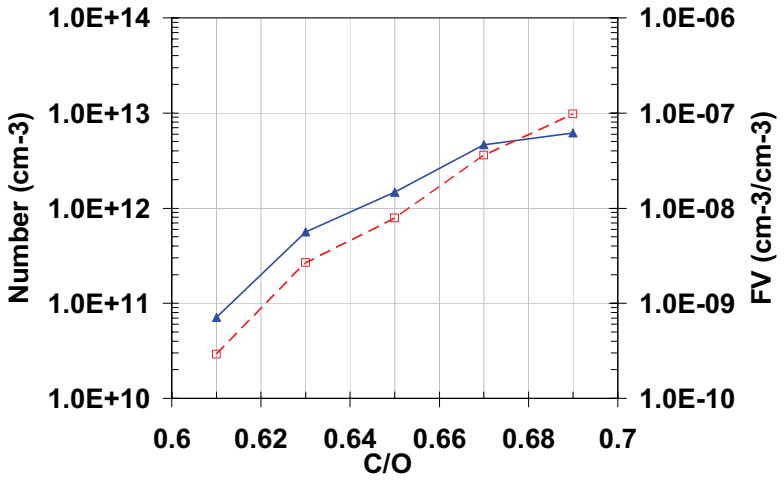

Figure 4.3 - Particle number concentration (blue solid line-filled symbols, primary axis) and volume fraction (red dotted line-empty symbols, secondary axis).

However, the slope of the increase for the DMA measurements reported in Figure 4.3 was larger than what was observed with *in situ* optical measurements and atomic force microscopy (AFM) analysis of particle collected by thermophoretic sampling and a good agreement was found only in flames above the soot formation threshold (Sgro *et al.*, 2008b) where particles larger than 3 nm were also detected. Furthermore, as Figure 4.2

shows, no particles were detected for C/O < 0.6 with the tapcon EMS while AFM and optical measurements detected a significant amount of particles in the C/O range from 0.5 to 0.6 (Minutolo *et al*., 1999; Barone *et al*., 2003; Sgro *et al*., 2008b).

The observed discrepancy, when only particles smaller than 3nm were detected with different diagnostic methods, might not be explained by the small size of the particles alone and by the corrections for particle losses in the probe (Sgro *et al.*, 2008b). Therefore, at present it is not possible to justify in a definitive way the disagreement in the current measurements, and further investigations are necessary in order to characterize chemically and physically this class of nanoparticles whose chemical composition (and size) possibly affects particles diffusivity, ionization efficiency, optical properties or interaction potential which could help to bridge the gap.

4.3.2 Particle charge

Figure 4.4 shows the current signals (Panel A) and the size distributions (Panel B) measured by the tapcon EMS from a rich premixed ethylene-air flames, at unburned gas velocity =10cm/s, with C/O =0.61 (green symbols). Reminding the general sketch of the experimental setup (see Figure 2.1), the signals were collected with the tapcon EMS in two different cases: with the Am-241 neutralizer before the electrostatic classifier (solid lines-full symbols) and without the bipolar charger (dotted lines-empty symbols). Since the tapcon EMS was operated with a positive center electrode voltage, only negatively charged particles were detected by the electrometer.

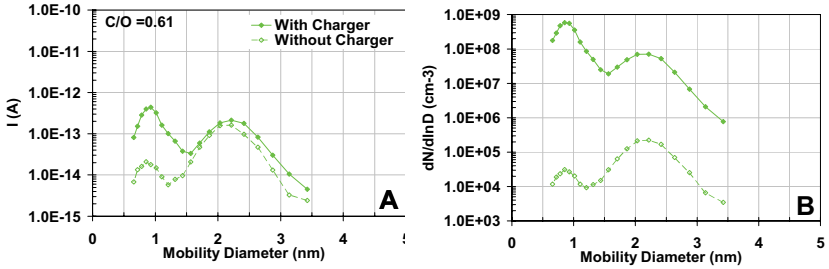

Figure 4.4 – Current signals (Panel A) and size distributions (Panel B) measured by the EMS from atmospheric premixed ethylene-air flame with C/O=0.61 with (solid lines-full symbols) and without the neutralizer (dotted lines-empty symbols). Height above the burner, H=10mm.

The size distributions displayed in Panel B are not corrected for dilution and diffusion losses along the sampling line. Moreover, when the Am-241 was present (full symbols), the size distribution was obtained from the current signal considering the values of charging probabilities provided by the software while, without the neutralizer, this correction was not made (the number of correction terms used for the data reduction was set equal to 0 in the EMSSYS software).

The x-axis is extended below 1.4 nm also to evaluate the behavior of the sub-nanometer peak in presence of flame-generated material. For the C/O=0.61 flame, where

only a particle mode at 2 nm is present, both the absolute value and the shape of the current signal were not affected by the removal of the bipolar charger. On the other hand, the peak at 0.85 nm considerably decreased as observed in a particle free-gas (see section 2.2.4). This behavior indicates first that the nature of the 2nm peak is completely different from that of the sub-nanometer peak. The 2nm peak is definitely flame-generated and is not a result of molecular clustering in the ionizer. Furthermore, clusters produced in the ionizer are entirely smaller than this peak and do not interfere. Therefore it is possible to state that the 2nm peak is quantitatively measured by this setup. This observation is not surprising because many other measurements based on other techniques (AFM, optical diagnostics, PIMS, FTRPA) (Barone *et al*., 2003; D'Alessio *et al*., 2005; Minutolo *et al*., 2007; Gonzales Baquet *et al*., 2007; Bruno *et al*., 2007) also found a ~2nm peak for flame-generated nanoparticles. However, the results in this thesis are the first evidence reported using only a DMA.

Furthermore, the 2nm flame-generated particles are naturally charged in the combustion process (see Figure 4.4). The observation that the amount of charging in the flame is quite similar to that in the charger is surprising. When the neutralizer is present, the steady state charge is achieved at room temperature. On the other hand, when the neutralizer is not present, the charging occurs presumably in the flame, at a temperature of about 1700 K. Therefore, since the temperature dependence is roughly exponential, these steady states should be quite different and the current measured in the absence of the neutralizer should be larger than with the neutralizer (as it was really found for higher C/O ratios). For the specific flame displayed in Figure 4.4, possible explanations are either: 1) that the flame contains enough ions to achieve a 'steady state' charge distributions similar to that predicted by Fuchs theory (Fuchs, 1963; Wiedensohler, 1988) or 2) the charge distribution achieved by the flame is not Fuchs' and the charger is unable to effectively fully charge the particles. The latter hypothesis could also explain the quantitative observed differences with optical techniques on the amounts of material at 2nm measured when investigating leaner flames (C/O < 0.65). Other specific experimental investigations on particle charging are required to provide a more definitive explanation for the measured currents.

In addition, Reischl *et al.* (1996) and Alonso *et al.* (1997b) have experimentally found that Fuchs' theory for bipolar charging can be used to predict the charging probabilities down to 2nm, respectively for WOx and NaCl nanoparticles. But nobody have experimentally found for flame-generated nanoparticles. In previous studies on the electrical charge of flame-generated nanoparticles (Maricq, 2008, 2006, 2005, 2004), Maricq (2007) found that larger particles (d >5nm) are charged to 'steady state' equilibrium, which is what it was found in this thesis if point 1) of previous paragraph is true while, on the contrary, the lower particle mode (d_m<5) was charge neutral in various burning and environmental conditions: different heights above the burner (2004, 2005), single DMA and Tandem DMA measurements (2005), different fuels (2006), and different times in residence tube (2008). At a first sight, the fact that the 2nm flame-generated particles, measured in this thesis, are naturally charged in the combustion process is in contrast with the electrical neutrality addressed by Maricq. However, this contrast is only apparent. More specifically, the argument given by Maricq is that particle charging by gaseous chemiions occurs relatively low in the flame. As these particles coagulate with increasing height in the flame, particles in the upper size mode remain charged. But new particles that are formed below 5nm, remains electrically neutral because there no longer remain any ions to charge them. Thus, an

important aspect of his argument is the contemporary presence of larger soot particles with the smaller particle mode. In this thesis, the measurements were performed at low height, for flame with a high gas flow and before the first larger size soot mode was formed. Therefore there were still ions in the flame to charge these nanoparticles. So the burning conditions for the C/O=0.61 flame were quite different from those generally investigated by Maricq and explains the discrepancy. To support this interpretation, it is worth nothing that, in some cases, e.g. Fig. 4 in Maricq (2005), Maricq also found that, early in the flame when the size distribution was monomodal and peaked at ~3nm (lower detection limit for his instruments), this particle mode was not uncharged and accounted for the ~0.1% of the particle population. This specific condition was similar to the C/O=0.61 case, both in terms of particle number concentration and mean diameter, and eventually a fairly good agreement (and not contrast) could be found also in terms of particle charge since, as Panel B shows, the charge accounted for 0.28% of the particle population in the size range 1.4 nm-3.42 nm.

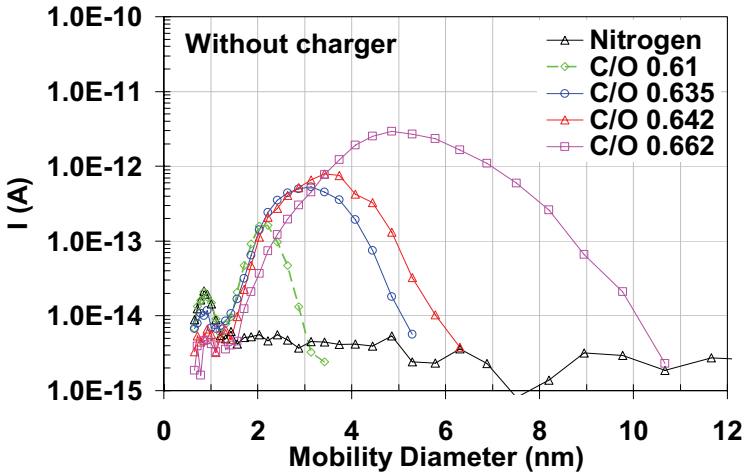

Figure 4.5 – Current signals measured from different premixed flames with C/O=0.61 (green diamonds), C/O=0.63 (blue circles), C/O=0.642 (red triangles) and C/O=0.66 (purple squares) without the neutralizer. Black symbols refer to that for the particle-free nitrogen. The probe was fixed at height, H=10mm, above the burner.

Figure 4.5 displays the current measured by the electrometer without the charger for different flames in the C/O range below the on-set of soot formation: 0.61 (green diamonds), 0.635 (blue circles), 0.642 (red triangles) and 0.662 (purple squares). Also the signal from free-particle nitrogen is displayed (black triangles). The sampling condition was exactly the same for all the flames studied. It is worth noting that with increasing the particle concentration in the flame there is a shift of current signal towards larger sizes, similarly to what observed in the size distributions, and a decrease of current signal related to the sub-nanometer peak, depending on the fact that the presence of large flame-generated particles subtract the ions necessary to produce molecular clustering.

At present, current signals at higher C/O ratios and burning conditions are not yet investigated and represent a future goal to complete the analysis of NOC particles with respect to larger soot particles. However two important results were achieved by these measurements. First, when only particles smaller than 3nm were detected, and in non-sooting burning conditions, the 2nm NOC particles were not charge neutral and were clearly distinct from the sub-nanometer peak. This is a strong indication that the 2nm particles are flame-generated and not a result of molecular clustering in the ionizer. Second, when particles larger than 3 nm were also detected, the charge distribution was shifted towards the larger sizes, in agreement with was found for particle size distribution. This is indicative that when larger particles are present, they subtract charge to the 2 nm particles which eventually become neutral. The role of charged particles in flame dynamics remains an interesting and important topic because it can influence particle processes, such as coagulation (Maricq, 2008), and might also be an explanation for the observed differences between nanoparticles of organic carbon (NOC) and larger soot particles.

4.4 Size distributions at different heights above the burner surface

This section describes the size distributions of flame generated nanoparticle formed in atmospheric pressure premixed ethylene-air flames as a function of the height above the burner surface, H. The first part of this section describes the measurements of a flame with C/O = 0.65 (cold gas velocity= 10 cm/s), considered to be below the soot-forming threshold since in situ optical measurements found no signs of soot (fluorescence and extinction in the visible, black body emissions, or incandescence) (De Filippo *et al*., 2007). DMA measurements were performed with the same experimental setup as described in section 4.3 and the data were corrected for particle diffusion losses and dilution ratio. The distance from the burner surface to the fixed sampling probe was varied with an accuracy of 0.01mm using a vertical translation stage equipped with a micrometer. The measured size distributions were used to deduce implications on particle formation processes and growth dynamics, including inception, surface growth and coagulation since the measured trends of volume fraction, f_v, number concentration, N, and size changes give information on the relative magnitude of particle growth processes.

In the second part of this section, these measured size distributions are compared to those predicted with a coagulation model to make more quantitative estimates on the relative roles of the particle growth processes. The model uses the coagulation efficiency, γ, to either consider no thermal rebound from particle-particle collisions (γ=1, and the coagulation rate is equal to the collision rate) or a size-dependent coagulation efficiency (γ_{SD}) where the coagulation rate decreases rapidly with decreasing diameter for particles smaller than 5 nm because their kinetic energy at high flame temperatures is higher than their interaction energy during collisions, following earlier work (D'Alessio *et al*., 2005). The detailed description of the model is reported in recent papers (Sgro *et al*., 2007a; Lanzuolo *et al*., 2008) and will be not discussed in this thesis.

Finally the last part of this section reports additional measurements of flame generated nanoparticle formed in two other atmospheric pressure premixed ethylene-air flames (leaner than C/O=0.65) as a function of the height above the burner surface, H.

4.4.1 C/O=0.65: experimental results

Figure 4.6 shows the size distributions measured from a C/O=0.65 flame at 12 heights in the range from 7 to 15 mm, which correspond to residence times from ~12 to ~27 ms. These size distributions were characterized by the presence of two particle modes below 10 nm. Early in the flame, below H=10mm, the size distribution was monomodal, with the modal diameter at ~2 nm. This mode shifted slightly toward larger sizes (from 2 to 2.4 nm) in about 5 ms when increasing the height from H=7mm to H=10mm. Similarly its number concentration only marginally increased (~ 1.3 times) in the same interval. At higher residence times, a second larger mode appeared, first as a shoulder growing out from the smaller mode (H=10.5 mm), and later as a well distinct mode (H=15mm). The modal diameter of this larger mode shifted from 3 to 4.5 nm in 7.5 ms, while its tail broadened from 6 to ~10 nm.

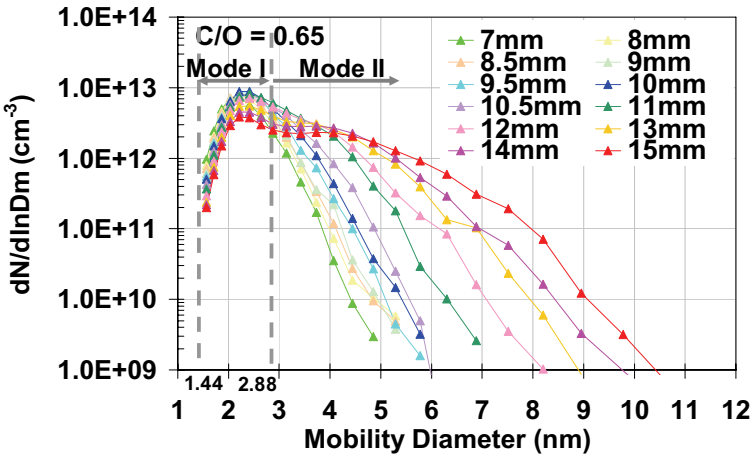

Figure 4.6 - Particle size distribution measured at different heights above the burner surface in an ethylene-air flames with C/O=0.65 and unburned gas velocity =10 cm/s.

Measured trends of volume fraction, FV, number concentration, N, and size changes give information on the relative magnitude of particle inception, coagulation and surface growth processes. Generally, an increase in total N can be due only to inception while a decrease in N is necessarily due to coagulation. An increase in FV could be due to either inception, which would preferentially increase FV at small sizes or surface growth. Since FV is proportional to d^3, surface growth has a much greater effect on FV than inception. The increase in particle size can be ascribed to coagulation and surface growth while significant inception would reduce the mean diameter.

Figure 4.7 shows the evolution of N (Panel A) and FV (Panel B) for the entire distribution, mode I and mode II as a function of H, furnishing more detailed information on

particle growth processes . The dotted vertical lines in Figure 4.6 delineate the size intervals considered for modes I and II.

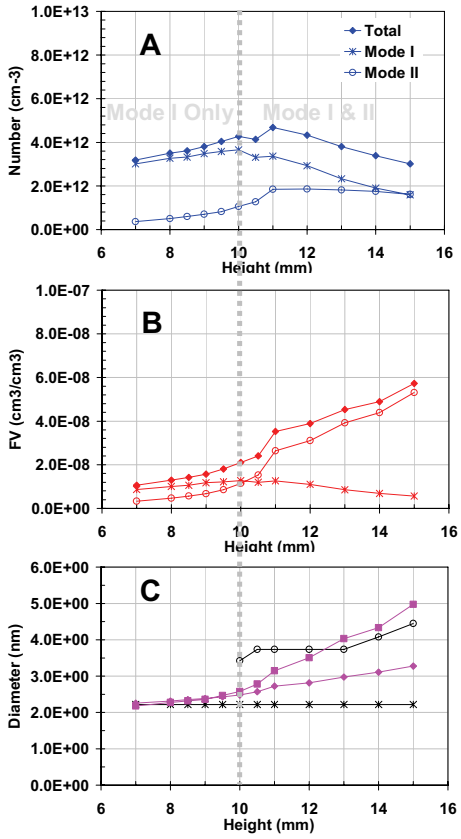

Figure 4.7 – Integrated values of number concentration (blue symbols, panel A), volume fraction (red symbols, panel B), and particle modal diameter (black symbols, panel C) calculated for the entire population (filled diamonds) and for two separate modes: Mode I (cross) and Mode II (empty circle). Panel C includes the mean diameter (filled purple diamonds) and the $d_{6,3}$ (filled purple squares).

Early in the flame (H<10 mm) when the size distribution is unimodal, N increases (~34%), FV doubles and particle size remains basically constant (Panel C). For H>10 mm, when both mode I and mode II appear, the slopes of N, FV, and d change drastically. As the number concentration of mode II becomes significant with respect to that of mode I, the slope of N changes sign and begins to decrease for the total population, mode I and, less drastically, for mode II. Contemporaneously, the total volume fraction increases with a notably higher slope that follows closely that calculated for mode II, while the volume fraction of mode I decreases slightly. The decrease in N observed for H>10 mm indicates that coagulation becomes a more significant particle dynamic when the size distribution

includes mode II. Since the N at H=10 mm is only marginally (~1.34 times) higher than N at H=7 mm, particle coagulation seems to increase because of the appearance of mode II rather than a significant increase in N. The fact that the increase in FV of the total population follows closely that of mode II indicates either a surface growth mechanism that occurs preferentially on mode II or persistent nucleation combined with coagulation throughout the entire post-flame zone. Even if the flame is considered non-sooting (does not produce material that absorbs/fluoresces visible light (De Filippo *et al.*, 2007)), mode II shows drastically different behaviours than mode I since it has a faster coagulation rate and is hydrophobic or not trapped in water samples where only mode I is observed (Sgro *et al*., 2007a; D'Alessio *et al*., 2007). This opens the question about the nature of mode II particles, and future work is needed to determine if these particles have a different chemical structure than mode I, which may influence their surface reactivity.

In any case, the results relative to mode I are generally consistent with the conceptual framework for particle inception advanced in earlier works based on UV-visible optical measurements (D'Alessio *et al*., 1998; Minutolo *et al.*, 1999). These earlier works found that Nanoparticles of Organic Carbon (NOC) with a $d_{6\text{-}3}$=2-3 nm are formed just after the flame front early in the flame (H=2-3 mm), and coagulate at a rate that is significantly slower than their collision rate in the post-flame zone (H>3 mm) (D'Alessio *et al*., 2005).

4.4.2 C/O=0.65: experimental and numerical results

Initial condition to the numerical model is the measured size distribution at H=7mm (green symbols in Figure 4.6), with the particle diameter converted from the measured mobility to real diameter using equation 1.1, described in Chapter *First*.

Figure 4.8 compares the measured size distributions (symbols, exp) with size distributions predicted by the coagulation model assuming either a size-dependent coagulation efficiency (γ_{SD}, solid line) or that every collision results in particle coagulation (γ=1, dotted line) for three different heights: H=8mm (Panel A), H=10mm (Panel B) and H=15mm (Panel C). The model considering size dependent coagulation (γ_{SD}) predicts that mode I particles survives through the entire post-flame region, in close agreement with the measured results. Instead, the modal diameter predicted assuming all collisions result in particle coagulation or coalescence (γ=1) quickly increases to a value that is significantly larger than the measurements. Also, the number concentration predicted by the model assuming γ=1 is much lower than the measured number concentrations. Predictions assuming γ_{SD} are in much better agreement than the γ=1 assumption for mode I and total N measured later in the flame, but the number concentration of mode II is significantly lower than the measured value for both considerations (γ_{SD} and γ=1). Coagulation alone cannot explain the measured broadening of the size distribution and the eventual appearance of mode II late in the post-flame region (Panel C). This discrepancy may be either due to persistent nucleation balanced by coagulation or surface growth and coagulation.

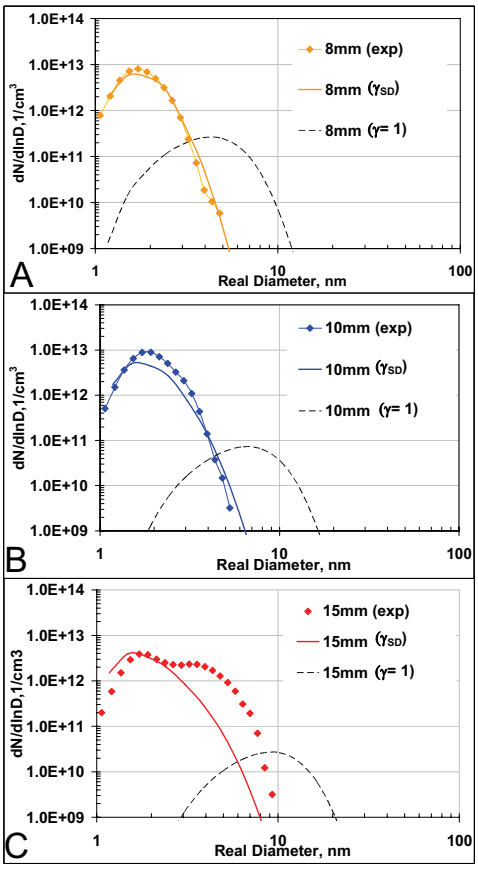

Figure 4.8 - *Size distributions measured (symbols) or calculated numerically (lines) assuming a size-dependent coagulation efficiency (solid line) or that every collision results in a coagulation (dotted line), at H=8 (A), H=10 (B), and H=15 mm (C).*

To investigate whether persistent nucleation balanced by coagulation assuming no thermal rebound (γ=1) can explain the bimodal size distributions measured in this flame, inception was later included to the coagulation model considering two inception rates for mode I: 1) dN/dt is equal to that measured early in the flame (between H=7-10 mm, 12-17 ms), where the measured size distributions is relatively unchanging except for a slight increase in N, and 2) dN/dt is equal to the slope assuming zero mode I particles at the flame front and N measured at H=7 mm (12 ms). Figure 4.9 indicates that the inception-coagulation model in both cases is unable to reproduce the high number concentration measured for modes I and II, and it incorrectly predicts a significant amount of particles larger than 10 nm, which are not measured by the DMA. Any assumed inception rate, even if it were changing with H would only add more material, which combined with coagulation (assuming no thermal rebound) would cause the model to predict a larger size distribu-

tion with lower number concentration compared to the measurements. The only way that inception and coagulation (assuming no thermal rebound) could explain the measured size distributions would be if oxidation also played a significant role in stunting the growth and consuming particle mass of mode I, which seems unlikely. A more complex model combining gas phase chemical kinetic growth with particle dynamics is needed to more rigorously examine the role of surface growth and oxidation on incipient nanoparticles and further work is needed to determine if mode II particles have a different chemical structure than mode I, which may influence their surface reactivity. This analysis is left for future activities.

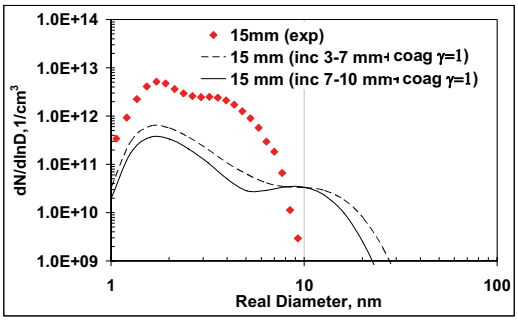

Figure 4.9 - Predicted size distributions at H=15mm with a model considering inception and coagulation (γ=1, no thermal rebound). The solid line assumes that the inception rate, dN/dt, is equal to that measured early in the flame for H=7-10 mm, and the dotted line assumes a higher dN/dt equal to the slope calculated from the measured N at H=7 mm and an assumed zero particle concentration at the flame front (H=3 mm).

4.4.3 C/O=0.63 & C/O=0.60: experimental results

Nanoparticles generated from two other rich premixed ethylene-air flames (with a C/O lower than 0.65) were also experimentally investigate by means of the same experimental setup as described in the previous paragraphs of this chapter.

Figure 4.10 shows the size distributions measured from a C/O=0.63 flame at 9 heights in the range from 7 to 16 mm. The heights investigated were actually 13 but some of them are not displayed to make Figure 4.10 as clear as possible. However the integrated values of their particle number and volume fraction are displayed in Figure 11and therefore no useful is missing. Early in the flame the size distribution was monomodal, with the modal diameter shifting from ~1.9 nm (at 7mm) to ~2.3 nm (at 13mm). Later in the flame (at 15mm) a shoulder started to appear from mode I particles, showing a similar behaviour to what already discussed for the C/O=0.65 flames (but for a different range of heights). The integrated particle number concentration and volume fraction displayed in Figure 4.11 seems to indicate three different regions where the particle growth processes change. In the step from 7 to 11mm, the number concentration increased ~4 times while the volume fraction about a factor of 6. In the second step from 11 to 15mm, the increase is less steep (~1.5 times) for both the parameter while from 15 to 16 mm the slope changes sign.

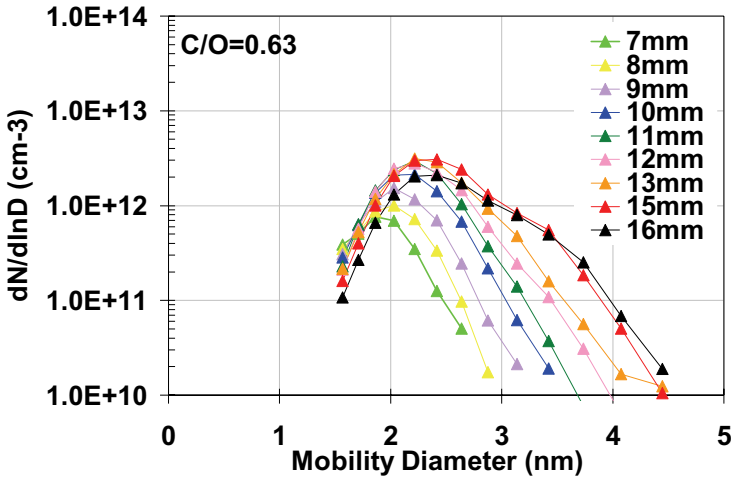

Figure 4.10 - Particle size distribution measured at different heights above the burner surface in an ethylene-air flames with C/O=0.63 and unburned gas velocity =10 cm/s.

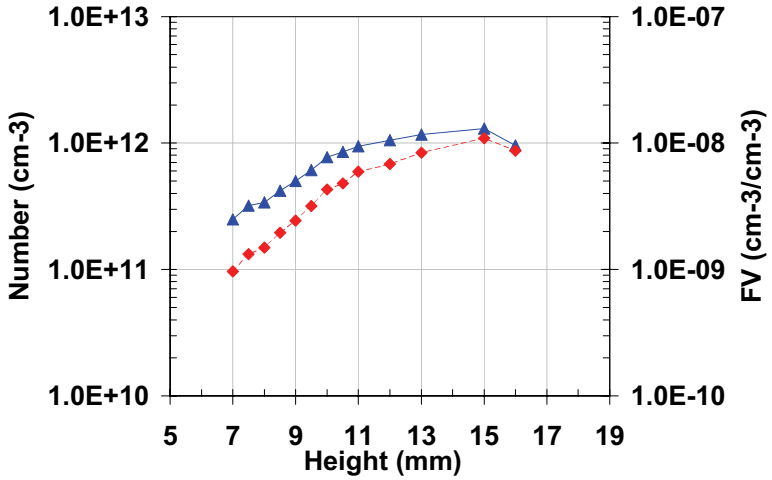

Figure 4.11 – Flame C/O=0.63: integrated particle number concentration (blue solid line-filled symbols, primary axis) and volume fraction (red dotted line-empty symbols, secondary axis).

If we consider that this flame has a slightly higher flame temperature than that of C/O=0.65, the data of Figure 4.10 and Figure 4.11 are obtained for different residence time with respect to those discussed previously for the flame C/O=0.65, namely time axis is changing relative to the height above the burner.

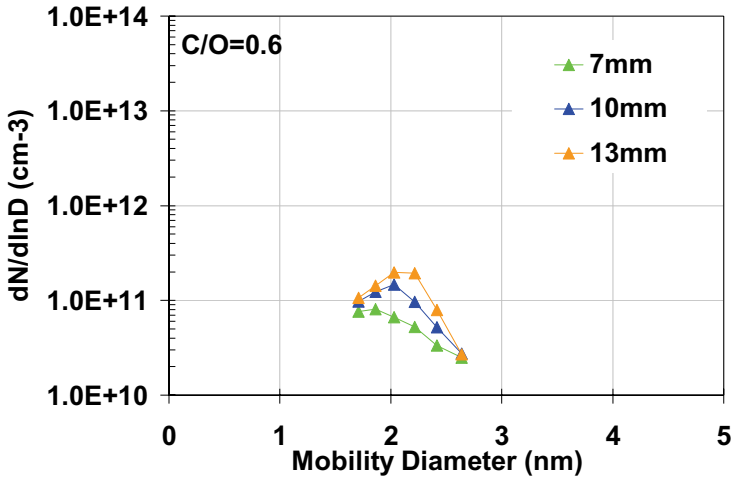

Figure 4.12 - Particle size distribution measured at different heights above the burner surface in an ethylene-air flames with C/O=0.60 and unburned gas velocity =10 cm/s.

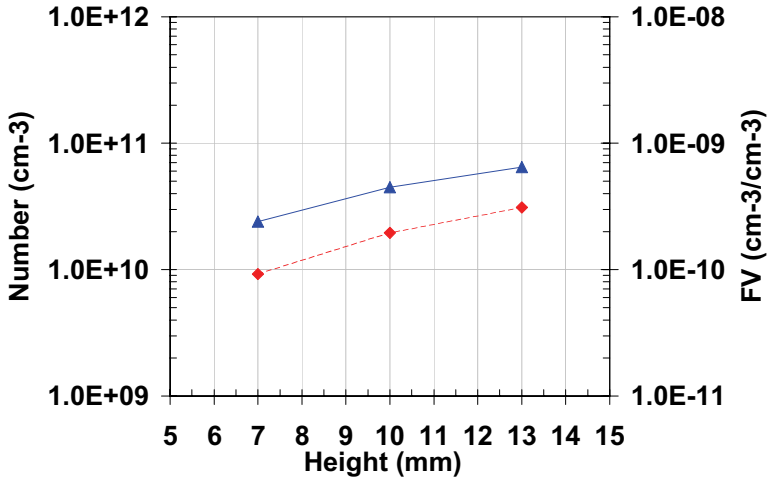

Figure 4.13 - Flame C/O=0.60: integrated particle number concentration (blue solid line-filled symbols, primary axis) and volume fraction (red dotted line-empty symbols, secondary axis).

However, in the absence of detailed flame temperature profiles for this C/O=0.63 flame, it can only be inferred that the range of heights from 9 to 15mm for C/O=0.63 is basically correspondent to that from 7 to 10mm for C/O=0.65. At the same time, H>15mm for C/O=0.63 seems to coincide with that from 11 to 15mm for C/O=0.65. In other words, it is possible to extend also to this C/O=0.63 flame (at least for heights from 11 to 16mm) the same considerations on particle growth discussed previously for the C/O=0.65 flame.

Figure 4.12 and Figure 4.13 display few data from a C/O=0.6 which represent the C/O ratio below which the sampling-probe-DMA system was not able to measure nanoparticles.

4.5 Effect of flame gas velocities

Figure 4.14 shows measured size distributions at different flame gas velocities with the horizontal probe HP-NA1 fixed at H=10mm and fuel to oxidant ratio constant with C/O=0.65. The variation of the cold gas velocity produced a change of the flame temperature, which was measured with a thermocouple (type R, joint diameter = 330 µm, wires covered with Al_2O_3 insulators to minimize surface effects). Temperatures were corrected for radiation effect following the procedure described by Shaddix (1999).

Increasing flame temperature from ~1650 K to ~1750 K caused the shoulder (mode II) to decrease without significantly affecting mode I. A further increase in temperature to ~1820 K caused the shoulder to completely disappear and showed also a significant decrease in model I particles.

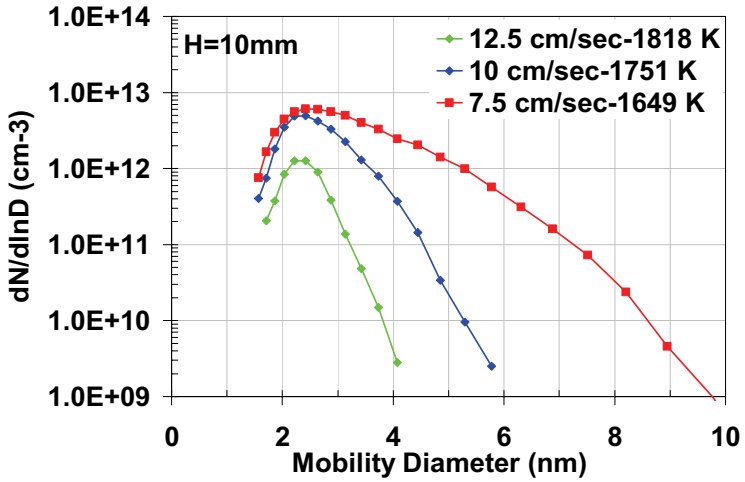

Figure 4.14 - Measured size distributions at three different flame gas velocities: 12 cm/s (green symbols), 10 cm/s (blue symbols) and 7.5 cm/s (red symbols). Horizontal probe fixed at H=10 mm and C/O ratio =0.65.

The trends in Figure 4.15 clearly indicate that the volume fraction (mainly related to Mode II of NOC) constantly decreased as the flame temperature increased. Conversely, the number concentration (basically related to Mode I) slightly decreased (less than 2 times) in the first step from ~1650 K to ~1750 K and then rapidly decreased (~6 times) as the temperature raised to more than 1800 K.

The reduction of surface growth and inception processes at higher temperature may be due either to an increased tendency to undergo thermal rebound and not interact with (coagulate, or adhere to) other NOC or gas phase molecules involved in surface growth reac-

tions or to the reduction of gas phase precursors important for inception/surface growth (or both considerations are relevant). Considering that mode I NOC growth occurs mainly because of inception while mode II NOC growth is due to coagulation and surface growth (and not inception), the reduction of mode I at very high temperature may be due to the decrease in the concentration of 2-3 ring PAHs, since NOC inception has been proposed as a fast polymerization process of 2-3 ring PAHs (D'Anna *et al*., 2001). In other words, we are on the down side of the bell-shaped temperature curve so that an increase in temperature causes a reduction in the precursor material important for mode I NOC. Additionally, it also seems that surface growth is affected by changes in temperature more than coagulation, and seems to occur at a higher rate at lower temperatures.

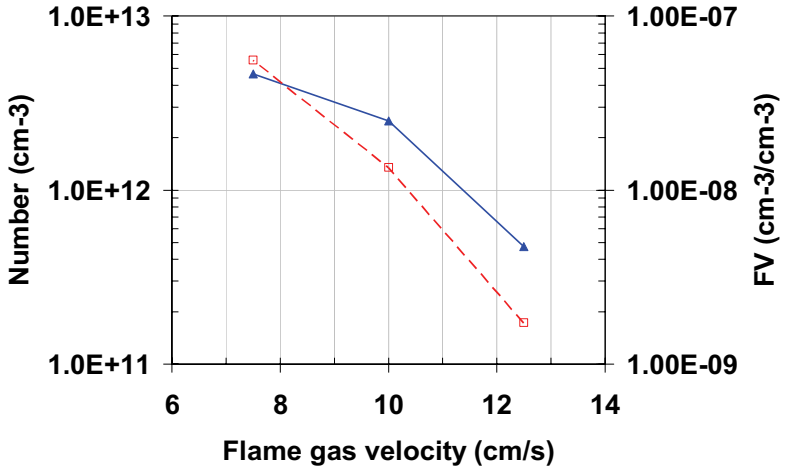

Figure 4.15 - *Integrated values of number concentration (blue solid line-full triangles, primary axis) and volume fraction (red dotted line-empty squares, secondary axis)*

In principle, a second effect should be considered. Increasing gas velocity increases flame temperature and this produces a change of the time axis relative to HAB. Namely the time to reach 10mm is shorter for the 12.5 cm/s flame (~16.4 ms) compared to the 7.5 cm/s flame (~18 ms) and to the 10 cm/s (~17 ms). Thus the decrease in particle number concentration with increasing gas velocity could just as well be due to the sampling point being earlier in the flame, as it is dependent on the flame temperature. A simple comparison with data in Figure 4.7 could help to quantify the importance of this second effect. Looking only at each residence time, the data for the 12.5 cm/s flame would correspond to H=9.5mm in Figure 4.7 whereas the data for the 7.5 cm/s flame would match that at H=10.5mm in Figure 4.7. However the respective size distribution did not match at all: the one at 7.5 cm/s has a lower number concentration (~10 times) and that at 7.5 cm/s is broader (FV is 2 times higher). Therefore this second effect can be considered negligible.

4.6 Effect of fuel employed: comparison with methane flames

Figure 4.16 shows the measurements performed on rich premixed flames burning methane and oxygen. The sampling and analysing procedure was identical to that described in section 4.3 for the ethylene-air flame. Flow rates were varied in order to cover the C/O ratio from 0.43 and 0.5, where a yellow luminosity started to be eye-visible, with the cold gas velocity fixed at 4.74 cm/s. These flames were similar to those investigated by Ciajolo *et al.* (1994) and only when studying the C/O=0.5 flame particle deposits were observed onto the probe orifice, thus affecting the optimal sampling procedure.

At increasing C/O ratio from 0.43 to 0.47, the modal diameter of the 2nm peak measured at C/O=0.43 (green symbols) slightly shifted towards larger sizes. Simultaneously the number concentration rapidly increased. When the yellow luminosity of the flame increased (C/O=0.5), the particle size distribution became bimodal with the lower mode at 3-4 nm and the larger size mode at ~ 10nm.

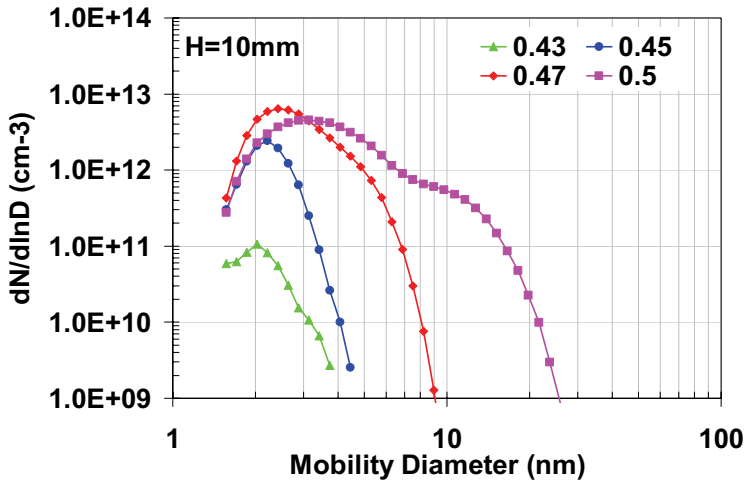

Figure 4.16 - Particle size distribution measured at H=10mm in premixed methane-oxygen flames with C/O=0.43 (green symbols), 0.45 (blue symbols), 0.47 (red symbols), 0.5 (purple symbols) at cold gas velocity = 4.74 cm/s.

Figure 4.17 displays the particle number concentration (blue solid line-solid-full symbols) and the volume fraction (red dotted line-empty symbols), respectively on the primary and secondary axis, calculated from the integration in the size range between the minimum (d_m=1.4 nm) and the maximum diameter measured for each case. The number concentration increased with the C/O ratio from C/O=0.43 to C/O=0.47 while it remained practically unchanged in the step from C/O=0.47 to C/O=0.5, where soot particle deposited onto the walls of the probe orifice. On the contrary, the volume fraction increased with a almost constant slope over the C/O range from C/O=0.43 to C/O=0.47. The slope of this increase reduced in the last step from C/O=0.47 to C/O=0.5.

It is not possible to make a direct comparison between results from the ethylene and the methane flames since the operating conditions, e.g., flame temperature and carbon to oxygen ratios, are different. However, observing those flames below the onset of soot formation (thus, excluding the C/O=0.5 methane flame) it is possible to find some analogies.

First, the peak around d_m=2.2 nm is measured in all the conditions investigated, both changing the equivalence ratio and the nature of the fuel, suggesting that the formation of these 2nm incipient particle is not strictly related to the nature of the fuel (at least when the fuel is a simple small hydrocarbon). Secondly a broadening of the 2nm mode towards larger sizes and an overall increase of the volume fraction was observed for richer flames. The increase in the overall volume fraction is mainly a consequence of the more carbon available for the combustion process but it is interesting to observe that the first 2nm particle mode does not shift immediately towards larger sizes, indicating that these incipient particles do not tend to grow rapidly and may therefore survive in the environment.

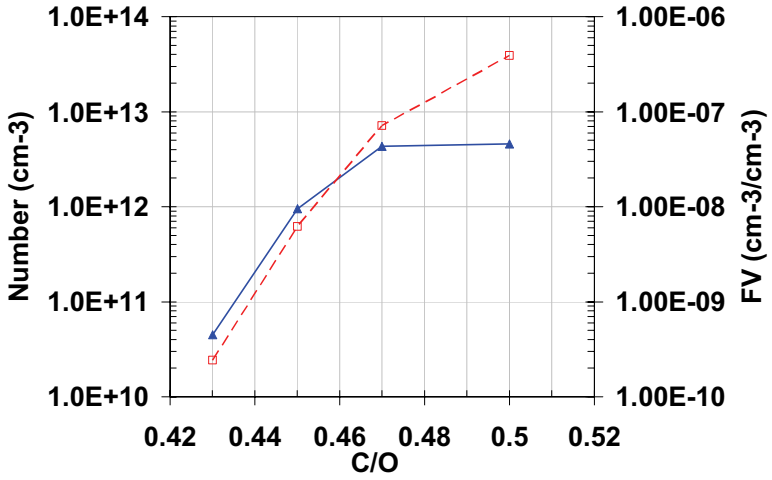

Figure 4.17 - Particle number concentration (blue solid line-filled symbols, primary axis) and volume fraction (red dotted line-empty symbols, secondary axis).

Fifth Chapter

Experimental results: behavior of flame-generated nanoparticles in a residence tube

5.1 Introduction

The purpose of this chapter is to present preliminary studies on the behavior, in a residence tube at ambient conditions, of nanoparticles sampled from rich premixed flame in burning conditions before and after the on-set of soot formation. The idea is to use a residence tube as the exhaust of common combustion sources, such as the engine or domestic cooking gas appliances, to investigate the variations in the measured size distributions of NOC and soot particles in different environments: different humidity conditions, presence of inorganic nanoparticles, of organic species and metallic nanoparticles, interaction with ozone, sulfates and nitrates. In addition, the variation of residence time due to the length of the tube and the aerosol flow rates is indicative of the lifetime of these combustion-generated nanoparticles. The general purpose of this study is to determine how two types of flame-generated nanoparticle develop before being emitted into the atmosphere.

In this thesis, this study has been only started and not yet concluded. This is the reason why these results have to be considered preliminary. The majority of the work was made at the Chemical Dynamics Beamline at the Advanced Light Source in Berkeley, California. The flame studied here were slightly different from those investigated in the previous chapter, resulting in more sooting flames. The nanoparticles were generated in an atmospheric pressure premixed ethylene-air slightly sooting flame with a carbon to oxygen ratio ranging from C/O=0.65 to C/O=0.7. Air and ethylene were supplied to the burner via MKS mass flow controllers, after calibration with a bubble flow meter, at an unburned gas velocity equal to 5 cm/s. The flat flames were stabilized on a 6-cm diameter water cooled McKenna burner by a stainless steel plate located at a height above the burner surface, H=30 mm.

Size distributions were alternatively measured at two distances from the burner surface, H=10mm and H=20mm, using the probe HP BE1 to sample and transport flame generated products to the Scanning Mobility Particle Sizer (SMPS). The height above the burner, H, was varied by moving the burner vertically with respect to the fixed dilution probe using a translation stage that gives an accuracy of +/-0.1mm for H.

The sample flow from the flame was controlled by a slight vacuum monitored downstream of the orifice. CO2 measurements from a stoichiometric flame (C/O=0.33) with a non-dispersive infrared analyser (EGM-4 Environmental Gas monitor, PP Systems) gave information on the dilution ratio at a fixed diluting flow. The sampled flame products mixed with a slightly turbulent flow of room temperature particle-free nitrogen

(QN_2=23.2lpm, STP, Reynolds number in the probe, Re= ~4000). After the mixing at the sampling point (Point C in Figure 5.1) the total aerosol travelled about 70 ms before arriving at a Swagelok tee (Point D in Figure 5.1) where 1 L/min was sent to the SMPS and the rest to the exhaust. The dilution ratio was kept fixed at the same value in order to sample the same amount of material from the flame. If the experiments reported in Chapter 4 utilized rapid dilution to quench flame chemistry and aerosol dynamics in order to capture the salient features of the soot particle size distributions, as they exist under flame conditions, the experiments presented in Chapter 5 were made at a lower dilution ratio (~$3*10^3$) to examine the particle behaviour outside of the flame. Whether or not the sampling was truly representative of the flame was of no importance in the present investigation because it simply defined the initial condition for the particles once they entered the probe/tube. To assure repeatability, the analysis was repeated 3 to 5 times cleaning the orifice before every single scan since, due to the nature of these flames, particles deposition onto the orifice wall could have distorted the sampled amount of particles. Furthermore, data were not corrected for the dilution.

Particle size distributions were recorded with a scanning mobility particle sizer (TSI SMPS) consisting of an impactor (Type 0.071 cm), a neutralizer, nano-DMA (TSI 3085 DMA), and a condensation particle counter (TSI 3025A CPC). With the sheath and aerosol set to 15 L/min and 1 L/min, respectively, this system covered the 2-64 nm range, while with the sheath and aerosol flow set to 3 L/min and 0.3 L/min, respectively, this system covered the 4.6 nm to 160 nm range. Each scan lasted 75 s (scan up time 60 s plus retrace time 15s) and, in all cases, data were corrected for diffusion losses within SMPS and for multiple charge corrections, both corrections provided by AIM TSI Software.

Figure 5.1 schematically reproduce the experimental setup for this type of study.

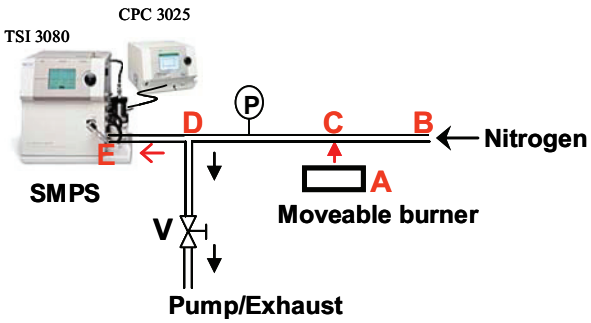

Figure 5.1 –Schematic design of the experimental setup[1]

[1] A= Flame/Burner; B=probe inlet; C=probe orifice/mixing between sampled aerosol and dilution nitrogen; D=Swagelok tee; E=inlet of the SMPS (before entering the impactor); V= needle valve on the exhaust line.

5.2 Effect of residence time on the measured size distributions

Table 5.1 summarizes the main characteristics of the different sampling line employed to vary the residence time from the sampling point (Point C in Figure 5.1), which can be considered as the initial position for the sample aerosol entering the probe, to the inlet of the SMPS (Point E in Figure 5.1).

Table 5.1 – **Summary of the sampling lines and corresponding residence times**

Name	Distance	Length, m	Aerosol Flow, L/min	Flow regime	Residence time, s
Case 0	CD	0.6	23.3	Slightly turbulent	0.069
Case 1	DE	0.08	1	laminar	0.105
Case 2	DE	0.08	0.3	laminar	0.35
Case 3	DE	3	1	laminar	2.96
Case 4	DE	3.27	1	laminar	4.58
Case 5	DE	3	0.3	laminar	9.85
Case 6	DE	3.27	0.3	laminar	15.24

The distance CD from probe orifice to Swagelok tee was kept fixed for all the cases studied. To change the residence time before entering the SMPS, namely in the path from the Swagelok tee (Point D in Figure 5.1) to the SMPS inlet (Point E in Figure 5.1), tubes of different length and the sample aerosol of the SMPS were both varied. It is worth noting that for Case 1 & 2 the 8cm long tubes were black conductive tubes, for Case 3 & 4 a 3m long copper coil tube (ID≈6mm) was used and for Case 5 & 6 the 3m long copper coil tube was used in series with a stainless steel residence chamber (~0.027cm^3). No influence of the different material employed was observed on the measured size distributions.

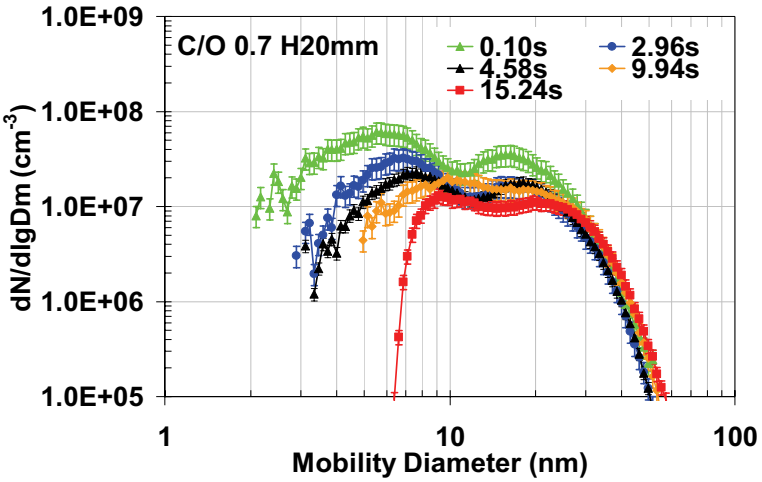

Figure 5.2 – Size distributions of a C/O=0.7 flame (unburned gas velocity set at 5 cm/s) at five different residence times. Data are corrected for diffusion losses within the SMPS and along the distance DE. Data are not corrected for dilution and H=20mm.

Figure 5.2 displays the size distributions measured by the SMPS for five different residence times when the particles were sampled later (H=20mm) in a flame with C/O=0.7: 0.1 s (green symbols), 2.96 s (blue symbols), 4.58 s (black symbols), 9.94 s (orange symbols) and 15.24 s (red symbols). The times refer to those travelling the distance DE (relatively to each other the time in the path CD is the same) and the data are corrected for the diffusion losses along the distance DE (losses are negligible along the distance CD). Error bars indicated the repeatability of these measurements. The starting condition (time 0.1 s) is a bimodal size distribution with the first mode at about ~5.5 nm and the second mode peaked at about ~ 15.7 nm. It is worth noting that the lower tail of the size distribution at 15.24 s deeply decreases, differently from the other three cases. This is likely due to the fact that these points were close to the lowest detection limit of the instrument, for that specific setup.

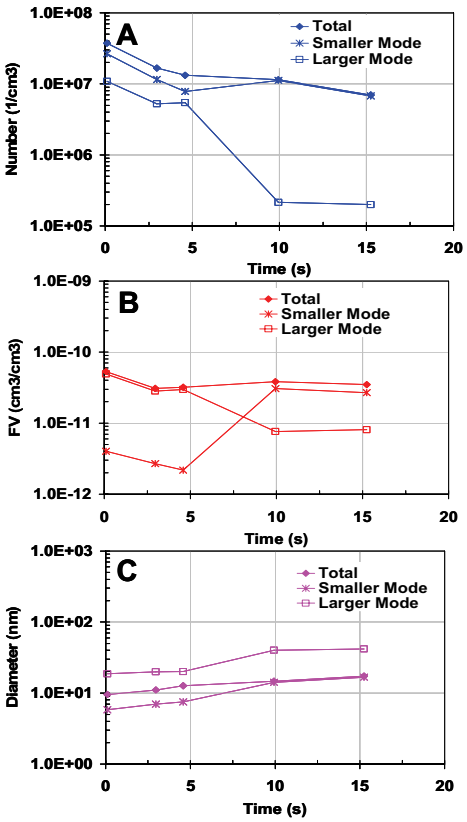

Figure 5.3 - Integrated values of number concentration (blue symbols, panel A), volume fraction (red symbols, panel B), and particle modal diameter (black symbols, panel C) calculated for the entire population (filled diamonds) and for two separate modes: smaller mode (cross) and larger mode (empty squares).

Figure 5.3 shows the trends relative to the integrated number concentration (Panel A), the integrated volume fraction (Panel B) and the mean geometric diameter (Panel C). These parameters have been calculated considering an integration of the total signal and also a partial integration for the two separate modes displayed in Figure 5.2. For the latter, the upper integration limit for the smaller mode (and lower integration limit for the larger mode) was set in correspondence of the dip between the two modes.

The total volume fraction was practically constant (variations are well within the repeatability shown in Figure 5.2) indicating that the estimation for particle diffusion losses was correct and that condensation processes of gas species onto the particle surface were not present in this cases. Thus, the observed variations of the size distribution were likely attributable to coagulation processes as confirmed by the decrease in the number concentration and the increase in mean particle diameter.

Figure 5.4 displays the size distributions measured by the SMPS for four different residence times when the particles were sampled from a less rich flame (C/O=0.65) with the horizontal probe fixed at H=20mm. The starting condition (green symbols) is again bimodal but differently from the cases investigated for C/O=0.7 the first smaller mode is peaked at ~2 nm and the second larger mode is at 3nm. As already discussed in Chapter 2, unfortunately the analyzer employed for these measurements lose its efficiency below 3nm and therefore it was not possible to carefully investigate this smallest mode as already done for the premixed laboratory flames presented in Chapter 4. Furthermore, to achieve a residence time of 15.24 s (red symbols), the SMPS was set with the sheath and aerosol flow at 3 L/min and 0.3 L/min, respectively, which consented to cover the 4.6 nm to 160 nm range. Thus the signal (likely present) below 4.6 nm were completely missed.

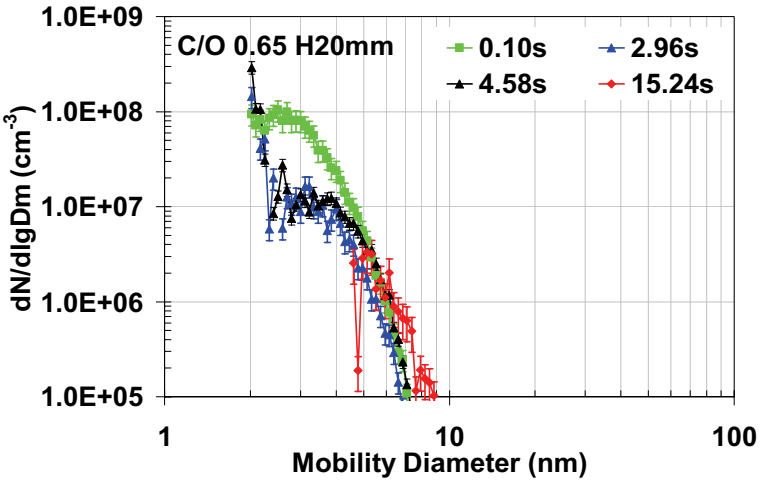

Figure 5.4 - Size distributions of a C/O=0.65 flame (unburned gas velocity set at 5 cm/s) at three different residence times. Data are corrected for diffusion losses within the SMPS and along the distance DE. Data are not corrected for dilution and H=20mm.

At present, a measurement at intermediate time between 4.58 s (black symbols) and 15.24 s (red symbols) has not been yet performed and it would be necessary to see how the particle size distributions change in that step.

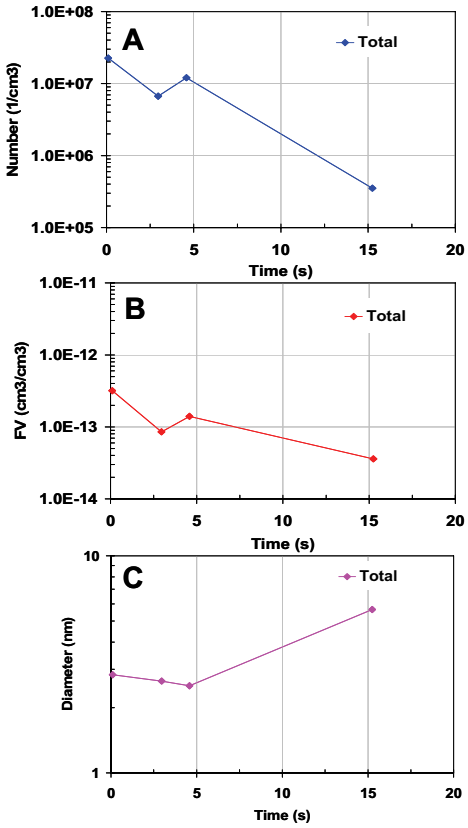

Figure 5.5 - Integrated values of number concentration (blue symbols, panel A), volume fraction (red symbols, panel B), and particle modal diameter (black symbols, panel C) calculated for the entire population (filled diamonds).

Figure 5.5 shows the trends relative to the integrated number concentration (Panel A), the integrated volume fraction (Panel B) and the mean geometric diameter (Panel C) for the size distributions displayed in Figure 5.4. These parameters have been calculated considering an integration of the total signal since the signal at the dip between the smallest mode and the larger mode is very noisy due to the low detection efficiency of the instrument. In this case, it is worth noting that the trend for the volume fraction (Panel B) was not constant and was not within the experimental error. This decrease may be likely due either to the lack of material below 4.6nm for the last point (red symbols in Figure 5.4) or to an under-estimation of the diffusion particle losses. The latter possibility indicates that tradi-

tional equation for diffusion losses may under-estimate the losses when particle size is below 3 nm or also that they depend on the nature of these nanoparticles as well.

5.3 Effect of humidity on the measured size distributions

The experimental setup described in Figure 5.1 was modified in order to perform measurements on the size distributions of flame-generated nanoparticles when the humidity conditions and the residence time were changed in a residence tube.

Figure 5.6 displays the modifications to the previous experimental setup.

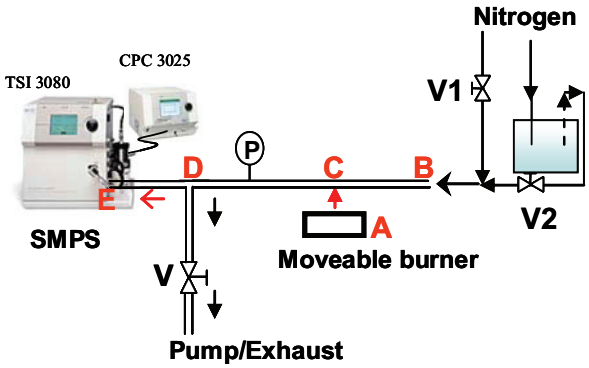

Figure 5.6 – Experimental setup to change the humidity of the diluting nitrogen and investigate its effect on flame-generated nanoparticles.

The main modification was related to the line that transports the nitrogen to the sampling probe. This line was alternatively split into two parts by the use of valves (see Figure 5.6). In one case, with valves V2 closed and V1 open, the nitrogen was sent directly to the inlet of the horizontal probe (point B), as in the set of measurements described in the previous section. In the following, this case will be referred as Dry Nitrogen since a non-measurable value of relative humidity (RH%~0) was measured at the inlet of the sampling probe. In the other case, with valves V1 closed and V2 open, the nitrogen was first passed through a bubbler containing purified water in order to increase its relative humidity and then successively sent to the horizontal probe. The latter will be referred as Wet Nitrogen since the measured relative humidity at point B was RH%~80% ±3%. Humidity measurements were performed with OMEGA RH62C.

The sampling and analysis system were exactly the same as those described in the previous section. In this set of measurements, the nanoparticles were generated by a single premixed ethylene-air flame with the horizontal probe positioned at two different heights above the burner surface, namely H=10mm and H=20mm.

Figure 5.7 shows the size distributions measured by the SMPS when particle-free gas nitrogen, with a different content of humidity, was sent into the probe during the sampling from premixed ethylene flame with C/O = 0.7 (unburned gas velocity = 5 cm/s). The measurements were performed both with the usual sampling line (empty diamonds, 0.085s) and at longer residence time (full squares, 3s). Red curves are the size distributions in the case

of Dry Nitrogen (RH 0%) while blue curves refer to the measurements when the nitrogen presented a RH≈80%. The data are not corrected for the dilution but are corrected for diffusional losses.

At shorter residence time (0.085 s), both the size distributions showed a modal diameter peaked at about ~3nm but slightly changes around 2nm and at the tail of the size distributions were also observed. These differences seemed to be not in the experimental error (~30%) and were likely indicative of an effect of the different humidity conditions but, at present time, there is not any clear explanations for it. At longer residence time (3s), when the mean particle diameter was shifted at about ~4nm, no particular differences were observed in the measured size distributions.

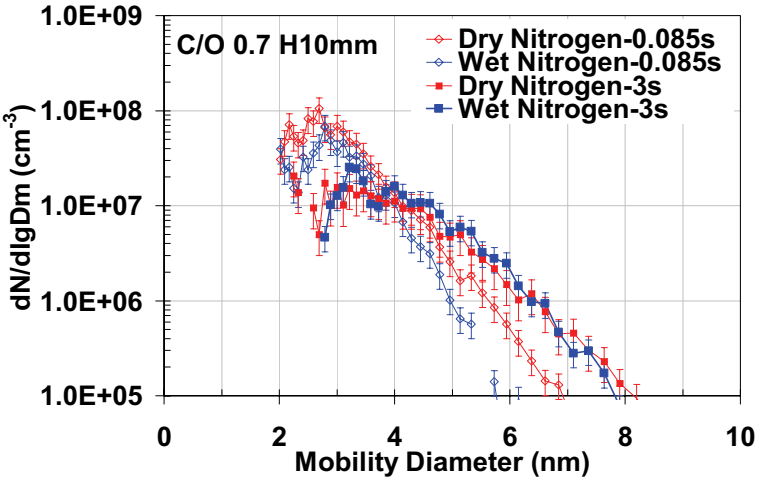

Figure 5.7 – Size distributions of nanoparticles sampled from a premixed ethylene-air with C/O=0.7 at H=10mm, at two different residence time (0.085s-dyamonds and 3s-squares) and with dry (red symbols) and wet (blue symbols) nitrogen.

Figure 5.8 displays an analogous investigation on the nanoparticles sampled from the same flame (C/O=0.7), later in the flame (H=20mm), where the size distribution was bimodal. Independently from the residence time and the humidity conditions, the size distributions, relatively to each other, were very similar and only a small difference around the tail of the size distribution was measured.

These first measurements indicated that only at H=10mm and short residence time some discrepancies were observed in the size distributions measured with Dry and Wet Nitrogen. These results seemed to be related to the particle size since the above said conditions refer to the situation when particles smaller or about 3 nm were measured. Conversely, at higher residence time and later in the flame, when the mean particle size increases, no significant effect of the humidity content was observed.

It is also worth noting that in high humidity conditions (RH>45%), after the first measurement, all the measured data showed a signal at the end of the investigated size range, namely above 55nm, which tended to increase in time. This signal was not flame-generated. In fact, even when the flame was turned off (and the sampling line also discon-

nected), this signal was still measured and eventually disappeared only sending dry nitrogen directly at the inlet of the SMPS. However, the signal did not instantly disappear and it was necessary to run at least three-four scans in a row with dry nitrogen to see a gradual disappearance of this signal at d_m > 55nm.

The reason of its presence is likely to be related to water droplets that condense on the optics of the CPC and/or inside the DMA thus producing this unusual signal at the end of the scan.

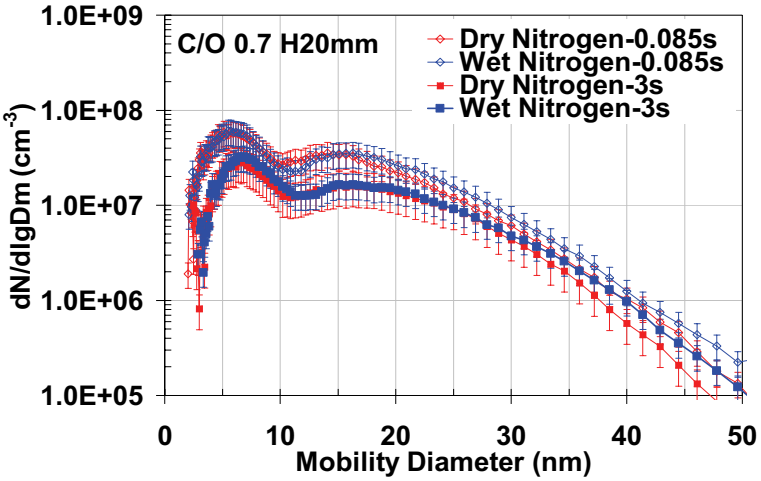

Figure 5.8 - Size distributions of nanoparticles sampled from a premixed ethylene-air with C/O=0.7 at H=20mm, at two different residence time (0.085s-dyamonds and 3s-squares) and with dry (red symbols) and wet (blue symbols) nitrogen.

5.4 Interaction of flame-generated nanoparticles with ~50nm NaCl particles

The experimental setup was again modified to perform this study on the interaction of flame-generated nanoparticles with ~50 nm NaCl particles. Figure 5.9 shows the new experimental configuration. The free-particle nitrogen flow before entering the probe was sent through a beaker containing water based solution of sodium chloride (99.99% on metal basis by Alpha Aeser). A fogger was used to generate a cloud of droplets containing NaCl nanoparticles. The nitrogen flow doped with NaCl particles was subsequently sent first through a glass heated tube and then into a diffusion dryer, containing wire screens of silica gel, in order to dry the sodium chloride particles. The temperature of the glass tube did not effect NaCl particle size distributions and most of the experiments were carried out with its temperature set at about 92°C. At point B in Figure 5.9 the total aerosol (nitrogen+ NaCl particles) entering the probe had a relative humidity of about 55%. The distance from the Swagelok tee (Point D in Figure 5.9) and the inlet of the SMPS (Point E in Figure 5.9) was varied to achieve a residence time of about ~ 10s, with the SMPS set with the sheath

and aerosol flow at 3 L/min and 0.3 L/min, respectively, to cover the 4.6 nm to 160 nm range.

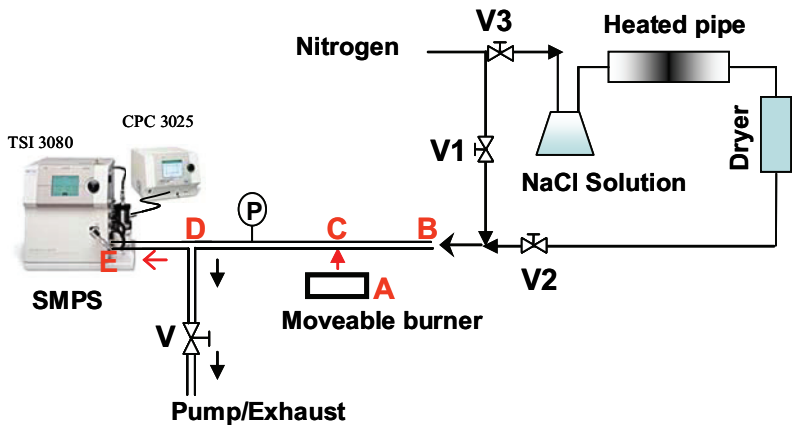

Figure 5.9 - Experimental setup to change the produce NaCl nanoparticles inside a high flow of diluting nitrogen and investigate its effect on flame-generated nanoparticles.

Measurements of only NaCl particle are displayed in Figure 5.10. The measured size distributions showed a mean diameter at about 53 nm with the tail of the distribution broadening to a value higher than 100nm.

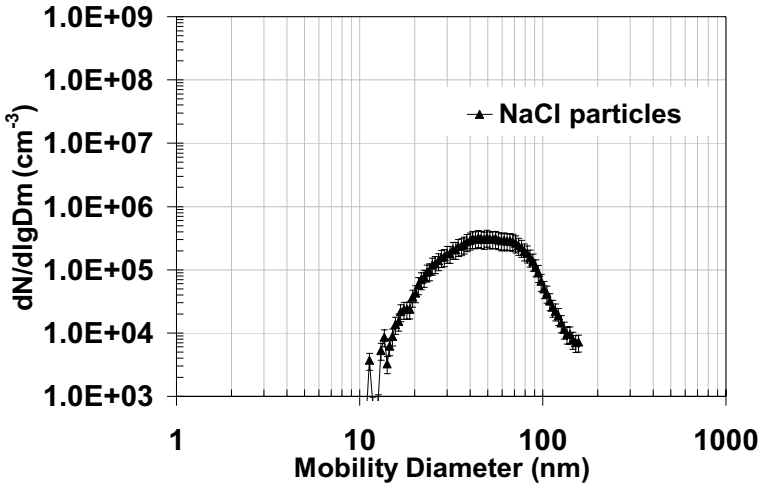

Figure 5.10 - Size distributions of NaCl nanoparticles generated by a fogger placed in a water-based solution containing 1e-5 gNaCl/cm^{3}H2O.

Figure 5.11 displays the size distributions of the flame-generated nanoparticles in the presence of the free-particle diluting nitrogen (blue symbols) and with the nitrogen doped

with the NaCl nanoparticles. The nanoparticles were sampled from the C/O=0.7 flame at H=20mm.

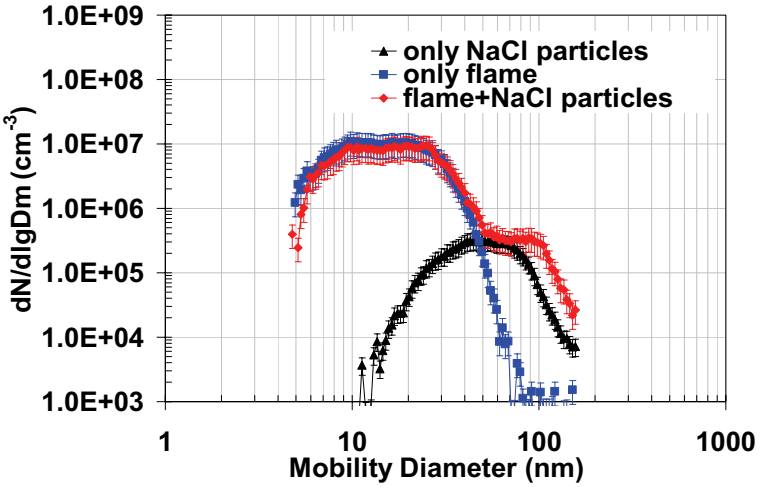

Figure 5.11 - Size distributions of flame-generated nanoparticles alone (blue symbols) and in the presence of ~53 nm NaCl nanoparticles.

As seen, the two sets of data for the flame-generated nanoparticles were the same for almost the entire size range studied. In the size range where the two nanoparticle modes overlap (above 60 nm) a slightly increase of total mass was observed.

In general, the presence of ~50nm NaCl nanoparticles did not seem to produce an effect on the flame-generated nanoparticles. Further study is necessary to see if this conclusion might be still valid for smaller size nanoparticles sampled at C/O ratio below the on set of soot formation.

Sixth Chapter

Experimental results: diesel vehicles and test bench engine

6.1 Introduction

Diesel exhaust particulate matter (PM) is characteristically bimodal in size, with the larger size mode composed of engine generated soot particles and the one at smaller diameter usually associated with hydrocarbon and sulfate nucleation. These particle modes depend on engine operation, fuel composition, lube oil, after treatment technology, and exhaust sampling procedure. It is generally accepted that the larger size mode (> 50 nm) is mainly composed by soot particles produced by high temperature combustion reactions (Harris & Maricq, 2001). Instead the nature of the smaller size mode ('nucleation mode') is still debated. On one side, it is believed that, as the exhaust cools, semi volatiles can nucleate to produce this smaller size mode. Sulfate, dilution ratio, lube oil and exhaust after treatment play an important role (Shi & Harrison, 1999; Maricq *et al*., 2002; Tobias *et al.*, 2001; Vaaraslathi *et al*., 2004 & 2006). On the other side, recent observations suggest that the nucleation mode may contain nonvolatile cores (Kittelson *et al*., 2006; Ronkko *et al.*, 2007). The source of nonvolatile cores remains unknown. On one side, Miller *et al*. (2007) suggests that as engine combustion technologies improve, the "cleaner" engines, i.e., those that generate low soot levels, will more likely to generate metallic nanoparticles whose source could be from fuel impurities, lube oil consumption, or metals derived from engine wear. On the other side, nonvolatile cores like soot particles, may also generate in the combustion chamber, formed in high-temperature combustion processes and reactions, and not by low-temperature condensation processes (Sgro *et al.*, 2008a). This hypothesis is based on the observation that nanoparticles emitted in vehicle exhausts have similar size and optical properties to the first incipient nanoparticles measured from premixed laboratory flames (Minutolo *et al.*, 1999; Barone *et al.*, 2003; Sgro *et al.*, 2007a).

In this chapter, emissions from two modern light-duty diesel vehicles and from a test bench single-cylinder engine run with commercial ultralow sulphur fuel were investigated at different vehicle speeds and exhaust gas recirculation (EGR)[1] conditions to examine the physical nature and the origin of the nucleation mode.

[1] EGR is used to reduce NOx formation by displacing air in the cylinder charge, whereby the reduced oxygen content lowers NOx formation (Ladommatos et al., 1998; Zheng et al., 2004).

6.2 Light-duty diesel vehicles: nucleation mode particles

6.2.1 Test vehicles and operating conditions

PM emissions were examined from two light-duty (LD) diesel test vehicles, both run on ultralow sulfur fuel. The vehicles were of modern design, including common rail, direct injection, and turbocharging. Table 6.1 lists their characteristics. They were run at steady state and normal road load on a 48-inch single roll, AC electric, dynamometer at Ford's Vehicle Emissions Research Laboratory in Dearborn (Michigan) (Figure 6.1). PM emissions were measured engine-out, post DOC which was positioned downstream the engine-out on the exhaust line, and post DPF, the latter positioned ~109 cm downstream the DOC.

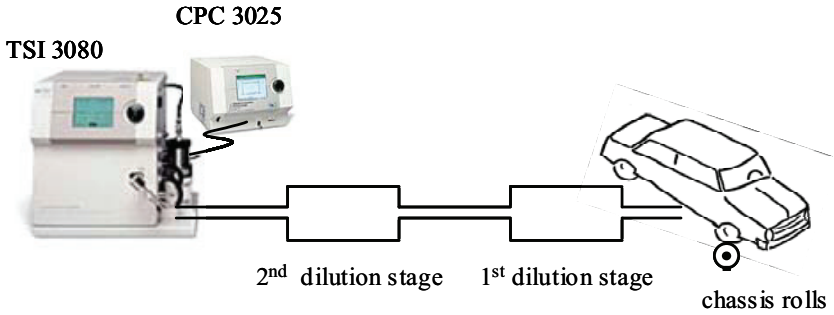

Figure 6.1 – Schematic design of the experimental setup at VERL.

Table 6.1 – **Two test diesel vehicles: main operating parameters**[2]

Test vehicle	LD diesel 2	LD diesel 3
Year	2007	2007
Engine (L)	2.7 V6	6.7 I6
Common rail	✓	✓
Turbocharged	✓	✓
# injections	2	2-3
Fuel sulfur (ppm)	9-23	9-23
Aftertreatment	DOC-SCR-DPF (prototype)	DOC-LNT-DPF

Vehicle exhaust was sampled using one or two ejector pump diluters (Dekati, Ltd.) in series. Each stage provided a dilution factor of ~7 and no qualitative effect of dilution was observed in the measured size distributions. The first stage was equipped with a heating

[2] DOC = Diesel Oxidation Catalyst; SCR = selective catalytic reduction; LNT = lean NO_x trap where NO_x is trapped on alkali or alkaline earth materials; DPF = diesel particulate filter; V6 = *V engine* with six cylinders mounted on the crankcase in two banks of three cylinders; I6 = *straight 6* or *inline 6 engine* with six cylinders mounted in a straight line along the crankcase; AC=alternating current

mantle (200 C) and supplied with heated nitrogen (200 C), which acted as both working fluid and diluent. The second stage operates at room temperature.

Tests of diesel vehicles 2&3 utilized a scanning mobility particle sizer (SMPS) consisting of ^{210}Po neutralizer (α-radiation, 2mCi, $t_{1/2}$=138 days), differential mobility analyzer (TSI 3085 'nano' DMA), and condensation particle counter (TSI 3025 CPC). With sheath and aerosol flows set to 15 L/min and 1 L/min, respectively, this system covered the 2 – 64 nm range and focused on the nucleation mode, referred as the nanoparticles with modal diameter below 50 nm (Kittelson, 1998). Data were corrected for diffusion losses during transport and within the SMPS, which become increasingly important as particle size decreases. To reduce diffusion losses during transport, the nanoDMA operated in bypass mode, which draws the sample at 5 L/min right to the DMA column entrance, and then discards 4 L/min. Overall penetration (including neutralizer, nanoDMA, and CPC) ranges from 20% at 3 nm to >90% above 65 nm. The data were also corrected for dilution and reported as particle concentration in engine exhaust.

6.2.2 Effect of vehicle speed and exhaust gas recirculation (EGR)

Light-duty diesel exhaust often lacks a nucleation mode (Maricq *et al.*, 2002; Giechaskiel *et al.*, 2005). Investigations on vehicles 2&3 furnish different information. During steady state operation at 40 mph and 70 mph, as displayed in Figure 6.2, the nucleation mode was absent and only a single 50-100 nm soot mode was measured. However a bimodal size distribution, with the lower size mode at about 7 nm, emerged at idling conditions (and also at low vehicle speed with low EGR (De Filippo & Maricq, 2008). This nucleation mode was strongly dependent on the exhaust gas recirculation as displayed in Figure 6.3.

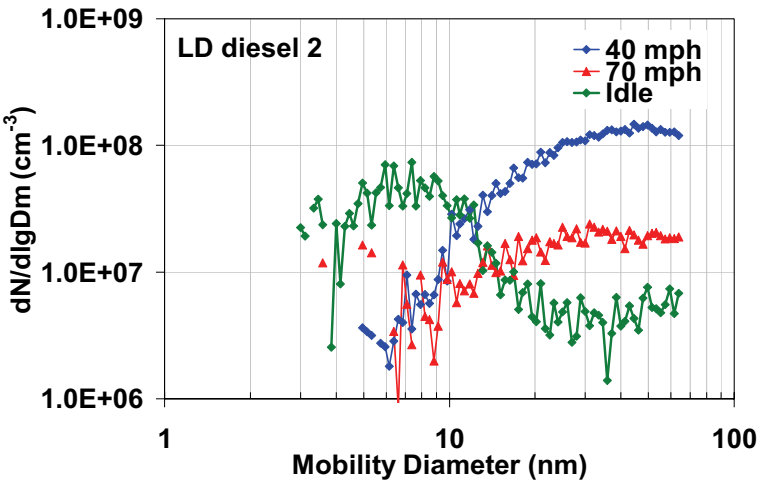

Figure 6.2 – Size distributions for LD diesel test vehicle 2 engine-out emissions: steady state speeds at 40 (blue symbols), 70 mph (red symbols) and idle (green symbols).

When the test vehicle was immediately brought to idle after a cold start, the exhaust particle size distribution began with only a soot mode (light blue symbols in Figure 6.3). After about 5 minutes of idling, the size distribution changed to bimodal. This transition accompanied a decrease in the EGR level to near zero, a procedure used to protect the oxidation catalyst from potential fouling and plugging during prolonged cold weather idle periods. If the EGR reverts to a high level (orange symbols in Figure 6.3), the size distribution again exhibited solely the soot mode.

The data displayed in Figure 6.3 are respectively the results of a single measure, corresponding to the cold start (light blue symbols), of an average of 4 runs (light green symbols) and of an average of 6 runs (orange symbols) after 2 hours from the cold start. In the latter case, it is also possible to note a signal below 3 nm. In contrast with the signal for particle size larger than 5nm, this signal was not reliable since it was measured just in the first of the six runs (orange symbols in Figure 6.4).

Therefore, even it is not possible to exclude *a priori* also the presence of material at very small sizes (below 5 nm), in this case the experimental evidence does not support this hypothesis.

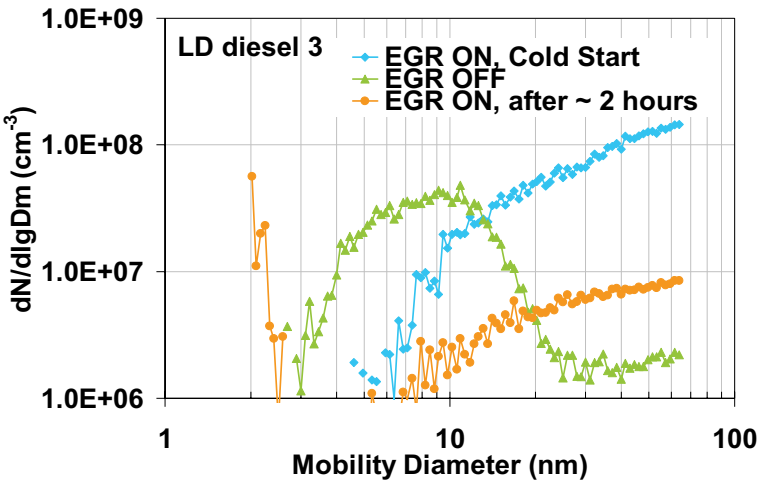

Figure 6.3 – Size distributions for LD diesel test vehicle 3 engine-out emissions at idling conditions with different EGR levels.

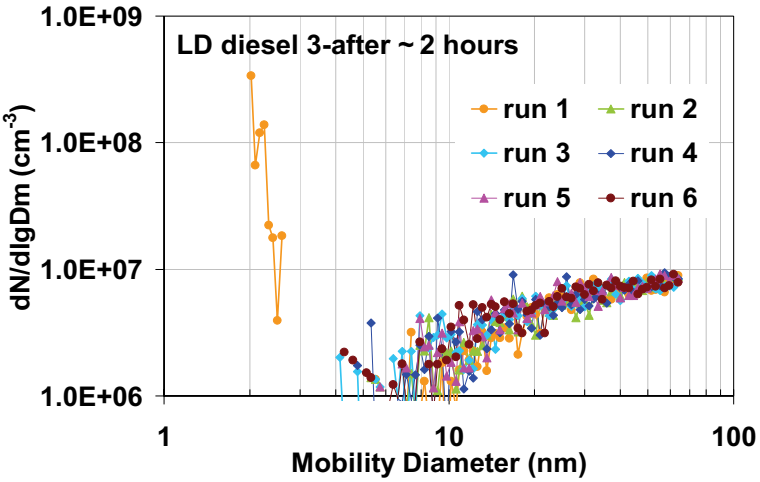

Figure 6.4 - Size distributions repeatability for LD diesel test vehicle 3 engine-out emissions at idling conditions with different EGR ON after 2 hours of measurements

6.2.3 Nanoparticle volatility & charge measurement

A heat pipe (20 cm long, 0.9 cm diameter) was inserted between the exit of the last diluter and the inlet of the SMPS to evaluate the volatility of the nucleation mode measured at idle, when the EGR is off. The traditional commercially available thermodenuder (Dekati), in which a heating tube is followed by an annular tube lined with active charcoal to adsorb the volatized gases so that they do not re-nucleate or condense, was not employed because of concern for increase particle losses below 10 nm. However the efficacy of the employed heat pipe was tested on poly α-olefin (PAO) oil aerosol (base stock of synthetic lube oil) where 98% was removed by a temperature of ~260 °C and the remaining 2% shrank to half of their original mobility diameter (De Filippo & Maricq, 2008). Losses in this approach were not separately measured, but the diesel PM data displayed in Figure 6.5 suggested that they remained less than 50% in the 3 – 20 nm size range up to a temperature of ~450 C. The data collected for test diesel vehicle 3 were in stark contrast with to POA oil droplets and indicated a 'solid', 'nonvolatile' nature for the measured nucleation mode. In fact, while geometric mean diameter remained nearly constant, decreasing only by ~1nm over the 400 °C temperature rise, particle number also did not experience drastic changes, lowering by 55% only above 400°C (see Figure 6.5). Data on test diesel vehicle 2 were in close agreement with the ones on diesel vehicles 3.

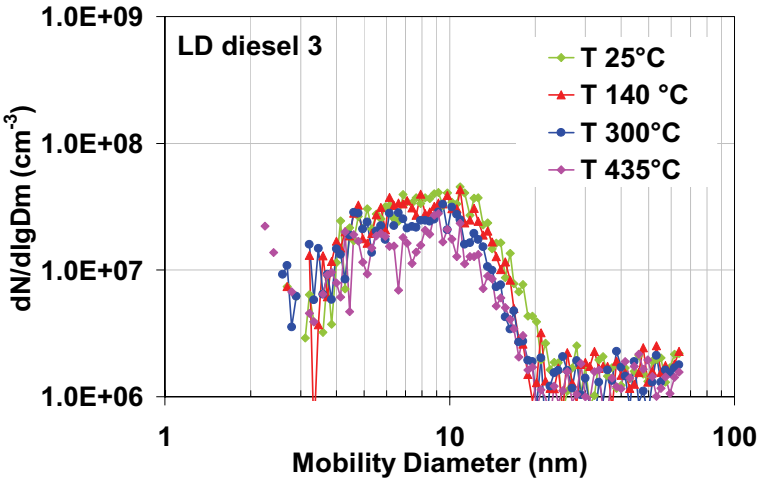

Figure 6.5 – Size distributions for LD diesel test vehicle 3 engine-out emissions at idle, when EGR is off, as a function of the thermodesorber temperature.

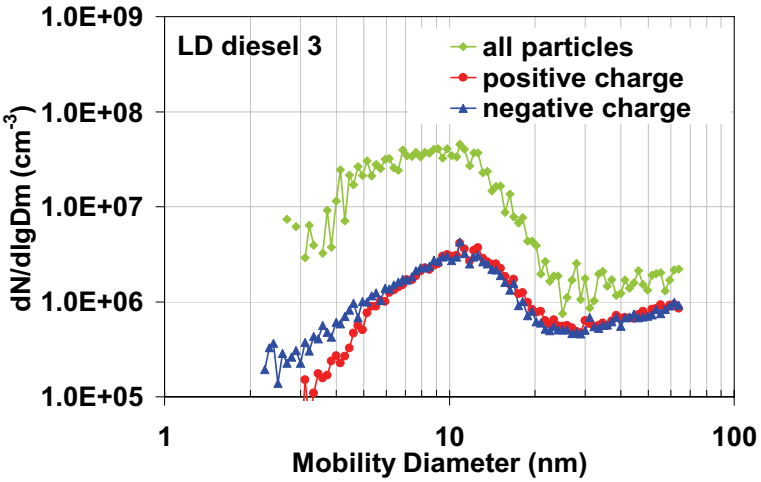

Figure 6.6 – Size distributions of all particles (green symbols) for LD diesel test vehicle 3 engine-out emissions at idle, when EGR is off, compared to those with natural electrical positive (red symbols) and negative (blue symbols) charge.

The natural electrical charge of LD diesel 2&3's idle nucleation mode was examined by comparing size distributions measured with and without first passing the sample aerosol through the ^{210}Po neutralizer. Without a neutralizer, the DMA sizes only those particles naturally endowed with electrical charge, for example through combustion (Maricq, 2006; Howard *et al*., 1973; Wegert *et al*., 1993; Wersborg *et al*., 1973). Tests on diesel vehicles

2&3 revealed that idle nucleation mode contained significant (and almost equal) fractions of positively and negatively charged particles. Figure 6.6 illustrates this for the example of LD diesel 3 by comparing the size distributions of naturally charged particles to that of the overall particle population (identical behavior was observed for vehicle 2).

It is interesting to note that below 5 nm the number concentration of negatively charged particles is ~ 3 times higher than those positively charged. In this size range, the use of an electrometer rather than a condensation particle counter would help to verify this discrepancy.

6.2.4 Effect of exhaust after treatment

As reported in Table 6.1, both test vehicles were representative of last generation of vehicles present on the roads. Therefore they were equipped with after treatment devices to reduce diesel PM emissions: a Diesel Oxidation Catalyst (DOC) to remove CO and hydrocarbons, a lean NO_x trap (LNT) or selective catalytic reduction (SCR) to reduce NO_x emissions, and a Diesel Particulate Filter (DPF) to remove the nonvolatile fraction of PM emissions collecting it on the filter layers. The effectiveness of DOC and DPF on the nanoparticles emitted from LD diesel test vehicles 2&3, run at idle when EGR was off, was evaluated comparing the size distributions collected at three points in the exhaust system: a) engine-out, b) post DOC, and c) post DPF.

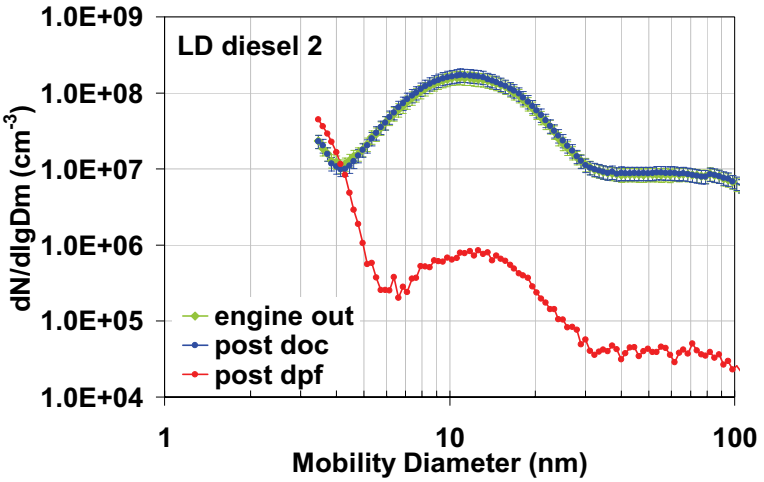

Figure 6.7 – Effect of after treatment devices on the nonvolatile nucleation mode and soot mode: size distribution for LD diesel test vehicle 2.

Figure 6.7 reports the data relative to diesel vehicle 2. The DOC had virtually no effect on the particles; the size distributions measured post DOC (blue symbols) were qualitatively and quantitatively in agreement with those at engine-out (green symbols). This was likely due to the fact that neither nuclei mode nor soot mode particles diffused sufficiently

rapidly for significant numbers to reach the channel walls for catalytic removal. Post DPF data were taken employing a single - Dekati diluter stage. As expected, the DPF removed both modes of particles and they were removed with equal effectiveness by about two orders of magnitude. The filtration did not produce significant effect on the modal diameters of nucleation particle mode and soot mode, which were practically unchanged pre and post DPF. A third peak below 5 nm was also measured in this set of measurements. However, this peak consisted of particles which were volatile (removed by heat pipe) and electrically neutral (bypassing the neutralizer reduces this peak by more than 1000).

In this thesis, nanoparticle emissions were not investigated during DPF regeneration.

6.3 Test bench single-cylinder engine: nucleation mode particles

6.3.1 Operating conditions

In this thesis, size distribution measurements were also used to investigate how different fuels and different combustion conditions influence the particle size emitted from a test bench diesel single-cylinder engine. Measurements of the bench single-cylinder engine were carried out at the Istituto Motori - CNR at Napoli, Italy. In the original configuration, the engine corresponded to the FIAT Multijet 16V architecture (unit displacement of 475cc, III° common rail generation, 4 valves, centred injector, swirl regulation, omega bowl and 16.5 of compression ratio) in the EURO IV version. In this tested configuration, as described by Avolio *et al.* (2005), the diesel engine was modified to allocate only a single cylinder. The reason of this modification has to be found in the possibility to have an instrument that, without the complications of multi-cylinder engine, permitted to isolate and to understand the effects of the different operating parameters on the engine performance.

Nanoparticle emissions were examined from the engine run, at constant load, in one case with commercial ultralow sulphur fuel (Blue Diesel, Normative EN590) and in a second case with Normal-Heptane (n-C_7H_{16}). The speed was kept constant at 1500 rpm[3] with the brake mean effective pressure (bmep) at 2 bar. Table 6.2 lists the main engine characteristics in the different cases. Emissions were measured 1m downstream the engine-out, just after the exhaust damping volume. The measured temperature at the sampling point was ~ 190°C, monitored constantly.

Engine exhaust was sampled using one ejector pump diluter (Dekati Ltd.). This stage provided a dilution factor of ~ 3.5, calibrated measuring carbon dioxide concentrations in the exhaust and in the sample flow. The diluted flow was transported to the analysis system through a 2m long copper tube (OD=6mm).

Size distributions were recorded with a tapcon EMS DMA 3/150, consisting of an Am241 bipolar ionizer, a cylindrical classifier, and a Faraday Cup Electrometer. Tests were taken with the DMA operated with a sheath flow of 50 L/min and an aerosol flow of 5 L/min with an applied voltage of 0-1250 V and 0-12500V, which respectively covered the 0.6-28 nm and 2-100nm size regions. Scan time was 170s and the data are an average of

[3] rpm = revolutions per minute

three to five runs in a row (with high repeatability), not corrected for diffusion losses during transport (~20% at 4 nm; ~ 6% at 10nm) and within the analysis system. The applied dilution was taken into account and the data are reported as particle concentration in engine exhaust at the sampling point.

Table 6.2 – **Test bench single-cylinder engine: main operating parameters**

Fuel	EGR[4]	Speed (rpm)	bmep (bar)	Prail (bar)	# Injections
Blue Diesel	0%	1500	2	480	Main+Pilot
Blue Diesel	40%	1500	2	480	Main+Pilot
Blue Diesel	50%	1500	2	800	Main
N-Heptane	0%	1500	2	480	Main+Pilot
N-Heptane	0%	1500	2	480	Main
N-Heptane	39%	1500	2	480	Main
N-Heptane	45%	1500	2	600	Main

6.3.2 Particle size, mass, gases and cycle-pressure measurements

With the dilution ratio kept constant at ~3.5, nanoparticle emissions were studied at different exhaust gas recirculation (EGR) levels and different injection conditions: main and main plus pilot injection. Pilot injection (sometimes also know as a pre-ignition) introduces a small quantity of fuel into the combustion chamber within a few ten-thousandths of a second prior to the main power-inducing explosion, resulting in a smoother combustion cycle, reduced knock and lower peak combustion temperature. Figure 6.8 illustrates this set of measurements for the example of the test engine run with commercial ultralow sulphur fuel (Blue Diesel). With the EGR off (red symbols), the measured size distribution was bimodal with the larger modal diameter at ~ 70nm and the smaller particle mode at 3-4nm, in good agreement with the results from LD diesel test vehicles 2&3 described in the previous paragraph except for the fact that the nucleation mode had a slightly smaller mean size. With the EGR level at ~ 40% (blue symbols), the smaller mode drastically decreased of about an order of magnitude (practically at the noise level) whereas the number concentration of the larger mode slightly increased. The last condition investigated (green symbols), when only the main injection was employed, revealed that, with a higher EGR (~ 50%) and the pressure rail at 800 bar (with respect to 480 bar in the other two conditions), the particle size distribution became mono-modal with mean geometric diameter at ~ 32 nm and showed a significant increase in the particle number concentration. The latter was a condition that resembled a premixed charge compression ignition (PCCI), an approach to achieve ultra-low emission combustion, which relies on changes in the injection time and high EGR rates to delay auto-ignition.

[4] Percentage of EGR refers to the EGR level

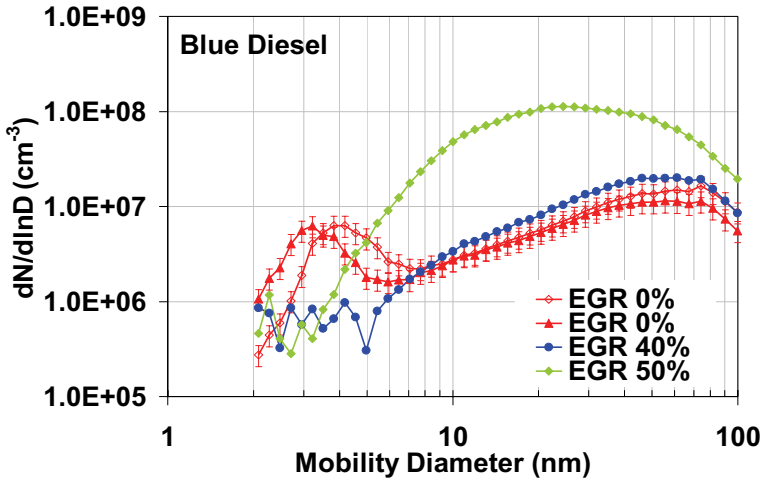

Figure 6.8 – Particle size distributions measured by DMA with three different EGR levels. Red filled symbols refer to data collected 90 minutes after those indicated with red empty symbols.

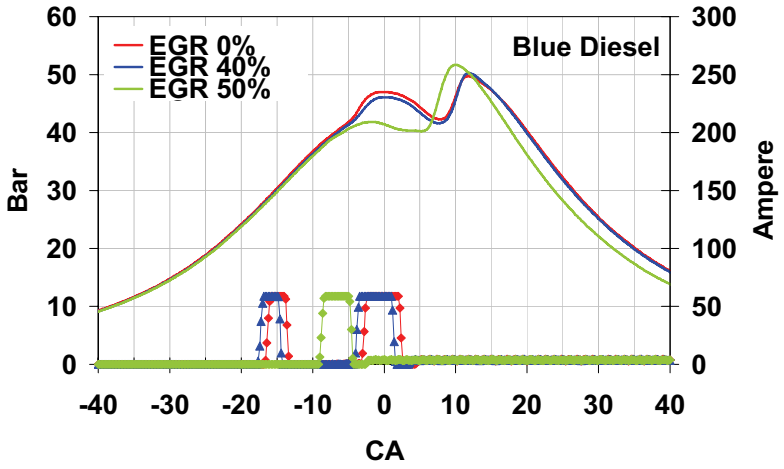

Figure 6.9 – Cycles of pressure (primary axis) and energizing current (secondary axis) corresponding to the three different EGR levels.

Figure 6.9 plots the cycles of pressure (primary axis, bar) and the energizing current (secondary axis, ampere) as function of the crank angle (CA) in correspondence of the three tested conditions. The energizing current refers to the current signal necessary to open the electro-injectors valve needle. The current signal is proportional to the injection time which is obviously slightly delayed compared to the input current. Both cycle of pressure and energizing current indicate the different operating conditions. For the first two

conditions investigated (EGR 0% and EGR 40%), it is possible to note the presence of the pilot injection (~ -15° of crank angle) prior to the main injection (~ 0° of crank angle) while the latter condition (EGR 50%) is characterized by the main injection, anticipated in time with respect to the other two. Also the Heat Release Rates (HRR) displayed in Figure 6.10 are a clear indication of the different combustion condition achieved for EGR 50% (green symbols).

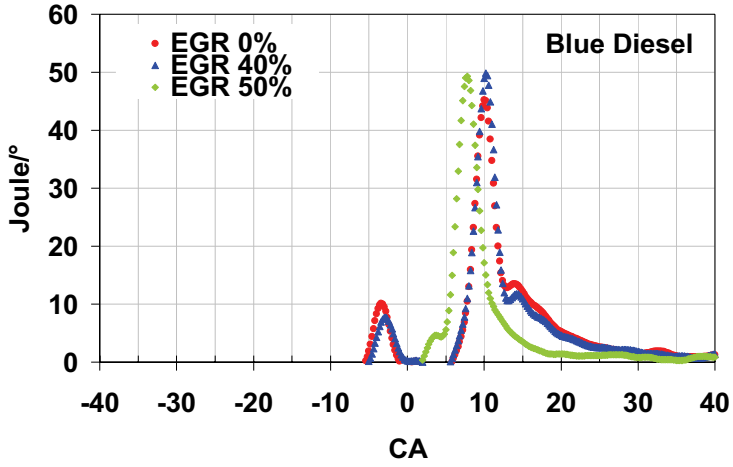

Figure 6.10 – Heat Release Rate (HRR) corresponding to the three different EGR levels.

Figure 6.11 compares the total mass concentration (Panel A) calculated from particle number size distributions of Figure 6.8 with the amount of hydrocarbons (HC) (Panel B), of oxides of nitrogen (NOx) (Panel C) and of carbon monoxide (CO) (Panel D) measured in the exhaust. HC concentration was measured with a so-called Flame Ionization Detector (AO 2020 Multi-Fid 14 Analyzer by ABB). NOx concentration was measured with a Model 955 NO/NO_x Analyzer (Beckman) while CO concentration was measured with a Model 880A Non-Dispersive Infrared Analyzer (Rosemount Analytical). The data reported in Panel A are calculated assuming an average particle density of 1.8 g/cm^3. This value was chosen since, with EGR 0% and EGR 40%, the larger mass-based fraction is made by a larger particle mode, likely soot. However, for EGR 50%, this value could be incorrect since the measured increase in the mass is likely due to hydrocarbons as testified by Panel B and therefore a lower value for the particle density (1.2 g/cm^3) would be more appropriate. The correlated increase in the particle and HC concentration, when changing EGR levels, seems to indicate that the additional mass measured with EGR at 50% was likely due to the condensation of semi-volatile matter on solid particles. At the same time it is interesting to note that the last operating condition (EGR 50%) effectively exhibited a positive effect on the amount of the oxides of nitrogen, producing a reduction of about 95% with respect to EGR 0%, but simultaneously produced a significant increase in the hydrocarbon and CO emissions.

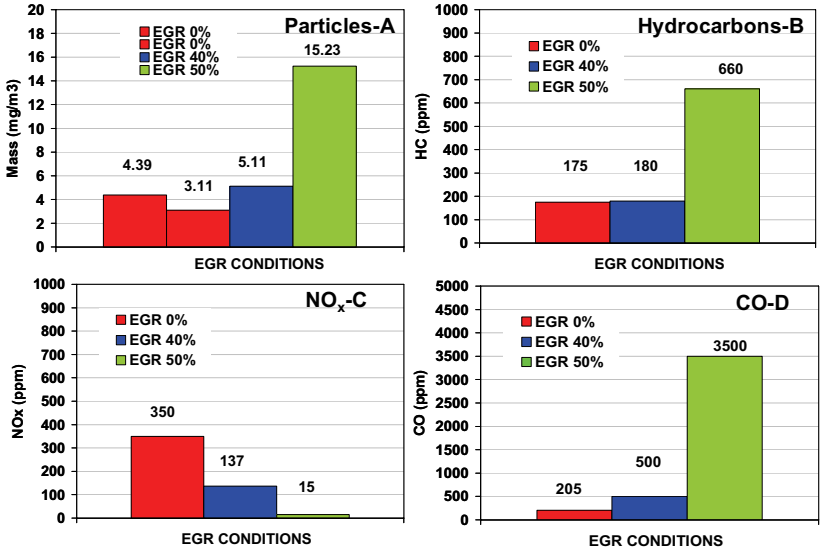

Figure 6.11 - Particle mass measured by the DMA (A), hydrocarbon concentration (B), nitrogen oxides (C) and carbon monoxide (D) in the different operating conditions.

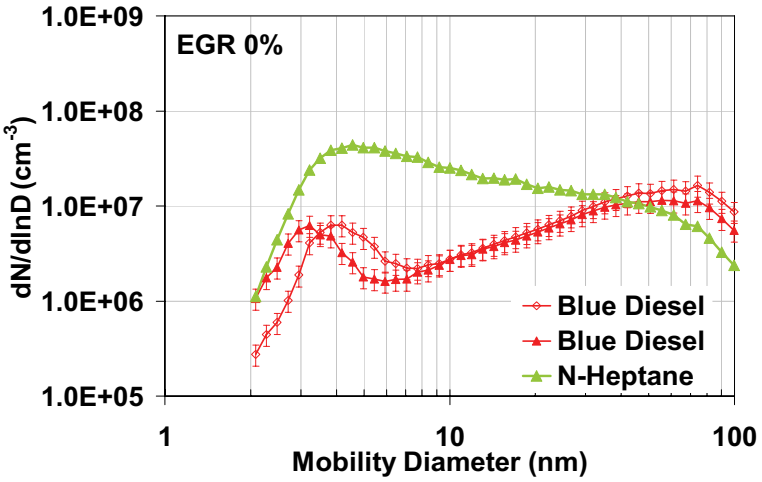

Figure 6.12 – Particle size distribution measured at EGR 0% with the engine running Blue Diesel (red symbols) and N-Heptane (green symbols).

The emissions from the single-cylinder engine were also tested when burning a different fuel, namely N-Heptane. Figure 6.12 displays the comparison of the measured size distribution when burning Blue Diesel (red symbols, identical to those displayed in Figure

6.8) and N-Heptane (green symbols), with the EGR off and the same operating conditions, namely 1500 rpm and pilot injection prior to the main injection. With the N-Heptane, the size distributions again exhibited two particle modes, even if the dip between the smaller mode (4-5 nm) and the larger mode (30-40 nm) was less evident and shifted toward larger sizes compared to the previous situation described for the Blue Diesel. The comparison in Figure 6.12 also reveals that, when burning N-Heptane, there was an increase in the emission for the nucleation particle mode and a lowering (and also a shift towards smaller sizes) of the larger mode.

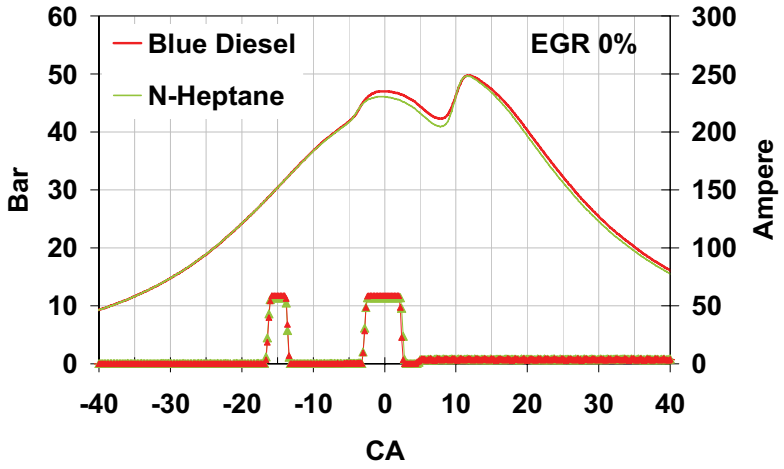

Figure 6.13 - Cycles of pressure (primary axis) and energizing current (secondary axis) corresponding to the engine running Blue Diesel (red line) and N-Heptane (green line). EGR at 0%.

The quantitative differences in the two examined cases are likely related to the fuel employed since the operating conditions were exactly the same: EGR off, speed 1500 rpm, Prail 480 bar, 2 injections, and dilution ratio ~ 3-4, also confirmed by equal cycles of pressure and energizing current (see Figure 6.13) and also Heat Release Rates (Figure 6.14).

Panel A of Figure 6.15 compares the mass concentration (mg/m^3) calculated from the measured size distributions and that measured by the smoke meter (415 S Variable Sampling Smoke Meter). Independently from the fuel employed, mass concentration calculated from size distributions is two times higher than that measured by the smoke meter. There are some explanations for the observed difference. First, as already pointed out, the absolute value of calculated mass depends on two important assumptions: particle density and particle roundness. The first has been chosen 1.8 g/cm^3, which is usually the value attributed to soot particles, but a smaller value of particle density (1.2 g/cm^3) would drop the mass concentration very close to the value measured by the smoke meter. Secondly there is no indication that larger size mode consists of spherical particles. As report by Baron *et al.* (2001), there are two common types of aggregate particles. The first type is a compact aggregate with an external shape similar to a sphere. The second type, also known as fractals, is represented by aggregate particles with an external shape highly non-spherical. In this calculation, the measured particles have been assumed to belong to the first category of ag-

gregate particles. At the same time, the operating principle of the smoke meter does not assure to measure all the particulate emitted. The measurement principle is based on the blackening of a filter paper, detected by an optical reflectometer head. Hence the non-graphitic carbon is missed. Finally, the smoke meter was positioned at the end of the exhaust line, namely ~3.5m downstream the sampling point for the differential mobility analysis, and the smoke meter measurement may suffer increased diffusional and thermophoretic losses with respect to the DMA measurement since the 3.5 line line was unheated.

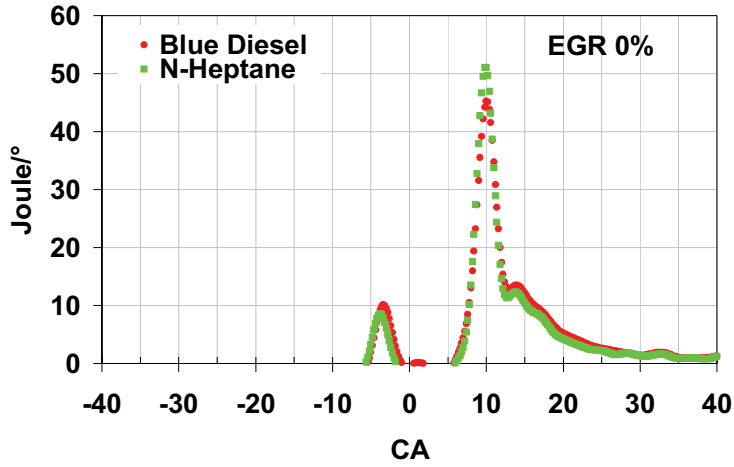

Figure 6.14 - Heat Release Rate (HRR) corresponding to the engine running Blue Diesel (red line) and N-Heptane (green line). EGR at 0%.

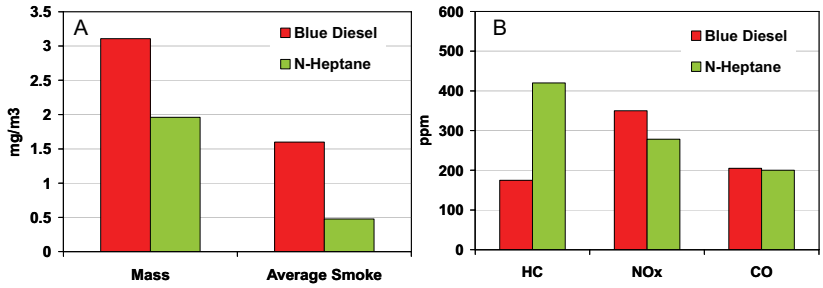

Figure 6.15 - Particle mass measured by the DMA and average smoke (Panel A); hydrocarbon concentration, nitrogen oxides and carbon monoxide (Panel B).

In any case, despite this discrepancy between the calculated and measured mass concentration, in the same operating conditions, the combustion of the Blue Diesel produced a higher particulate mass content with respect to the combustion of N-Heptane. Conversely the combustion of N-Heptane produced a higher (~ ten times) number particle emissions.

Panel B of Figure 6.15 displays the gases concentrations emitted when burning the two fuels. While there is practical no difference in the carbon monoxide emissions, trends for NO_x and HC are strongly dependent on the fuel employed. With respect to the Blue Diesel, the use of N-Heptane reduces of about 20% the NO_x emissions but produces an increase of about 140% for those of hydrocarbons.

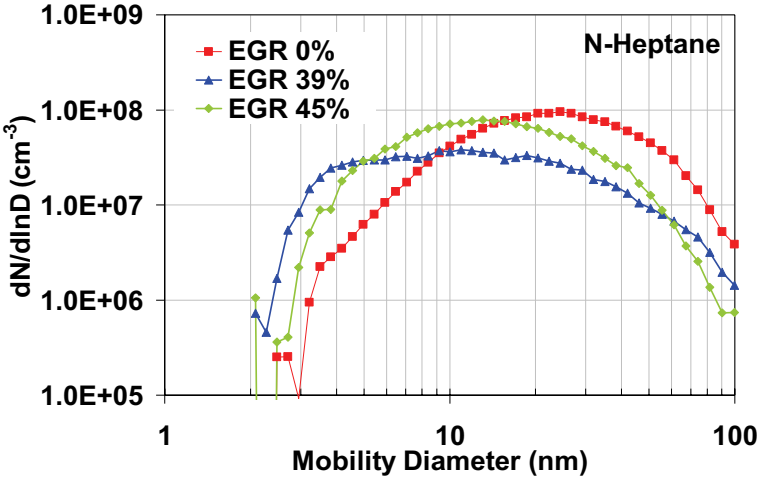

Figure 6.16 - Particle size distributions measured by DMA with three different EGR levels when the fuel is N-Heptane.

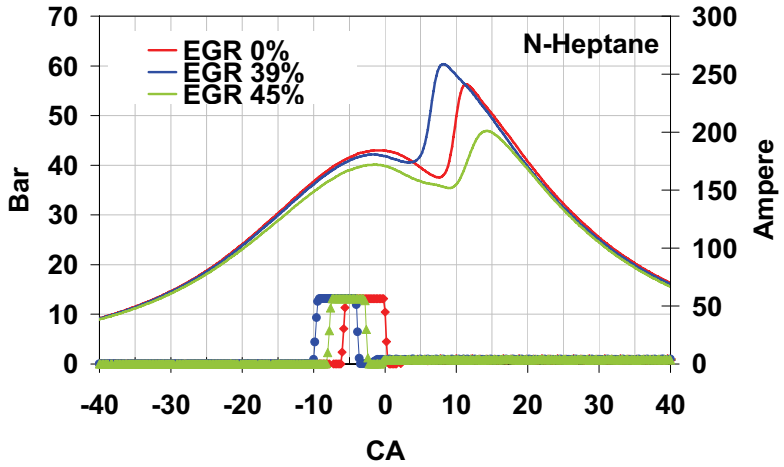

Figure 6.17 - Cycles of pressure (primary axis) and energizing current (secondary axis) corresponding to the three different EGR levels.

N-Heptane emissions have been also investigated operating with only the main injection at different EGR levels and different injection timing. In these conditions, the EGR

levels seemed to have a lower effect on the particle size distributions, since a broader distribution ranging from 3 to 100nm was always measured independently from the EGR level (see Figure 6.16). At a first sight, the main reason seems to be the different injection conditions employed which resembled that for EGR 50% in Figure 6.8 for the Blue Diesel. However, also the previous analyzed case for the N-Heptane, at EGR 0% and main plus pilot injection, did not show a clear bimodality (see green triangles in Figure 6.12). Thus the type of fuel employed, which produced a large amount of HC, may be the reason for the broad measured size distribution. A direct comparison at EGR 0% for the N-Heptane in the two different injection conditions is displayed in Figure 6.20 at the end of section 6.4.

Figure 6.17 displays the cycles of pressure (primary axis) and the energizing current (secondary axis) for this new set of measurements and Figure 6.18 shows the corresponding Heat Release Rates.

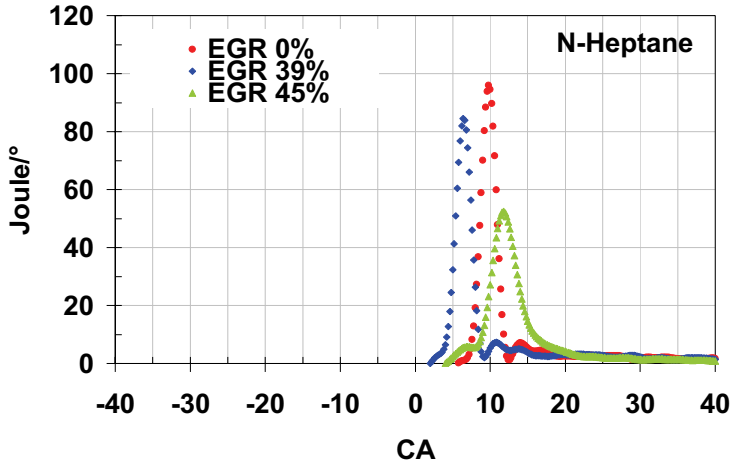

Figure 6.18 – Heat Release Rates corresponding to the three different EGR levels.

Figure 6.19 summarizes particle and gas concentrations at different EGR levels. The mass concentration calculated from the size distributions (again with particle density = 1.8 g/cm^3) and the soot mass measured from the smoke meter are compared in panel A, with those from the smoke meter displayed in light colors. In this case, the differences relative between the two masses are much larger than the one discussed in Figure 6.15. This may be explained by a higher content of semi-volatile matter condensed onto solid particles and, thus, measured by the differential mobility analyzer and not by the smoke meter. Similarly to the Blue Diesel, the last operating condition (EGR 45% and Prail 600 bar) strongly decreased the NO_x emissions (Panel C) but simultaneously increased the emissions of HC (Panel B) and carbon monoxide (Panel D). Therefore, the use of heated dilution (and higher dilution ratio) or a thermodenuder positioned along the sampling line before the EMS inlet might be able to clarify the contribution of semi-volatile material.

Further investigation on the particle size distributions emitted when the fuel is N-Heptane is still required and was not the aim of this thesis. Future goals are the analysis of particle size distributions at different loads, the investigation of particulate up to 1µm and

the use of a micro-soot analyzer for soot measurements at very low emission levels. In addition these measurements will constitute the experimental background for the development and validation of numerical modeling to simulate in cylinders particles formation during combustion processes in diesel engines. Preliminary attempts to simulate in cylinder particle formation during the combustion of N-Heptane have demonstrated a good agreement between experimental and numerical results (Fraioli, 2008).

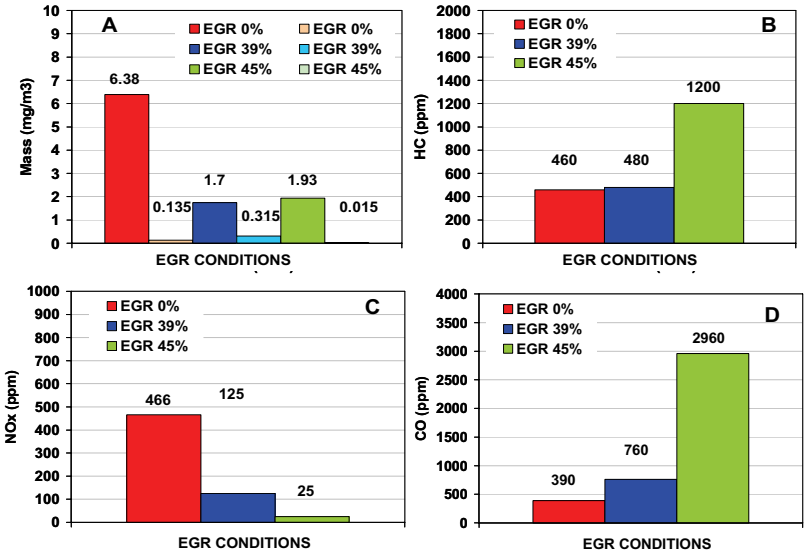

Figure 6.19 - Particle mass (A), hydrocarbon concentration (B), nitrogen oxides (C) and carbon monoxide (D) in the different operating conditions. Light colors in Panel A indicate the soot mass measured by the smoke meter.

6.4 General comments

The measurements of the emissions from two modern light-duty diesel vehicles run with commercial ultralow sulphur fuel showed the presence of two particle modes during different engine operative conditions of LD diesels 2&3: a smaller particle size mode (at ~ 8nm) and the soot mode (at ~ 60nm). The presence of the nuclei particles was found to be dependent on the EGR level and vehicle speed. With high level of the EGR and at higher speeds (40 and 70 mph), a nucleation mode was not evident. Without EGR and in idle condition (but also during low speed driving, 10 mph, see De Filippo & Maricq, 2008) measurements carried out on the LD diesel 2&3 revealed the presence of a nuclei mode with particular features that were in stark contrast with the traditional knowledge of the nucleation mode (Kittelson *et al*., 1996; Tobias *et al*., 2001; Shi & Harrison, 1999; Inoue *et al*., 2006; Kubo *et al*., 2006). First, these nuclei particles remained practically unchanged up to 450 C, similarly to the non-volatile cores observed by Kittelson *et al.* (2006) and Ronkko *et al.* (2007). Second, they exhibited electric charge, which indicates that they are origi-

nated in the combustion chamber, formed in high-temperature combustion processes and reactions, supporting the hypothesis by Sgro *et al*. (2008a). Third, they did not seem to be generated by semivolatile nucleation because the exhaust was sampled upstream of the DOC, the vehicles were run on ultra-low sulfur fuel (9-23 ppm) and hot dilution was employed. In addition, the analysis of how the after treatment devices affect these nuclei particles revealed that the Diesel Oxidation Catalyst (DOC) had practically no effect whereas the Diesel Particulate Filter significantly limited their release to the atmosphere with the same efficiency as the soot mode.

Measurements of the bench single-cylinder engine run with commercial ultralow sulfur fuel (Blue Diesel) confirmed the results from the two LD diesel vehicles. In this case, with the engine run at a constant speed and with EGR level 0%, the nucleation mode was found at slightly smaller sizes (~3-4 nm) with the soot mode again at ~ 60 nm. At higher EGR levels (39%), the smaller mode was not measured and a slightly increase of soot particle number was observed. Finally, in conditions that resembled a premixed charge compression ignition (PCCI), namely a single early injection time and high EGR rates, the nuclei particles were absent and a larger increase of the mass of the soot mode was observed. This increase was likely due to the condensation of semi-volatile matter on solid particles, namely hydrocarbons whose emissions were enhanced by the particular operating conditions. In addition, with EGR level at 0% and N-Heptane as the fuel, the size distributions again exhibited two particle modes even if the bimodality was not as clear as for the commercial fuel. In this case, with respect to the Blue Diesel case, the number concentration of the smaller mode (4-5 nm) was higher and that of the larger mode (30-40 nm) was smaller. The discrepancy is likely attributable to the different fuels employed and specifically to their evaporation rates of fuel droplets once injected into the combustion chamber which are related to the fuel composition.

Measurements with different injection conditions (and, specifically, only the main injection) on the N-Heptane produced a wider size distribution ranging from 3 to 100 nm. In this case the EGR level did not seem to affect the measured size distribution which was mostly affected by the type of fuel and by the premixed conditions generated into the combustion chamber, characterized by a higher production of HC. Figure 6.20 plots in the same graph the size distributions that have been already discussed for the N-Heptane when the level of EGR was kept at 0%. Whether the reason for the absence of a clear bimodality is the fuel or the operating conditions is still under investigation and requires further studies.

In general, these measurements represent also a powerful experimental background for the validation and the development of model to simulate in cylinders particles formation.

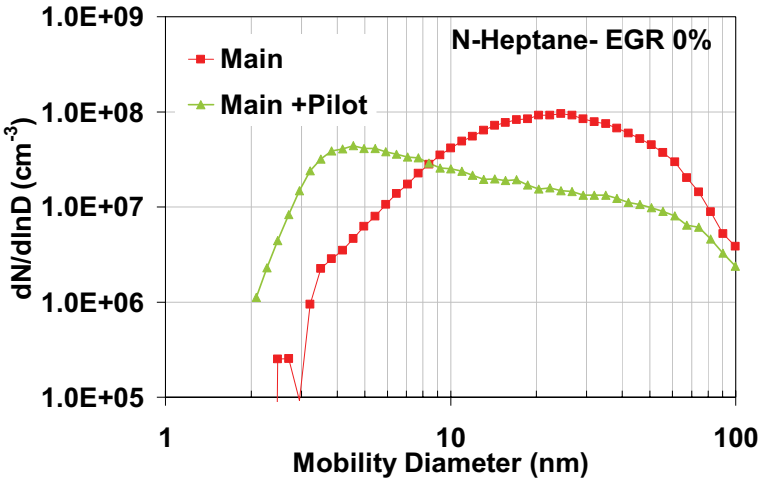

Figure 6.20 - Particle size distribution measured at EGR 0% with the engine running N-Heptane with a single injection (red symbols) and with a pre-injection (green symbols).

Seventh Chapter

Experimental results: domestic gas burner

7.1 Introduction

In the last few years, the research on indoor air pollution has received increased attention by the scientific community. As most people tend to spend more time indoors than outdoors, it becomes fundamental to evaluate the impact of indoor air pollution on human health, the extent to which humans are exposed to gases and particles, and identify the sources for indoor pollutants. The literature reports different campaigns measurements, carried out to evaluate indoor/outdoor relationship as well as personal exposure concentrations for selected volatile (Kotzias *et al.*, 2005) and non-volatile organic compounds in confined spaces such as homes, schools, public buildings (Kotzias *et al.*, 2005), kitchens (Kandpal *et al.*, 1995), residences (Li *et al.*, 2003), hospitals (Wang X. *et al*., 2006). Specifically different sources of pollutants such as evaporative coolers (Li *et al.*, 2003) and domestic cook stoves (Kandpal *et al*, 1995) were investigated.

The purpose of this chapter is to present preliminary size distributions measurements from domestic cooking gas burners fuelled with methane. The investigated burners were representative of domestic cooking appliances, mainly used in the early '90s but still largely employed by the lower class population living in the urban areas, the population living in the rural areas and by campers. Detailed chemical analysis of the measured nanoparticles will be a subject of future works.

7.2 Domestic gas burner

7.2.1 Experimental procedure

The experiments were carried out in a laboratory (3.5 x 4 x 3 m) at Dipartimento di Ingegneria Chimica - Università di Napoli "Federico II". Throughout the experiments, no arrangement for ventilation was provided. The burner (CF PARKER 5327 M) was fuelled with methane characterized by high purity level (IP 3.5). The methane flow rate, controlled by a rotameter, was varied in the flow range 2.25 - 9 L/min. Once the burner was ignited, the resulting flames were generally blue colored (see Figure 7.1) and the changes in the fuel flow rate simply produced a slight change in the flame's shape.

The monitoring of nanoparticle size distributions was carried out with the tapcon EMS DMA 3/150 (described in Chapter 2) at different heights from the stainless steel grid covering the burner. The size range 0.6-28nm was investigated. Two different sets of measurements were made. In one case, the undiluted sample was convoyed to the analyzer through a funnel (oval A in Figure 7.1), vertically positioned above the burner and connected to the tapcon inlet with a 35 cm long stainless steel tube (with a bend of 90 °). In a second case, the funnel was replaced by a home-made ejector which provided a dilution ratio of 25:1 (oval B & C in Figure 7.1). In both cases, tests were repeated 3 to 5 times to assure repeatability.

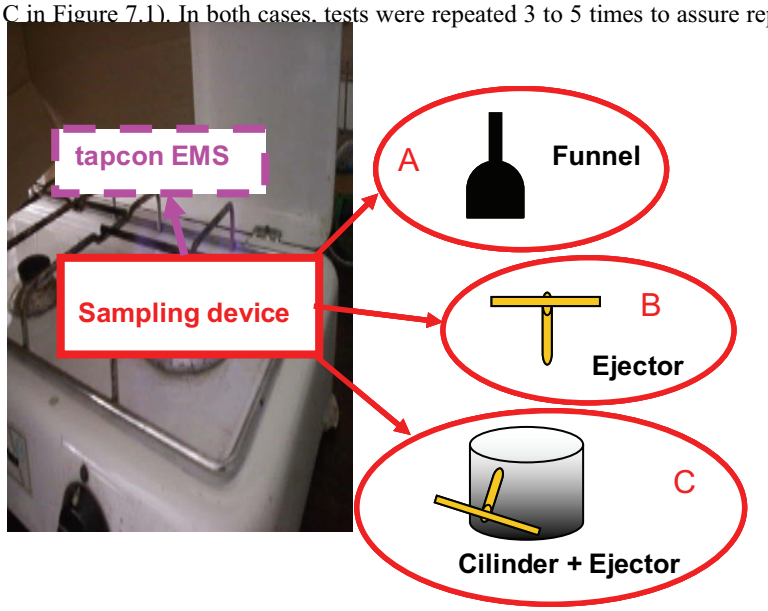

Figure 7.1 – Investigated burner fuelled with methane and schematic view of the different sampling devices adopted.

7.2.2 Nanoparticles naturally convoyed to the analyzer (no dilution employed)

Figure 7.2 shows the size distributions when no dilution devices were used. The sample was directly convoyed to the analyzer through a funnel, vertically positioned at H = 6mm above the grid. The burner was fuelled with methane flow respectively set at 2.25 L/min (filled black symbols) and 6.75 L/min (empty black symbols). The flame was not particularly stable and the three different runs at 2.25 L/m indicate the reliability in time. These measurements, employing the tapcon EMS as analyzer, are compared with size distributions relative to the laboratory air (blue symbols), at ambient conditions before burning any flames, and with the size distributions measured in a previous campaign on the same burner with a TSI SMPS 3936 (red symbols) (Minutolo *et al*, 2007). In the latter, Minutolo *et al.* did not use a dilution system, testing the particulate emitted in the exhaust, using the funnel to convey the aerosol to the analyzer. The measured nanoparticles were in the size range 3-7 nm with an overall number concentration of about 10^8 particles/cm^3.

A first observation is that, in the size range above 3 nm, there is a fairly good agreement between the two campaigns of measurements (signals below 10^6 were close to noise level). As previously discussed in Chapter 2, the tapcon EMS is also able to investigate the size range below 3 nm. Therefore it consented to reveal the lower side of the nanoparticle mode measured in the previous campaign. The 2nm peak measured in the premixed flames was not clearly visible. The dip between the sub-nanometer peak and the 2nm peak was only marginally visible, the latter appearing as a shoulder from the first which was larger than usually measured. The comparison with the signal measured from the air in the laboratory (blue symbols) before burning any flames, helps to discern whether or not the measured signal below 3 nm depended on the flame. The differences among blue and black curves are clear. The signal referred as 'Room Air' has a modal diameter at 0.85nm, with the tail dropping at about 2nm. The signal in the size range 2-5nm, below 10^6, is noisy and is an effect of the equation included in the software to account for the charging efficiency (Wiedensohler *et al.*, 1998).

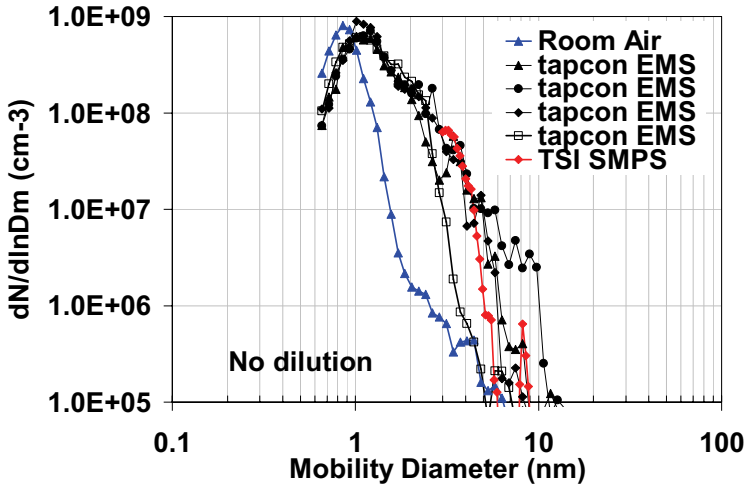

Figure 7.2 – Size distributions with methane flow set at 2.25 L/min (black squares) and 6.75 L/min (black triangles), with the sampling point at H = 6 mm above the grid.

Therefore, even if it is still not possible to completely identify the smallest particles emitted from the flames, it appears reasonable to conclude that there was also some material coming out from the flame in the size range 1-3 nm. The result is also in agreement with optical absorption measurements and time resolved fluorescence polarization anisotropy (TRFPA) analysis on water samples from the same flames (Minutolo *et al.*, 2006). In any case, a detailed chemical analysis and also a campaign to investigate the charge of the measured particle would help to attribute the origin of the signal in a more definitive way. These analyses were left for future works.

Furthermore, analyses at H=20 cm and at H=45 cm did not produce any changes in the measured size distributions, with the methane flow fixed at 2.25 L/min.

7.2.3 Nanoparticles sampled through a home-made ejector (dilution employed)

Figure 7.3 displays the size distributions measured with the home-made ejector vertically positioned above the burner surface at H=32 mm above the grid. The data from the flames are not corrected for the dilution employed (25:1) in order to compare with the curve measured when sampling ambient air before lighting the flame (blue curve).

Differently from data displayed in Figure 7.2, the size distributions showed additional material above 10nm, except when fuelling the burner with the methane set at 2.25 L/min (green symbols). In the size range above 5 nm, the repeatability was not very high (error bar 40%) but it was clear that the total volume fraction of the measured particle increased with increasing the methane flow. Specifically this increase preferentially involved the larger particles (d≥ 3nm). While the interpretation of the signals below 3 nm reflects the observations given for the previous case, it is very hard to attribute the origin of the larger particle mode without any other analysis (e.g. temperature) of the flames in the various conditions (but always blue colored) and also with the tapcon EMS set to investigate a larger size range.

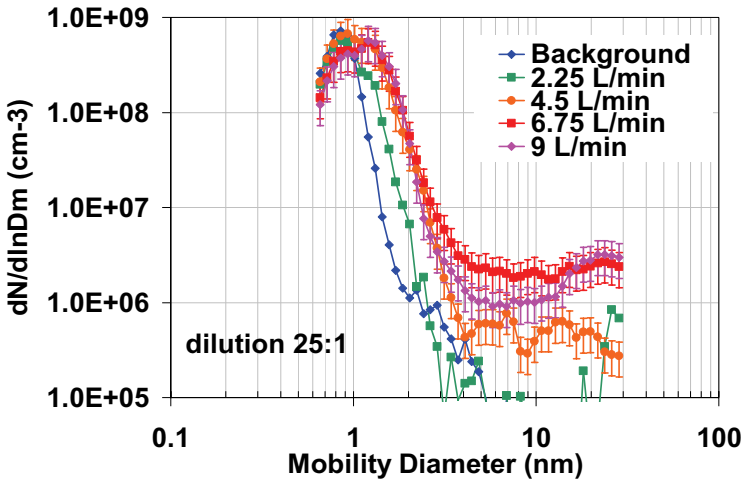

Figure 7.3 - Size distributions with methane flow set at 2.25 L/min (green symbols), 4.5 L/min (orange symbols), 6.75 L/min (red symbols) and 9 L/min (violet symbols) with the sampling point at H = 32 mm above the grid. Blue symbols refer to the signal of diluting nitrogen plus air sampled from the room before the ignition of the flame.

A possibility is that, in the experiment with the funnel, larger particles are lost somewhere during the transport from the sampling point to the inlet of the analyzer since no dilution was used. To note that the distance from the sampling point to the analyzer was ~ 150cm with the first 60 cm characterized by a 90° bend and the other remaining 90 cm as a straight line to the analyzer. In the experiment with the ejector the dilution (and also a shorter straight transport line, ~90 cm) likely reduced particle losses.

In a second set of measurements, a stainless steel cylinder (706.5 cm^2 x 33cm) was placed above the grid to reduce the perturbation of the flame. A small hole was drilled into

the wall of the cylinder to allow the ejector to horizontally sampling at H = 23 cm above the grid. The dilution ratio was kept fixed at 3.55 and the flames were studied at different methane flow rates. Figure 7.4 displays the corresponding measurements.

The presence of the cylinder favored a higher stability of the flame, and as a consequence a higher repeatability in the measured size distributions. Again a larger size particle mode was detected at about 10 nm, similarly to the previous data (see Figure 7.3). The increase of the volume fraction with increasing the methane flow was slightly lower than in the previous set of data.

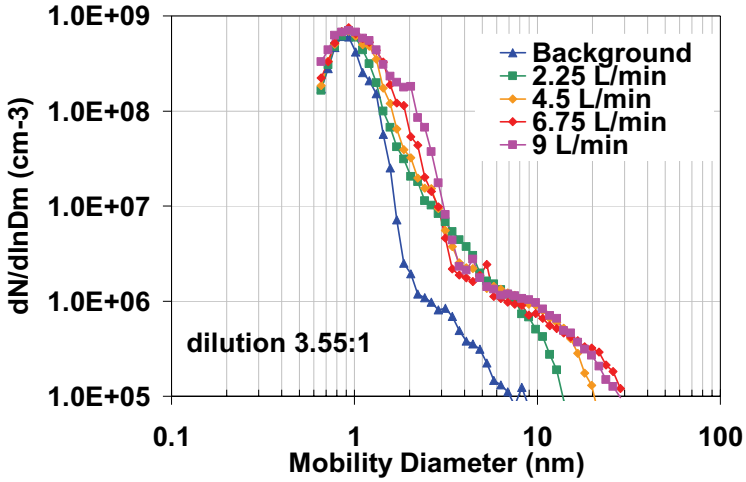

Figure 7.4 - *Size distributions with methane flow set at 2.25 L/min (green symbols), 4.5 L/min (orange symbols), 6.75 L/min (red symbols) and 9 L/min (violet symbols) with the sampling point at H = 23 mm above the grid. Blue symbols refer to the signal of diluting nitrogen plus air sampled from the room before the ignition of the flame. The flame is shielded by a stainless steel cylinder.*

In general, this preliminary investigation demonstrated the presence of nano-sized material in proximity of domestic cooking gas burner fuelled with methane. The nature of the signal requires further investigation. In 2006, Minutolo *et al*. collected the exhaust from the same burner, fuelled with methane, in water samples which were subsequently analyzed with Time Resolved Fluorescence Polarization Anisotropy (TRFPA) (Minutolo *et al*., 2006). The water collected material, after the partial evaporation of the sample at low pressure (10mbar), showed the same spectroscopic characteristics which can be assigned to small PAH and NOC particles with an estimated mean particle size of 1.9nm ± 0.1. A signal at ~2nm is also visible in this campaign of on-line measurements with a differential mobility analyzer.

As a future goal, it will be relevant to study also the particle size distributions emitted by this burner fuelled with natural gas (which is normally adopted in public buildings) and to evaluate the particle concentration in different realistic conditions: different distances from the combustion source and with ventilation.

7.3 Final comments

The levels of emissions from the common burner investigated in this thesis are very low (~10^6 particles/cm^3) and these would not represent a significant air quality issue within houses in developed countries. However, the situation would be slightly different in third world countries where the cooking methods are much less efficient that those used in the developed countries and are based on less clean combustion sources such as biomass. Therefore, in addition to the studies on $PM_{2.5}$ and PM_{10} (Li W.W. *et al*., 2003) and gaseous pollutants (Kandpal *et al*., 1995), it would be also interesting and advisable to perform campaigns of measurements with the differential mobility analyzer to determine the particle number concentration (and the size range) emitted from these specific combustion sources in order to assess their impact on human health and air indoor/outdoor pollution.

Conclusions

In this thesis, commercially available Scanning Mobility Particle Sizer (SMPS) and Electrical Mobility Spectrometer (EMS), both based on the differential mobility analysis (DMA), were used to provide further, and new, information about nanoparticles emitted from premixed flames, engines and common burners, with particular attention to the 1-10 nm range.

Employing an on-line differential mobility analyzer, this work showed clearly for the first time the presence of two modes of nanoparticles formed in premixed flames below the on-set of soot formation, the latter defined on the basis of previous work employing optical techniques. In flames burning ethylene and methane, the first modal diameter of the smaller mode (Mode I) was measured to be about ~ 2nm and showed features in good agreement with that of NOC particles found in earlier works by D'Alessio and his co-workers (D'Alessio *et al.*, 2007). On the other hand, the modal diameter of the larger (Mode II) shifted between 3 and 7 nm, depending on the specific combustion conditions, and its growth processes seemed to be slightly different from those of Mode I, opening the question about the chemical nature of Mode II (NOC or already soot particles?) whose analysis is left for future study. In terms of size distributions, these results were in excellent agreement with simultaneous, and independent, measurements employing Photo Ionization Mass Spectrometry (PIMS) on similar flames (Gonzales Baquet *et al*., 2007).

Furthermore, the first smaller mode was found to be electrically charged. Measurements of charged and neutral particles in Mode I presented in this thesis showed that the 2nm peak was definitely flame-generated with no interfering sign from ion-induced molecular clusters formed in the particle charger. Although this observation was not surprising because many other measurements based on other techniques (AFM, optical diagnostics, PIMS, FTRPA) also found a ~2nm peak for flame-generated nanoparticles in similar premixed flames, the DMA measurements gave the highest resolution size distributions determined for flame generated incipient nanoparticles to date except for PIMS. However, since PIMS measurements are not yet calibrated in terms of ion abundance, they give less quantitatively definitive distributions than those presented in this thesis. It is worth noting, however, that in flame conditions that produced unimodal size distributions containing only Mode I nanoparticles, DMA measured significantly less particles compared to *in situ* optical and atomic force microscopy (AFM) measurements. Future work is needed to determine the reason for this quantitative discrepancy in order to have reliable information on nanoparticles in these conditions.

In several burning conditions (different cold gas velocities, different fuels, different heights above the burner) flame-generated nanoparticles were found to be present in low mass concentration, but high number concentrations (10^{11}-10^{12} particles/cm^3). The investigation of laboratory flames also indicated that particle inception occurs early in the flame in non-sooting flames, in agreement with the conceptual framework for particle inception advanced in earlier works based on UV-visible measurements (D'Alessio *et al*., 1998; Minutolo *et al.*, 1999). Furthermore, the analysis limited to a flame with C/O=0.65, considered to be below the on-set of soot formation on the basis of optical measurements which found no signs of soot, indicated that, in high temperature flame environments, the coagulation rate is size dependent. This result again confirmed previous studies employing other diagnostics (D'Alessio *et al.,* 2005). The coagulation model assuming size dependent co-

agulation efficiency, γ_{SD}, was able to reproduce better than the model with $\gamma = 1$ the experimental results for the entire range of heights investigated even if it under predicted the quantity of material measured in Mode II late in the flame.

The low coagulation rate of nanoparticles indicated that some of them may survive for a long enough time to survive exhaust manifolds and thus be emitted into the atmosphere without significant growth. Based on the size, properties and nature of combustion-formed nanoparticles learned from laboratory flames, subsequent tests on diesel vehicles and test bench engines were made to examine the particle size distribution at the exhaust of a "real" system. Both vehicles and engine were representative of modern systems and were run with commercial ultralow sulphur fuel.

Without EGR and in idle conditions (and also low speed), the DMA measurements on the exhaust of two diesel vehicles indicated the presence of a particle nucleation mode (~ 8nm) which accompanied normal soot emissions (~ 60 nm). This nuclei mode presented particular features that were in stark contrast with the traditional knowledge of the nucleation mode previously measured in vehicle exhausts. First, these nuclei particles remained practically unchanged up to 450 C, which was a first indication of his "solid" nature. Second, they exhibited electric charge, which indicates that they are originated in the combustion chamber, formed in high-temperature combustion processes and reactions, and not by low-temperature condensation processes as the exhaust cools. Third, they did not seem to be generated by semi-volatile nucleation because the exhaust was sampled upstream of the DOC, the vehicles were run on ultra-low sulfur fuel (9-23 ppm) and hot dilution was employed. In addition, the analysis of how the after treatment devices affect these nuclei particles revealed that the Diesel Oxidation Catalyst (DOC) had practically no effect (another confirmation of their nonvolatile nature) whereas the Diesel Particulate Filter significantly limited their release to the atmosphere with the same efficiency as the soot mode. At the same time, the presence of a smaller mode at about 3 to 5nm was also measured at the exhaust of the single-cylinder test bench when run with ultralow sulphur commercial fuel. This mode was strongly dependent on the EGR levels and operating conditions.

In general, the two campaigns of measurements made in different research laboratories (and with different analysis systems) indicated the contemporary presence of two nonvolatile particles modes, with the smaller exhibiting different behaviors and characteristics from the larger one. The origin of these two modes of nonvolatile particles is currently not known. The fact that they are non-volatile indicates that they are not produced by evaporated then condensed lubrification oil. One hypothesis, based on this work, is that the smaller mode are flame-generated NOC, produced into the engine, that grew slightly in the exhaust manifold or sampling line before being measured. Continued advances in diagnostic techniques can help disclose their chemical characteristics, necessary to identify their original nature.

Additionally, size distributions measurements on the single-cylinder engine when run with N-Heptane and, in conditions that resembled a premixed charge compression ignition (PCCI), namely a single early injection time and high EGR rates, showed the absence of nuclei particles and an increase in the soot mode was observed. Contemporaneous analysis of gas exhaust revealed that these operating conditions strongly decreased the NO_x emissions (as expected and, in agreement, with the actual regulations) but simultaneously increased the emissions of HC and carbon monoxide.

Preliminary measurements on domestic gas appliances fuelled with methane also showed the presence of material coming out from the flame in the size range 1-3, in agreement with optical absorption measurements and time resolved fluorescence polarization anisotropy (TRFPA) analysis on water samples from the same flames (Minutolo *et al*., 2006). Detailed chemical analysis of the measured nanoparticles will be a subject of future works.

In general, this thesis remarks the importance of the differential mobility analysis (DMA) as a powerful experimental tool in the study of nanoparticle formation in different combustion sources, with particular attention to the dynamics of the very small nanoparticles (1-10 nm), and as an important experimental background for the development and validation of numerical modeling to simulate particles formation during combustion processes.

Bibliography

ADACHI, M., OKUYAMA, K., KOUSAKA, Y., *Electrical Neutralization of Charged Aerosol Particles by Bipolar Ions,* Journal of Chemical Engineering Japan 16 (1983) 229-235.

ALLEN, M.D., RAABE, O.G., *Slip Correction Measurements of Spherical Solid Aerosol Particles in an Improved Millikan Apparatus,* Aerosol Science and Technology 4 (1985) 269-286.

ALONSO, M., KOUSAKA, Y., HASHIMOTO, T., HASHIMOTO, N., *Penetration of Nanometer-Sized Aerosol Particles Through Wire Screen and Laminar Flow Tube*, Aerosol Science and Technology 27 (1997a) 471-480.

ALONSO, M., KOUSAKA, Y., NOMURA, T., HASHIMOTO, N., HASHIMOTO, T., *Bipolar charging and neutralization of nanometer-sized aerosol particles*, Journal of Aerosol Science 28 (1997b) 1479-1490.

APICELLA, B., CARPENTIERI, A., ALFE', M., BARBELLA, R., TREGROSSI, A., PUCCI, P., CIAJOLO, A., *Mass spectrometric analysis of large PAH in a fuel-rich ethylene flame*, Proceedings of the Combustion Institute 31 (2007) 547-553.

APICELLA, B., BARBELLA, R., CIAJOLO, A., TREGROSSI, A., *Comparative analysis of the structure of carbon materials relevant in combustion*, Chemosphere 51 (2003) 1063-1069.

AIR QUALITY MANAGEMENT DISTRICT (AQMD), *ULTRAFINE PARTICLES—The Science, Technology and Policy Issues*, Conference held in 2006, Los Angeles, United States. HTTP:// www.amqd.gov/TAO/UltrafineParticleConf.htlm

AVOLIO, G., BEATRICE, C., BERTOLI, C., *Development of a Single Cylinder Direct Injection Diesel Engine for advanced combustion system studies*, High-Tech Cars and Engines (2005) Modena, Italy.

BACHMANN, M., WIESE, W., HOMANN, K-H., *PAH and aromers: precursors of fullerenes and soot*, Proceedings of the Combustion Institute 26 (1996) 2259-2267.

BARLOW, R.S., CARTER, C.D., *Raman/Rayleigh/LIF measurements of nitric oxide formation I turbulent hydrogen jet flames,* Combustion and Flame 97 (1994) 261-280.

BARON, P.A., SORENSEN, C.M., BROCKMANN, J.E., *Nonspherical Particle Measurements: Shape Factors, Fractals, and Fibers,* in Aerosol Measurement: Principles, Techniques, And Applications, Ed by Baron, P.A., and Willeke, K., (2001) 705-749, John Wiley & Sons, New York (USA).

BARONE, A.C., D'ALESSIO, A., D'ANNA, A., *Morphological characterization of the early process of soot formation by atomic force microscopy*, Combustion and Flame 132 (2003) 181-187.

BASILE, G., ROLANDO, A., D'ALESSIO, A., D'ANNA, A., MINUTOLO, P., *Coagulation and carbonization processes in slightly sooting premixed flames*, Proceedings of the Combustion Institute 29 (2002) 2391-2397.

BOCKHORN, H., *A Short Introduction to the Problem-Structure of the Following Parts,* in Soot Formation in Combustion: Mechanisms and Models, Ed by Bockhorn, H., (1994) 3-7, Springer-Verlag, Heidelberg.

BRUNO, A., DE LISIO, C., MINUTOLO, P., D'ALESSIO, A., *Evidence of fluorescent carbon nanoparticles produced in premixed flames by time-resolved fluorescence polarization anisotropy*, Combustion and Flame 151 (2007) 472-481.

BRUNO, A., OSSLER, F., DE LISIO, C., MINUTOLO, P., SPINELLI, N., D'ALESSIO, A., *Detection of fluorescent nanoparticles in flame with femtosecond laser-induced fluorescence anisotropy*, Optics Express 16 (2008) 5623-5632.

BURTSCHER, H., *Physical characterization of particulate emissions from diesel engines: a review*, Journal of Aerosol Science 36 (2005) 896-932.

BURTSCHER, H., MATTER, D., SIEGMANN, H.C., *Measurement of size distribution and photoelectric activity of particles in a gas diffusion flame*, Atmospheric Environment 27A (1993) 1255-1259.

CADLE, S.H., MULAWA, P., HUNSANGER, E.C., NELSON, K., RAGAZZI, R.A., BARRETT, R., GALLAGHER, G.L., LAWSON, D.R., KNAPP, K.T., SNOW, R., *Measurement of Exhaust Particulate Matter Emissions from In-Use Light-Duty Motor Vehicles in the Denver, Colorado Area*, Coordinating Research Council Project E-24-1 Final Report, CRC, Atlanta, GA, (1998) 142.

CASTALDI, M.J., MARINOV, N.M., MELIUS, C.F., HUANG, J., SENKAN, S.M., PITZ, W.J., WESTBROOK, C.K., *Experimental and modeling investigation of aromatic and polycyclic aromatic hydrocarbon formation in a premixed ethylene flame,* Proceedings of the Combustion Institute 26 (1996) 693-702.

CHESKIS, S., *Quantitative measurements of absolute concentrations of intermediate species in flames,* Progress in Energy and Combustion Science 25 (1999) 233-252.

CIAJOLO, A., BARBELLA, R., TREGROSSI, A., BONFANTI, L., *Spectroscopic and compositional signatures of PAH-loaded mixtures in the soot inception region of a premixed flame,* Proceedings of the Combustion Institute 27 (1998) 1481-1487.

CIAJOLO, A., D'ANNA, A., BARBELLA, R., TREGROSSI, A., VIOLI, A., *The effect of temperature on soot inception in premixed ethylene flames,* Proceedings of the Combustion Institute 26 (1996) 2327-2333.

CIAJOLO, A., D'ANNA, A., BARBELLA, R., *PAH and High Molecular Weight Species Formed in a Premixed Methane Flame,* Combustion Science Technology 100 (1994) 271-281.

CLAUSS, W., FABELINSKY, V.I., KOZLOV, D.N., SMIRNOV, V.V., STELMAKH, O.M., VERESCHAGIN, K.A., *Dual-broadband CARS temperature measurements in hydrogen-oxygen atmospheric pressure flames,* Applied Physics B 70 (2000) 127-131.

COLKET, M.B., SEERY, D.J., *Reaction mechanisms for toluene pyrolysis*, Proceedings of the Combustion Institute 25 (1994) 883-891.

D'ALESSIO, A., D'ANNA, A., MINUTOLO, P., SGRO, L.A., *Nanoparticles of Organic Carbon (NOC) formed in flames and their effects in urban atmospheres*, in Combustion Generated Fine Carbonaceous Particles, Ed by Bockhorn, H., D'Anna, A., Sarofim, A.F., Wang, H., (2007) 201-227.

D'ALESSIO, A., BARONE, A.C., CAU, R., D'ANNA, A., MINUTOLO, P., *Surface deposition and coagulation efficiency of combustion generated nanoparticles in the size range from 1 to 10 nm*, Proceedings of the Combustion Institute 30 (2005) 2595-2603.

D'ALESSIO, A., D'ANNA, A., MINUTOLO, P., SGRO, L.A., VIOLI, A., *On the relevance of surface growth in soot formation in premixed flames*, Proceedings of the Combustion Institute 28 (2000) 2547-2554.

D'ALESSIO, A., D'ANNA, A., GAMBI, G., MINUTOLO, P., *The spectroscopic characterization of UV absorbing nanoparticles in fuel rich soot forming flames*, Journal of Aerosol Science 29, 4 (1998) 397-409.

D'ALESSIO, A., D'ANNA, A., D'ORSI, A., MINUTOLO, P., BARBELLA, R., CIAJOLO, A., *Precursor Formation and Soot Inception in Premixed Ethylene Flames*, Proceedings of the Combustion Institute 24 (1992) 973-980.

D'ANNA, A., COMMODO, M., SIRIGNANO, M., MINUTOLO, P., PAGLIARA, R., *Particle Formation in Opposed-Flow Diffusion Flames of Ethylene: an Experimental and Numerical Study,* accepted for publication on Proceedings of the Combustion Institute 32 (2008).

D'ANNA, A., *Particle inception and growth: experimental evidences and a modeling attempt*, in Combustion Generated Fine Carbonaceous Particles, Ed. by Bockhorn, H., D'Anna, A., Sarofim, A.F., Wang, H., (2007) 287-317.

D'ANNA, A., COMMODO, M., VIOLI, S., ALLOUIS, C., KENT, J., *Nano organic carbon and soot in turbulent non-premixed ethylene flames,* Proceedings of the Combustion Institute 31 (2007) 621-629.

D'ANNA, A., ROLANDO, A., ALLOUIS, C., MINUTOLO, P., D'ALESSIO, A., *Nano-organic carbon and soot particle measurements in a laminar ethylene diffusion flame,* Proceedings of the Combustion Institute 30 (2005) 1449-1456.

D'ANNA, A., VIOLI, A., D'ALESSIO, A., SAROFIM, A.F., *A Reaction Pathway for Nanoparticle Formation in Rich Premixed Flames,* Combustion and Flame 127 (2001) 1995-2003.

D'ANNA, A., D'ALESSIO, A., MINUTOLO, P., *Spectroscopic and Chemical Characterization of Soot Inception Processes in Premixed Laminar Flames at Atmospheric Pressure,* in Soot Formation in Combustion: Mechanisms and Models, Ed by Bockhorn, H., (1994) 83-103, Springer-Verlag, Heidelberg.

DE FILIPPO, A., MARICQ, M.M., *Diesel nucleation mode particles: Semivolatile or solid*?, Environmental Science Technology 42 (2008) 7957-7962.

DE FILIPPO, A., COMMODO, M., MINUTOLO, P., SGRO, L.A., *The Evolution Of Nanoparticle Size Distributions and UV-visible Extinction and Fluorescence in Premixed Ethylene Air Flames*, paper A325, 3rd European Meeting on Combustion (2007) Chanìa, Greece.

DE FILIPPO, A., SGRO, L.A., D'ALESSIO, A., *Sampling and analysis system to collect and measure nanoparticle size distribution produced in ethylene-air flame,* 29th Meeting on Combustion Italian Section of the Combustion Institute (2006) Pisa, Italy.

DEKATI LTD. – OSUUSMYLLYNKATU 13, FIN 33700 TAMPERE, FINLAND

DOBBINS, R.A., *Hydrocarbon Nanoparticles Formed in Flames and Diesel Engines,* Aerosol Science and Technology 41 (2007) 485-496.

DOBBINS, R.A., SUBRAMANIASIVAM, H., *Soot Precursor Particles in Flames,* in Soot Formation in Combustion: Mechanisms and Models, Ed by Bockhorn, H., (1994) 290-301, Springer-Verlag, Heidelberg.

DOBBINS, R.A., MEGARIDIS, C.M., *Morphology of Flame-Generated Soot as Determined by Thermophoretic Sampling,* Langmuir 3 (1987) 254-259.

DONALDSON, K., LI, X.Y., MACNEE, W., *Ultrafine (Nanometre) particle mediated lung injury,* Journal of Aerosol Science 29 (1998) 553-560.

EURO 5/6 STANDARDS (2009/2014), *Regulation (EC) No 715/2007 of the European Parliament and The Council*, Official Journal of the European Union L 171 (2007).

FERNANDEZ DE LA MORA, J.J., DE JUAN, L.L., LIEDTKE, K., SCHMIDT-OTT, A., *Mass and size determination of nanometer particles by means of mobility analysis and focused impaction*, Journal of Aerosol Science 34 (2003) 79-98.

FLAGAN, R.C., *History of Electrical Aerosol Measurements,* Aerosol Science and Technology 28 (1998) 301-380.

FRAIOLI, V., *Autoignition and particles formation in diesel engines: modeling and experiments,* Ph. D Thesis (2008) in press.

FRENKLACH, M., WANG, H., *Detailed Mechanism and Modeling of Soot Particle Formation,* in Soot Formation in Combustion: Mechanisms and Models, Ed by Bockhorn, H., (1994) 165-192, Springer-Verlag, Heidelberg.

FRENKLACH, M., WANG, H., *Detailed Modeling of Soot Particle Nucleation and Growth*, Proceedings of the Combustion Institute 23 (1991) 1559-1566.

FRIEDLANDER, S.K., *Smoke, dust, and haze: fundamentals of aerosol behaviour*, (1977) John Wiley & Sons, New York (USA).

FUCHS, N.A., *On the stationary charge distribution on aerosol particles in a bipolar ionic atmosphere*, Pure and Applied Geophysics 56 (1963) 185-193.

GASKOW, B.R., KITTELSON, D.B., ABDUL-KHALEK, I.S., AHAMADI, M.R., MORRIS, J.E., *Characterization of Exhaust Particulate Emissions from a Spark Ignition Engine,* SAE paper number 980528 (1998).

GIECHASKIEL, B., NTZIACHRISTOS, L., SAMARAS, Z., SCHEER, V., CASATI, R., VOGT, R., *Formation potential of vehicle exhaust nucleation mode particles on-road and in the laboratory,* Atmospheric Environment 39 (2005) 3191-3198.

GONZALES BAQUET, T., GROTHEER, H-H., AIGNER, M., *Simultaneous detection of two types of soot precursor particles using photo ionization mass spectrometry,* Rapid communications in mass spectrometry 21 (2007) 4060-4064.

GORMELEY, P.G., KENNEDY, M., *Diffusion from a Stream Flowing Through a Cylindrical Tube,* Proceedings of the Royal Irish Academy 52A (1949) 163-169.

GOTHANIYA, G., LEE, S-Y., MENON, A., IYER, S., LINEVSKY, M.J., LITZINGER, T.A., SANTORO, R.J., *A study on the effect of experimental setup configuration on soot formation in laminar premixed ethylene-air flame*, in Combustion Generated Fine Car-

bonaceous Particles, Ed by Bockhorn, H., D'Anna, A., Sarofim, A.F., Wang, H., (2007) 645-646.

HAMAKER, H.C., *The London-Van der Walls attraction between spherical particles,* Physica IV 10 (1937) 1058-1072.

HARRIS, S.J., MARICQ, M.M., *Signature size distributions for diesel and gasoline engine exhaust particulate,* Journal of Aerosol Science 32 (2001) 749-764.

HARTLIEB, A.T., ATAKAN, B., KOHSE-HOINGHAUS, K., *Effects of a sampling quartz nozzle on the flame structure of a fuel-rich low pressure propene flame,* Combustion and Flame 121 (2000) 610-624.

HEPP, H., SIEGMANN, K., SATTLER, K., *New aspects of growth mechanisms for polycyclic aromatic hydrocarbons in diffusion flames,* Chemical Physics Letters 233 (1995) 16-22.

HINDS, W.C., *Aerosol Technology. Properties, behavior, and measurement of airborne particles*, 2nd ed 1999, John Wiley & Sons, New York, NY

HOLMES, N.S., *A review of particle formation events and growth in the atmosphere in the various environments and discussion of mechanistic implications,* Atmospheric Environment 41 (2007) 2183-2201.

HOLTHUIS & ASSOCIATES – P.O. BOX 1531, SEBASTOPOL, CALIFORNIA 95473, U.S.A., HTTP:// *www.flatflame.com*

HOMANN, K.H., WAGNER, H.GG., *Some new aspects of the mechanism of carbon formation in premixed flames*, Proceedings of the Combustion Institute 11 (1967) 371-379.

HOWARD, J.B., WERSBORG, B.L., WILLIAMS, G.C., *Coagulation of carbon particles in premixed flames*, Faraday Symposia of the Chemical Society 7 (1973) 109-119.

INOUE, M., MURASE, A., YAMAMOTO, M., KUBO, S., *Analysis of volatile nanoparticles emitted from diesel engine using TOF-SIMS and metal-assisted SIMS (MetA-SIMS)*, Applied Surface Science 252 (2006) 7014-7017.

INTERNATIONAL ENERGY AGENCY (IEA) - *Key World Energy Statistics* 2006.

JENNINGS, B.R., PARSLOW, K., *Particle Size Measurement: The Equivalent Spherical Diameter,* Proceedings of the Royal Society of London, Series A 419 (1988) 137-149.

JOHN, W., *Size distribution Characteristics of Aerosols,* in Aerosol Measurement: Principles, Techniques, and Applications, 2nd Ed. by Baron, P.A., Willeke, K., (2001) 99-116, John Wiley & Sons, New York, NY.

JUNG, C.H., KIM, Y.P, *Numerical estimation of the effects of condensation and coagulateon on visibility using the moment method*, Journal of Aerosol Science 37 (2006) 143-161.

KANDPAL, J.B., MAHESHWARI, R.C., KANDPAL, T.C., *Indoor air pollution from domestic cookstoves using coal, kerosene and LPG*, Energy Conversion and Management 36 (1995) 1067-1072.

KASPER, M., SIEGMANN, K., SATTLER, K., *Evaluation of an in situ sampling probe for its accuracy in determining particle size distributions from flames,* Journal of Aerosol Science 28 (1997) 1569-1578.

KESTEN, J., REINEKING, A., PORSTENDORFER, J., *Calibration of a TSI Model 3025 Ultrafine Condensation Particle Counter,* Aerosol Science and Technology 15 (1991) 107-111.

KITTELSON, D.B., WATTS, W.F., JOHNSON, J.P., *On-road and laboratory evaluation of combustion aerosols-Part1: Summary of diesel engine results,* Journal of Aerosol Science 37 (2006) 913-930.

KITTELSON, D.B., *Engines and nanoparticles: a review,* Journal of Aerosol Science 29 (1998) 575-588.

KLEEMAN, M.J., SCHAUER, J.J., CASS, G.R., *Size and composition distribution of fine particulate matter emitted from motor vehicles,* Environmental Science and Technology 34 (2000) 1132-1142.

KOTZIAS, D., *Indoor air and human exposure assessment – needs and approaches,* Experimental and Toxicologic Pathology 57 (2005) 5-7.

KREYLING, W.G., SEMMLER, M., MOLLER, W., *Dosimetry and Toxicology of Ultrafine Particles,* Journal of Aerosol Medicine 17 (2004) 140-152.

KUBO, S., CHATANI, S., KONDO, T., YAMAMOTO, M., INOUE, M., *Detailed properties of diesel volatile nanoparticles,* Transactions of the Japan Society of Mechanical Engineers B 72 (2006) 2619-2625.

KULMALA, M., VEHKAMAKI, H., PETAJA, T., DAL MASO, M., LAURI, A., KERMINEN, V.M., *Formation and grow rates of ultrafine atmospheric particles: a review of observations,* Journal of Aerosol Science 35 (2004) 143-176.

KYOTO PROTOCOL TO THE UNITED NATIONS FRAMEWORK CONVENTION ON CLIMATE CHANGE (1997).

LADOMMATOS, N., ABDELHALIM, S.M., ZHAO, H., HU, Z., *The effects of carbon dioxide in exhaust gas recirculation on diesel engine emissions*, Proceedings of the IMECH E Part D Journal of Automobile Engineering 212 (1998) 25-42.

LANZUOLO, G., SGRO, L.A., DE FILIPPO, A., BARONE, A.C., BORGHESE, A., D'ALESSIO, A., *Coagulation of Nanoparticles of Organic Carbon (NOC) in Exhaust Conditions*, Environmental Engineering Science (2008) in press.

LANZUOLO, G., DE FILIPPO, A., SGRO, L.A., D'ALESSIO, A., *Modeling of the Evolution of Nanoparticles Size Distributions Detected in Rich Premixed Flames by Differential Mobility Analysis,* 29th Meeting on Combustion Italian Section of the Combustion Institute (2006) Pisa, Italy.

LI, W. W., PASCHOLD, H., MORALES, H., CHIANELLI, J., *Correlations between short-term indoor and outdoor PM concentrations at residences with evaporative coolers*, Atmospheric Environment 37 (2003) 2691-2703.

LI, Z., WANG, H., *Drag force, diffusion coefficient, and electric mobility of small particles. I. Theory applicable to the free-molecule regime,* Physical Review E 68 (2003) 061206, 1-9.

MARICQ, M.M., *Thermal equilibration of soot charge distribution by coagulation*, Journal of Aerosol Science 39 (2008) 141-149.

MARICQ, M.M., *Electrical mobility based characterization of bimodal soot size distributions in rich premixed flames,* in Combustion Generated Fine Carbonaceous Particles, Ed. by Bockhorn, H., D'Anna, A., Sarofim, A.F., Wang, H., (2007) 347-366.

MARICQ, M.M., *On the electrical charge of motor vehicle exhaust particles*, Journal of Aerosol Science 37 (2006) 858-874.

MARICQ, M.M., *The dynamics of electrically charged soot particles in a premixed ethylene flame,* Combustion and Flame 141 (2005) 406-416.

MARICQ, M.M., *Size and charge of soot particles in rich premixed ethylene flames*, Combustion and Flame. 137 (2004) 340-350.

MARICQ, M.M., HARRIS, S.J., SZENTE, J.J., *Soot size distributions in rich premixed ethylene flames,* Combustion and Flame 132 (2003) 328-342.

MARICQ, M.M., CHASE, R.E., XU, N., LAING, P.M., *The effects of the catalytic converter and fuel sulfur level on motor vehicle particulate matter emissions: Light duty diesel vehicles,* Environmental Science Technology 39 (2002) 3191-3198.

MARINOV, N.M., PITZ, W.J., WESTBROOK, C.K., CASTALDI, M.J., SENKAN, S.M., *Modeling of aromatic and polycyclic aromatic hydrocarbon formation in methane and ethane flames,* Combustion Science Technology (1996) 116-117, 211-226.

MAVLIEV, R., WANG, H.C., *Design and Performance Characteristics of a Turbulent Mixing Condensation Nuclei Counter,* Journal of Aerosol Science 31 (2000) 933-944.

MCENALLY, C.S., PFEFFERLE, L.D., ATAKAN, B., KOHSE-HOINGHAUS, K., *Studies of aromatic hydrocarbon formation mechanisms in flames: Progress towards closing the fuel gap*, Progress in Energy and Combustion Science 32 (2006) 247-294.

MCMURRY, P.H., *The History of Condensation Nucleus Counters,* Aerosol Science and Technology 33 (2000a) 297-322.

MCMURRY, P.H., *A review of atmospheric aerosol measurements,* Atmospheric Environment 34 (2000b) 1959-1599.

MIGLIORINI, F., DE IULIIS, S., CIGNOLI, F., ZIZAK, G., *How "flat" is the rich premixed flame produced by your McKenna burner?* Combustion and Flame 153 (2008) 384-393.

MILLER, A., AHLSTRAND G., KITTELSON, D., ZACHARIAH, M., *The fate of metal (Fe) during diesel combustion: Morphology, chemistry, and formation pathways of nanoparticles,* Combustion and Flame 149 (2007) 129-143.

MILLER, J.H., *The kinetics of polynuclear aromatic hydrocarbon agglomeration in flames,* Proceedings of the Combustion Institute 23 (1990) 91-98.

MINUTOLO, P., D'ANNA, A., D'ALESSIO, A., *On detection of nanoparticles below the sooting threshold,* Combustion and Flame 152 (2008) 287-292.

MINUTOLO, P., D'ANNA, A., COMMODO, M., PAGLIARA, R., TONIATO, G., ACCORDINO, C., *Emissions of fine particles from natural gas domestic burners,* Fifth Mediterranean Combustion Symposium (2007) Monastir (Tunisia).

MINUTOLO, P., BRUNO, A., GALLA, D., D'ANNA, A., D'ALESSIO, A., *Characterization of nanoparticles formed in gas fuelled burners,* Chemical Engineering Transactions 10 (2006) 281-286.

MINUTOLO, P., GAMBI, G., D'ALESSIO, A., CARLUCCI, S., *Spectroscopic characterization of carbonaceous nanoparticles in premixed flames*, Atmospheric Environment 33 (1999) 2725-2732.

MINUTOLO, P., GAMBI, G., D'ALESSIO, A., D'ANNA, A., *Optical and spectroscopic characterization of rich premixed flames across the soot formation threshold,* Combustion Science Technology 101 (1994) 311-325.

MORAWSKA, L., THOMAS, S., BOFINGER, N., WAINWRIGHT, D., NEALE, D., *Comprehensive characterization of aerosols in a subtropical urban atmosphere: particle size distribution and correlation with gaseous pollutants,* Atmospheric Environment 32 (1998) 2467-2478.

NARSIMHAN, G., RUCKENSTEIN, E., *The Brownian coagulation of aerosols over the entire range of Knudsen numbers: Connection between the sticking probability and the interaction forces,* Journal of Colloid and Interface Science 104 (1985) 344-369.

NEMMAR, A., HOYLAERTS, M.F., HOET, P.H., NEMERY, B., *Possible mechanisms of the cardiovascular effects of inhaled particles: systemic translocation and prothrombotic effects,* Toxicological Letters 149 (2004) 243-253.

NEMMAR, A., HOET, P.H.M., THOMEER, M., NEMERY, B., VANQUICKENBORNE, B., VANBILLONEN, H., *Passage of inhaled particles into the blood circulation in humans,* Circulation 105 (2002) 411-414.

OBERDORSTER, G., SHARP, Z., ATUDOREI, V., ELDER, A., GELEIN, R., LUNTS, A., *Extrapulmonary translocation of ultrafine carbon particles following whole-body inhalation exposure of rats,* Journal of Toxicology and Environmental Health A65 (2002) 1531-1543.

OBERDORSTER, G., *Pulmonary effects of inhaled ultrafine particles, le of the alveolar macrophage in lung injury: study with ultrafine particles,* International Archives of Occupational and Environmental Health 74 (2001) 1-8.

OBERDORSTER, G., FERIN, J., GELEIN, R., SODERHOLM, S.G., FINKELSTEIN, J., *Role of the alveolar macrophage in lung injury: study with ultrafine particles,* Environment and Health Perspectives 97 (1992) 193-199.

PARTS, T.E., *On the nature of small indoor air ions,* Journal of Aerosol Science 27 (1996) s445-s446.

PETZOLD, A., GYSEL, M., VANCASSEL, X., HILTZENBERGER, R., PUXBAUM, H., VROCHTICKY, S., WEINGARTNER, E., BALTENSPERGER, U., MIRABEL, P., *On the effects of organic matter and sulphur-containing compounds on the CCN activation of combustion particles,* Atmospheric Chemistry and Physics 5 (2005) 3187-3203.

PFEFFERLE, L.D., BERMUDEZ, G., BOYLE, J., *Benzene and Higher Hydrocarbon Formation During Allene Pyrolysis,* in Soot Formation in Combustion: Mechanisms and Models, Ed by Bockhorn, H., (1994) 25-49, Springer-Verlag, Heidelberg

POPE, C.A., *Epidemiology of fine particulate air pollution and human health: Biologic mechanisms and who's at risk?,* Environmental Health Perspectives 108 (2000) 713-723.

PREINING, O., *The physical nature of very, very small particles and its impact on their behaviour,* Journal of Aerosol Science 29 (1998) 481-495.

PRUCKER, S., MEIER, W., STRICKER, W., *A Flat flame burner as calibration source for combustion research: Temperatures and species concentrations of premixed H_2/Air flames,* Review of Scientific Instruments 65 (1994) 2908-2911.

REISCHL, G.P., MAKELA, J.M., NECID, J., *Performance of Vienna type differential mobility analyzer at 1.2-20 nanometer*, Aerosol Science and Technology 27 (1997) 651-672.

REISCHL, G.P., MAKELA, J.M., KARCH, R., NECID, J., *Bipolar charging of ultrafine particles in the size range below 10 nm*, Journal of Aerosol Science 27 (1996) 931-949.

REISCHL, J., *Measurement of Ambient Aerosols by the Differential Mobility Analyzer Method: Concepts and Realisation Criteria for the Size Range Between 2 and 500nm*, Aerosol Science and Technology 14 (1991) 5-24.

ROBINSON, A.L., DONAHUE, N.M., SHRIVASTAVA, M.K., WEITKAMP, E.A., SAGE, A.M., GRIESHOP, A.P., LANE, T.E., PIERCE, J.R., PANDIS, S.N., *Rethinking organic aerosols: semivolatile emissions and photochemical aging,* Science 315 (2007) 1259-1262.

RODRÌGUEZ, S., VAN DINGEGNEN, R., PUTUAD, J-P., MARTINS-DOS SANTOS, S., ROSELLI,D., *Nucleation and growth of new particles in the rural atmosphere of Northern Italy-relationship to air quality monitoring,* Atmosphere Environment 39 (2005) 6734-6746.

RONKKO, T., VIRTANEN, A., KANNOSTO, J., KESKINEN, J., LAPPI, M., PIRJOLA, L., *Nucleation mode particles with a nonvolatile core in the exhaust of a heavy duty diesel vehicle,* Environmental Science Technology 41 (2007) 6384-6389.

SEINFELD, J.H., *Atmospheric chemistry and physics of air pollution,* ed. 1996, John Wiley & Sons, New York, NY.

SGRO, L.A., BORGHESE, A., SPERANZA, L., BARONE, A.C., MINUTOLO, P., BRUNO, A., D'ANNA, A., D'ALESSIO, A., *Measurements of Nanoparticles of Organic Carbon and Soot in Flames and Vehicle Exhausts*, Environmental Science Technology 42 (2008a) 859-863.

SGRO, L.A., BARONE, A.C., COMMODO, M., D'ALESSIO, A., DE FILIPPO, A., LANZUOLO, G., MINUTOLO, P., *Measurement of Nanoparticles of Organic Carbon in Non-Sooting Flame Conditions*, in press on the Proceedings of the Combustion Institute 32 (2008b), available online at www.sciencedirect.com.

SGRO, L.A., DE FILIPPO, A., LANZUOLO, G., D'ALESSIO, A., *Characterization of nanoparticles of organic carbon (NOC) produced in rich premixed flames by differential mobility analysis*, Proceedings of the Combustion Institute 31 (2007a) 631-638.

SGRO, L.A., DE FILIPPO, A., *Size distribution measurements of nanoparticles of organic carbon in hydrocarbon-air flame,* 30th Meeting on Combustion Italian Section of the Combustion Institute (2007b) Ischia, Italy.

SGRO, L.A., BASILE, G., BARONE, A.C., D'ANNA, A., MINUTOLO, P., BORGHESE, A., D'ALESSIO, A., *Detection of combustion formed nanoparticles,* Chemosphere 51 (2003) 1079-1090.

SHADDIX, *Correcting Thermocouple Measurements for Radiation Loss: A Critical Review,* Proceedings of the 33rd National Heat Transfer Conference (1999) HTD99-282, Albuquerque, NM.

SHI, J.P., HARRISION, R.M., *Investigation of ultrafine particle formation during diesel exhaust dilution,* Environmental Science Technology 33 (1999) 3730-3736.

SHI, J.P., EVANS, D.E., KHAN, A.A., HARRISION, R.M., *Sources and concentration of nanoparticles (<10nm in diameter) in the urban atmosphere,* Atmospheric Environment 35 (2001) 1193-1202.

SINGH, J., PATTERSON, R.I.A., KRAFT, M., WANG, H., *Numerical simulation and sensitivity analysisa. of detailed soot particle size distribution in laminar premixed ethylene flames*, Combustion and Flame 145 (2006) 117-127.

SIOUTAS, C., DELFINO, R.J., SINGH, M., *Exposure Assessment for Atmospheric Ultrafine Particles (UFPs) and Implications in Epidemiologic Research*, Environmental Health Perspectives 113 (2005) 947-955.

STAINER, C.O., KHLYSTOV, A.Y., PANDIS, S.N., *Nucleation events during the Pittsburgh Air Quality Study: description and relation to key meteorological, gas phase, and aerosol parameters*, Aerosol Science Technology 38 (2004) 253-264.

STOLZENBURG, M.R., MCMURRY, P.H., *An Ultrafine Aerosol Condensation Nucleus Counters,* Aerosol Science and Technology 14 (1991) 48-65.

STOLZENBURG, M.R., *An Ultrafine Aerosol Size Distribution Measuring System,* Ph.D. Thesis, Mechanical Engineering Department, University of Minnesota, MN (1988).

TAMMET, H., *Size and mobility of nanometer particles, clusters and ions,* Journal of Aerosol Science 26 (1995) 459-475.

TAPCON & ANALYSESYSTEME GMBH, ALOIS STRASSE 9, A-5026 SALZBURG, AUSTRIA, HTTP:// www.emsvie.at

THIERLEY, M., GROTHEER, H-H., AIGNER, M., YANG, Z., ABID, A., ZHAO, B., WANG, *On existence of nanoparticles below the sooting threshold,* Proceedings of the Combustion Institute 31 (2007) 639-647.

TOBIAS, H.J., BEVING, D.E., ZIEMANN, P.J., SAKURAI, H., MCMURRY, P.H., ZARLING, D., WAYTULONIS, R., KITTELSON, D.B., *Chemical analysis of diesel engine nanoparticles using a nano-DMA / thermal desorption particle beam mass spectrometer,* Environmental Science Technology 35 (2001) 2233-2243.

TRIER, A., *Submicron particles in an urban atmosphere: a study of optical size distributions-I,* Atmospheric Environment 31 (1997) 909-914.

TSI INCORPORATED – 500 CARDIGAN ROAD, SHOREVIEW, MN 55126 USA, HTTP: // www.tsi.com

US EPA, *Air Quality Criteria Document for Particulate Matter (October 2004) Volume I & II*, HTTP: // WWW.EPA.GOV/OAR/PARTICLEPOLLUTION/PUBLICATIONS.HTLM

US EPA, *The Particle Pollution Report Current Understanding of Air Quality and Emissions through 2003*, HTTP: // WWW.EPA.GOV/AIRTRENDS/AQTRND04/PMREPORT03/REPORT_2405.PDF

VAARASLATHI, K., RISTIMAKI, J., VIRTANEN, A., KESKINEN, J., GIECHASKIEL, B., SOLLA, A., *Effect of oxidation catalysts on diesel soot particles,* Environmental Science Technology 40 (2006) 4776-4781.

VAARASLATHI, K., VIRTANEN, A., RISTIMAKI, J., KESKINEN, J., *Nucleation mode formation in heavy-duty diesel exhaust with and without a particulate filter,* Environmental Science Technology 38 (2004) 4884-4890.

VANDER WAL, R.L., *Soot precursor carbonization: Visualization using LIF and LII and comparison using bright and dark field TEM,* Combustion and Flame 112 (1998) 607-616.

VIOLI, A., D'ANNA, A., D'ALESSIO, A., *Modeling of particulate formation in combustion and pyrolysis,* Chemical Engineering Science 54 (1999) 3433-3442.

WANG, H.C., KASPER, G., *Filtration Efficiency of Nanometer-Size Aerosol Particles,* Journal of Aerosol Science 22 (1991) 31-41.

WANG, X., BI, X., CHEN, D., SHENG, G., FU, J., *Hospital indoor respirable particles and carbonaceous composition,* Building and Environment 41 (2006) 992-1000.

WEBER, R.J., MCMURRY., P.H., MAULDIN, L., TANNER, D.J., EISELE, F.L., BRECHTEL, F.J., KREIDENWEIS, S.M., KOK, G.L., SCHILLAWSKI, R.D., BAUMGARDNER, D., *A study of new particle formation and growth involving biogenic and trace gas species measured during ACE 1*, Journal of Geophysical Research-Atmospheres 103 (D13) (1998) 16385-16396.

WEGERT, R., WIESE., W., HOMANN, K-H., *Molecular beam/Wien filter application to the study of charged soot in flames: Methodology and mass distributions of particles in butadiene flames*, Combustion and Flame 95 (1993) 61-75.

WEILMUNSTER, P., KELLER, A., HOMANN, K-H., *Large Molecules, Radicals, Ions, and Small Soot Particles in Fuel-Rich Hydrocarbon Flames-Part I: Positive Ions of Polycyclic Aromatic Hydrocarbons (PAH) in Low-Pressure Premixed Flames of Acetylene and Oxygen*, Combustion and Flame 116 (1999) 62-83.

WERSBORG, B.L., HOWARD., J.B., WILLIAMS, G.C., *Physical mechanisms in carbon formation in flames*, Proceedings of the Combustion Institute 14 (1973) 929-940.

WICHMANN, H.E., SPIX, C., TUCH, T., WOLKE, G., PETERS, A., HEINRICH, J., KREYLING, G., HEYDER, J, *Daily mortality and fine and ultrafine particles in Erfurt, Germany. Part-I: Role of particle number and particle mass.*, Health Effects Institute Research Report, number 98 (2000).

WIEDENSOHLER, A., ORSINI, D., COVERT, D.S., COFFMANN, D., CANTRELL, W., HAVLICEK, M., BRECHTEL, F.J., RUSELL, L.M., WEBER, R.J., GRAS J., HUDSON, J.G., LITCHY, M., *Intercomparison Study of the Size-Dependent Counting Efficiency of 26 Condensation Particle Counters*, Aerosol Science and Technology 27 (1997) 224-242.

WIEDENSOHLER, A., *An approximation of the bipolar charge distribution for particles in the submicron size,* Journal of Aerosol Science 19 (1988) 387-389.

WIEDENSOHLER, A., LUTKEMETER, E., FELDPAUSH, M., HELSPER, C., *Investigation of the Bipolar Charge Distribution at Various Gas Conditions,* Journal of Aerosol Science 17 (1986) 413-416.

WINKLMAYR, W., REISCHL, G.P., LINDNER, A.O., BERNER, A.*, A new electromobility spectrometer for the measurement of aerosol size distributions in the size range from 1 to 1000 nm*, Journal of Aerosol Science 22 (1991) 289-296.

WHITBY, K.T.*, The physical characterization of sulfur aerosols*, Atmospheric Environment 12 (1978) 135-159.

WOLKOFF, P., NIELSEN, G.D., *Organic compounds in indoor air-their relevance for perceived indoor air quality?,* Atmospheric Environment 35 (2001) 4407-4417.

WOO, K.S., CHEN, D.R., PUI, D.Y.H., MCMURRY, P.H., *Measurement of Atlanta Aerosol Size Distributions: Observations of Ultrafine Particle Events,* Aerosol Science and Technology 34 (2001) 75-87.

YU, F., TURCO, R.P., *Ultrafine aerosol formation via ion-mediated nucleation,* Geophysical Research Letters 27 (2000) 883-896.

ZHAO, B., YANG, Z., WANG, J., JOHNSTON, M.V., WANG, H., *Analysis of Soot Nanoparticles in a laminar premixed Ethylene Flame by Scanning Mobility Particle Sizer*, Aerosol Science and Technology 37 (2003) 611-620.

ZHENG, M., READER, G.T., HAWLEY, J.G., *Diesel engine exhaust gas recirculation-a review on advanced and novel concepts*, Energy Conversion and Management 45 (2004) 883-900.